Universität
Rostock
Traditio et Innovatio

Polymer nucleation and crystallization investigated by in situ combination of atomic force microscopy (AFM) and fast scanning calorimetry (FSC)

Dissertation

zur Erlangung des Grades

doctor rerum naturalium (Dr. rer. nat.)

am Institut für Physik

der Mathematisch-Naturwissenschaftlichen Fakultät

der Universität Rostock

vorgelegt von

M.Eng. Rui Zhang

aus Chengdu, Volksrepublik China

https://doi.org/10.18453/rosdok_id00002777

Gutachter:
Prof. Dr. Christoph Schick, Universität Rostock, Institut für Physik
Prof. Dr. René Androsch, Martin-Luther-Universität Halle-Wittenberg, Zentrum für Ingenieurwissenschaften

Jahr der Einreichung: 2020

Jahr der Verteidigung: 2020

Abstract

A chip based fast scanning calorimeter (FSC) is used as a fast hot-stage in an atomic force microscope (AFM). This way, the morphology of materials with a resolution from micro to nano meters after fast thermal treatments becomes accessible. FSC can treat the sample isothermally or at heating and cooling rates up to 1 MK s^{-1}. The short response time of the FSC in the order of milliseconds enables rapid changes from scanning to isothermal modes and vice versa. Additionally, FSC provides crystallization/melting curves of the sample just imaged by AFM. A combined AFM-FSC device is described, where the AFM sample holder is replaced by the FSC chip-sensor. The sample can be repeatedly annealed at pre-defined temperatures and times and the AFM images can be taken from exactly the same spot of the sample.

Homogeneous crystal nucleation in polyamide 66 (PA 66) was studied by the AFM-FSC described above. PA 66 was subjected to Tammann's two-stage crystal nuclei development method. With the number of crystals/nuclei detected by AFM imaging and by variation of the nucleation time, a value of the steady-state nucleation rate equal to $(2.3\pm0.2)\times10^{18}$ m^{-3} s^{-1} at 310 K has been determined. Comparing the total enthalpy of melting crystals, obtained by FSC, with the number of crystals, observed by AFM, yields the specific enthalpy of melting/formation of one single crystal of $(5.2\pm0.5)\times10^{-13}$ J at the specific growth conditions applied. Application of this approach, that is, correlating transition enthalpies with nuclei numbers, for analysis of crystal nucleation in a wide range of temperatures between 310 and 375 K yielded a maximum nucleation rate close to 10^{19} m^{-3} s^{-1} at 350 K. The present thesis offers a qualitatively new approach of analysing the kinetics of homogeneous nucleation of polymers. In addition, it allows employing the specific AFM-FSC setup as a valuable tool for direct observation of crystal-specific enthalpies of crystallization.

Zusammenfassung

Ein Chip-basiertes Schnellscan-Kalorimeter (FSC) wird als schnelle Heißstufe in einem Atomkraftmikroskop (AFM) verwendet. Auf diese Weise wird die Morphologie von Materialien mit einer Auflösung von Mikro- bis Nanometern nach schnellen thermischen Behandlungen zugänglich. FSC kann die Probe isotherme oder mit Heiz- und Kühlraten bis zu 1 MK s^{-1} behandeln. Die kurze Reaktionszeit des FSC in der Größenordnung von Millisekunden ermöglicht schnelle Änderungen vom Scannen in isotherme Modi und umgekehrt. Darüber hinaus bietet FSC Kristallisations-/Schmelzkurven der Probe, die nur von AFM abgebildet wurde. Ein kombiniertes AFM-FSC-Gerät wird beschrieben, bei dem der AFM-Probenhalter durch den FSC-Chipsensor ersetzt wird. Die Probe kann wiederholt bei vordefinierten Temperaturen und Zeiten geglüht werden und die AFM-Bilder können genau an der gleichen Stelle der Probe aufgenommen werden.

Die homogene Kristallkernung in Polyamid 66 (PA 66) wurde vom oben beschriebenen AFM-FSC studiert. PA 66 wurde Tammanns zweistufiger Kristallkernentwicklungsmethode unterzogen. Mit der Anzahl der durch AFM-Bildgebung und durch Variation der Keimzeit nachgewiesenen Kristalle/Kerne wurde ein Wert der stationären Keimbildungsrate von $(2{,}3\pm0{,}2)\times10^{18}$ m^{-3} s^{-1} bei 310 K ermittelt. Vergleicht man die gesamte Enthalpie der Schmelzkristalle, die von FSC erhalten werden, mit der Anzahl der von AFM beobachteten Kristalle ergibt sich die spezifische Enthalpie des Schmelzens/Der Bildung eines einzigen Kristalls von $(5{,}2\pm0{,}5)$ 10^{-13} J unter den angewandten spezifischen Wachstumsbedingungen. Die Anwendung dieses Ansatzes, d.h. die Korrelation von Übergangsenthalpies mit Kernzahlen, zur Analyse der Kristallkernbildung in einem weiten Temperaturbereich zwischen 310 und 375 K ergab eine maximale Keimrate nahe 10^{19} m^{-3} s^{-1} bei 350 K. Die vorliegende These bietet einen qualitativ neuen Ansatz zur Analyse der Kinetik der homogenen Kernbildung von Polymeren. Darüber hinaus ermöglicht es den Einsatz des spezifischen AFM-FSC-Setups als wertvolles Werkzeug zur direkten Beobachtung kristallisierter Enthalpies der Kristallisation.

Table of Contents

1 Introduction

Polymers can be found both in nature and in engineering applications. Due to the great variability of their chemical structure, this ranges from the reproduction of the genetic information in deoxyribonucleic acid (DNA) to simple applications of synthetic polymers such as plastic bags or car bumpers and many other more or less complex applications. In most cases, the functionality of polymers is based on self-organization. DNA, for example, forms a double helix and most of the engineering polymers have semicrystalline morphologies. Crystallization in polymers is a self-assembly process on the nanometer scale with tremendous consequences for the mechanical, optical, electrical and other properties. Polymer crystallization and the resulting semi-crystalline morphologies have therefore been the subject of extensive studies for many years [1]. In contrast to atoms or small molecules, polymers have long molecular chains, which do not allow the whole molecules to arrange into in a perfect three-dimensional crystal lattice, resulting in semi-crystalline materials. The formation of such semi-crystalline polymer morphologies usually follows the sequence of nucleation, growth and perfection [2-6]. Many experimental methods have been applied to study polymer crystallization, including calorimetry [7], microscopy [8], X-ray- [3, 4], electron-[9], neutron-diffraction [10], NMR [11] and so on. Different microscopes can be used to visualize the semicrystalline morphology on different length scales. Optical microscopy, particularly with polarized light (POM), is one of the techniques applied in crystallography for decades [12]. In combination, *ex-situ* or *in-situ*, with fast scanning calorimetry (FSC) it provides deep insights into crystal nucleation and growth even for fast-crystallizing materials [13-16]. Nevertheless, the size of the crystals or crystal superstructures like spherulites must be in the micrometer range to be visible. Electron microscopy, due to the much higher resolution, provides an alternative to optical microscopy [17, 18]. Nowadays, high-resolution transmission electron microscopy (HRTEM) allows imaging with atomic resolution. Often a focused ion beam (FIB) is employed for HRTEM sample preparation [19]. Structures generated by fast controlled cooling in FSC became accessible this way [20, 21]. The drawbacks of HRTEM, on the other side, are the enormous efforts required for sample preparation and possible sample damage by the electron beam [22], preventing its broad application to kinetic studies of organic materials. For time-resolved scanning electron microscopy (SEM) less demanding sample preparation is required [23]. A combination of FSC with SEM was reported by LaVan et al. for the *in situ* observation of phase transitions even in polymers [24]. Another microscopic technique with a molecular single-chain resolution for polymers is atomic force microscopy (AFM) [25, 26]. AFM is an imaging technique, usually not requiring sophisticated treatments of the sample surface. In combination with a hot stage, AFM can follow polymer crystallization on the lamellar scale *in-situ* [27-29]. The formation of spherulites [30, 31], recrystallization [32] and mesophase formation [33, 34] were also shown.

Differential scanning calorimetry (DSC) is one of the most widely used and convenient tools for studying crystallization kinetics. DSC with precise temperature control has been used to treat samples for AFM studies [35]. The use of DSC for sample preparation has several advantages. DSC provides more flexible and faster temperature control than a hot-stage, enabling complex multi-step time-temperature experiments. Calorimetric data recorded during and after the heat treatment contain information about the morphology of the sample. Information about the non-crystalline part may be available from the glass transition, and the enthalpy and temperature of melting provide knowledge about the crystal fraction and crystal perfection, respectively. From cold crystallization on heating information about the presence of crystal nuclei is accessible too [36]. However, the slow heating and cooling rates of DSC (< 10 K s^{-1}) limit its application, and particularly fast quenching and crystallization at deep undercooling of the melt is often not possible. Recent developments of fast scanning calorimetry (FSC) allow cooling the equilibrium melt of polymers at rates up to 1,000,000 K s^{-1} mainly achieved by a much decreased heat capacity of both the sample and the measuring system [37], which is opening interesting opportunities for a combination with AFM. Androsch et al. employed AFM *ex-situ* in combination with FSC for the investigation of polymer crystallization [33, 38-40]. After the thermal treatment of the sample, the sensor was taken out of the calorimeter and the membrane irreparably removed from the chip. The thin membrane with the sample was mounted on the AFM sample holder and the images were collected. As an intermittent step towards an *in-situ* combination of FSC and AFM Van den Brande et al. [41] applied FSC and AFM to the crystallization of materials for organic electronics. In this research, similar to Androsch et al. [33], the sample was first treated by FSC to allow crystallization under particular conditions. Afterwards, the whole sensor was transferred to the AFM for imaging. Contrary to the sensors used by Androsch et al. the AFM images could be taken without destroying the chip sensor. Consequently, the same sample could be again thermally treated and imaged to illustrate the formed crystals [38, 41]. Finding back the same spot of the sample for imaging was difficult and therefore the growth of individual objects could not be followed. By an *in-situ* combination of AFM with FSC this limitation could be overcome.

In this thesis, I will describe the realized *in-situ* combination of AFM with FSC. The aim of this combination is the collection of images from exactly the same spot of the sample either after different thermal treatments by FSC or directly during isothermal annealing of the sample. The chip calorimeter sensor is used as the sample holder for the AFM and it is connected to the FSC electronics allowing fast heating and cooling as well as isothermal treatments of the sample. In other words, I will describe a fast AFM hot stage with millisecond time resolution and the ability to perform calorimetric measurements in the AFM.

The combined AFM-FSC instrument is first employed to study polymer crystallization on different length scales. Images can be obtained from exactly the same spot of the sample, permitting e.g. following the progress of nucleation, crystallization, reorganization, or melting when freezing the structure by the fast-cooling option of the FSC. Finally, the homogeneous nucleation of crystals in polymers is investigated at a depth that has not been possible so far. To gain information about nuclei numbers, additional imaging of samples at the nanometer-length scale and counting of crystals is needed, which, however, is challenging since FSC still is required to subject the sample to the desired thermal profiles. A new approach of obtaining absolute numbers of homogeneous crystal nuclei from FSC data will be introduced, based on Tammann’s method and the combined AFM-FSC device. I estimated the enthalpy of formation of one single crystal, at the specific growth conditions applied, by correlating the number of crystals in the sample obtained by AFM with the calorimetrically observed enthalpy of crystallization/melting. With this knowledge, it is possible to convert any observed transition enthalpy associated with specific nucleation conditions into nuclei numbers/densities, with the boundary condition that growth conditions are unchanged.

The thesis is structured as follows: In the next chapter, a short review of the state of the art regarding the theoretical description of polymer nucleation and crystallization and relevant investigations by novel experimental approaches is given. Chapter 3 is associated with some detailed information about the combination of AFM and FSC. This way, the morphology of materials with a resolution from micrometers to nanometers after fast thermal treatments becomes accessible. In chapter 4, some examples of application of the new

AFM-FSC combination to polymer crystallization, including spherulite growth rates, crystals morphologies, memory effects in melt-recrystallization and tip-induced crystal nucleation are illustrated. Last but not the least, in chapter 5 the analysis and discussion towards my final task of a detailed study of homogenous nucleation of polymers is presented on the example of polyamide 66 (PA 66).

2 Literature review

2.1 Some critical problems in studying homogeneous nucleation in polymers.

The main difficulty in studying homogeneous nucleation of polymers is that the sample is hard to be quenched to deep supercooling without any crystallization during cooling. Heterogeneous nucleation usually happens at the surface of nucleation agents. The energy barrier for forming heterogeneous nuclei is significantly smaller than for homogeneous nucleation, which leads heterogeneous nucleation to be dominant at low supercooling. Therefore, polymer crystallization is commonly investigated at low supercooling of the melt, initiated by heterogeneous nuclei [42, 43].

In addition, the sizes of nuclei are tiny and cannot be observed by most microscopes. A method to overcome this is Tammann's two-stage nuclei development method, which includes nucleating the sample at one temperature and developing the nuclei to observable crystals at another higher temperature. By this method, the nucleation density can be estimated through the density of developed crystals, which gives a possibility of estimating nucleation kinetics. POM is a widely used microscopic technique for observing polymer crystals. The limitation in resolution only enables POM to observe well-developed μm-sized spherulites [16]. This drawback limits the application of POM for the estimation of high nucleation densities of semi-crystalline polymers.

In addition, the morphology and properties of semi-crystalline polymers are widely controlled by the density of crystal nuclei formed in their liquid or glassy states. For this reason, understanding crystal nucleation is essential for both gaining comprehensive insights into polymer crystallization as well as for optimization of polymer processing. Crystal nucleation may occur through two qualitatively different pathways. In the first one, denoted as homogeneous nucleation, the nuclei directly develop in the bulk of the polymer by spontaneous rearrangement of molecule segments to form small ordered clusters. In the second one, called heterogeneous nucleation, heterogeneities like foreign surfaces, impurities, substrates, but also remnants of former crystals may act as nuclei for the crystallization process. Homogeneous nucleation, as a rule, requires high supercooling of the liquid, due to the high-energy barrier needed to obtain a nucleus of supercritical size at moderate undercooling. This activation energy for nucleation is decreased with decreasing temperature. Typically, homogeneous nucleation is most effective at temperatures close to the glass transition. At higher temperatures, homogeneous nucleation is often outpaced by heterogeneous nucleation due to the significant reduction of the nucleation barrier by mentioned above heterogeneous nucleation cores. This dominance of heterogeneous nucleation is reduced with decreasing temperature since the number of heterogeneous nucleation cores is as a rule small as compared with the number of places where homogeneous nucleation may take place. At lower temperatures, in the glassy state, nucleation constraints arise both for homogeneous and heterogeneous nucleation by the limited mobility of structural motifs required to form a nucleus. Analysis of crystal nucleation from a kinetic point-of-view includes measurements of the temperature-dependence of the crystallization rate, which yielded for many polymers a bimodal dependence, revealing temperature ranges of dominant heterogeneous and homogeneous nucleation. As noted, the presence of heterogeneous nucleation cores leads to a decrease of the nucleation barrier, which has to be overcome in homogeneous nucleation. Consequently, the knowledge of the basic mechanism of homogeneous nucleation is also a prerequisite for understanding heterogeneous nucleation. For this reason, the understanding of the basic features of homogeneous nucleation is an essential ingredient also for the description of the more complex features of heterogeneous nucleation. Analysis of homogeneous crystal nucleation requires the absence of heterogeneous nucleation. This absence is achieved either by transferring the equilibrium liquid of interest into a state of high supercooling without prior crystallization at low supercooling initiated by heterogeneous nuclei, or by removing all heterogeneous nucleation sites in the sample. The latter is possible within droplet-experiments, that is, by subdividing the system into small compartments with a size smaller than the characteristic distance between heterogeneous nuclei. In that case, the transfer of the equilibrium melts to temperatures where homogeneous nucleation is effective is uncritical and analysis can even be realized by conventional DSC or hot stage microscopy, that is, at rather slow cooling. Since droplet-experiments may not fully suppress heterogeneous nucleation at substrates or the interface to the surrounding phase, analysis of homogeneous nucleation in bulk seems advantageous, however, requires sophisticated tools for bypassing the temperature-range where heterogeneous nuclei are active. Such tools include FSC which is employed in the present thesis. For most polymers, the high cooling rate by FSC permits suppressing heterogeneous nucleation and crystallization at high temperature, allowing studying homogeneous nucleation at high melt-supercooling and even in the crystal-free glassy state.

FSC, when employing Tammann’s approach, allows evaluation of the kinetics of homogeneous nucleation as a function of temperature, however, the determination of absolute nuclei numbers or densities is not possible without further assumptions.

Furthermore, tip-induced nucleation and crystallization is a serious problem for applying AFM to study polymer crystallization. The working mechanism of AFM requires the tip to have weak interactions with the sample surface in order to record the surface morphology. These weak interactions may introduce nucleation and crystallization at the sample surface. Two different mechanisms have been proposed to explain this phenomenon. First, the tip may introduce weak stresses at the sample surface, which causes tiny ordered structures at the molecular level. Moreover, these tiny ordered structures further develop into active centers of nucleation. Second, the cold-tip would cause a local cooling at the hot sample surface, which increases the supercooling at the position of the tip. Investigating tip-induced nucleation and crystallization of polymers is another interesting field.

2.2 Crystal nucleation, growth and perfection

The general opinion about polymer crystallization assumes that polymer crystallization follows the sequence of nucleation, growth and perfection [3], as schematically shown in Figure 1. In Figure 1(A), a coil-like pattern represents a nucleus. Figure 1(B) is a lamellar leaf with a small number of lamellae. As illustrated in Figure 1(B) – (D), the lamellar leaf becomes more branched and growth. Finally, Figure 1(E) illustrates the formed spherulite.

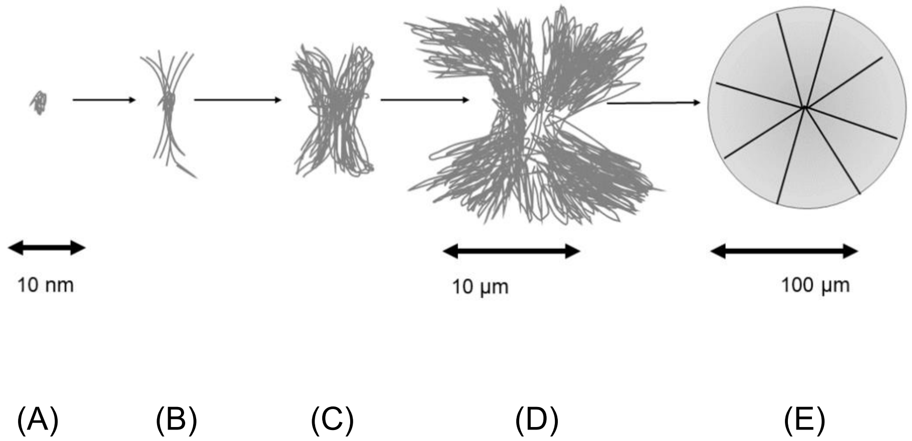

Figure 1 Schematic of polymer crystallization from a stable nucleus to a spherulite. The patterns with the order from left to right are the nucleus (A), lamellar leaf (B), branched lamellar leaf (C-D) and spherulite (E), respectively.

Primary nucleation has been thought of as the first step of crystallization, influencing the morphology and physical properties of semi-crystalline polymers by controlling the density of crystals [1]. The understanding of nucleation is therefore important for tailoring the properties of semi-crystalline polymers. Several theories on crystal nucleation exist. A very general one is the classical nucleation theory (CNT) proposed by Gibbs [44, 45]. This theory initially describes the thermodynamics of inhomogeneous systems, which is composed of two homogeneous phases with zero-thickness at the edge [46]. When this theory is applied to crystallization, the two homogeneous phases correspond to the amorphous and the crystalline phases, respectively.

Homogeneous nucleation generally begins with a non-steady state and gradually develops to a steady state. As described by CNT, the time required for developing the steady state nucleation is the time-lag τ. Only nuclei exceeding the critical size, can further grow to crystals. According to CNT, τ can be estimated through [46-48]:

$$\tau = \frac{16h}{\pi} \frac{\sigma_{cm}}{\Delta G_V^2 \alpha^4} exp\left(\frac{\Delta G_D}{k_B T}\right) \tag{1}$$

Because the nucleation rate at non-steady state conditions are unpredicted, only nucleation rates at steady state, *I*(*t*), have a well-defined time-dependence, which can be quantitatively measured and estimated. According CNT, *I*(*t*) can be expressed as follows:

$$I(t) = I_{st}\left[1 + 2\sum_{m=1}^{\infty} (-1)^m \, exp\left(-m^2 \frac{t}{\tau}\right)\right] \tag{2}$$

The number volume density of nuclei, $N_V(t)$, can be obtained through integrating Eq.(2), as

$$\frac{N_V(t)}{I_{st}\tau} = \left[\frac{t}{\tau} - \frac{\pi^2}{6} - 2\sum_{m=1}^{\infty} \frac{(-1)^m}{m^2} exp\left(-m^2 \frac{t}{\tau}\right)\right] \tag{3}$$

Eq.(3) can be simplified if t >> τ, as

$$N_V(t) = I_{st}\left(t - \frac{\pi^2}{6}\tau\right) \tag{4}$$

For calorimetric studies, τ is hard to be directly determined through experimental curves; an empirical method for predicting τ is proposed as [46]

$$\tau = \frac{6}{\pi^2} t_{onset} \tag{5}$$

where t_{onset} can be assessed through linear fitting, being the onset time in the experimental curve of the nuclei density versus the annealing time. The nucleation rate also shows a dependence on temperature, as described by Eq.(6).

$$I_{\text{st}} = \text{c}\sqrt{\frac{\Delta\sigma}{K_B T}}\left(\frac{D}{d_0}\right) exp\left(-\frac{W_c}{K_B T}\right) \tag{6}$$

However, CNT is based on the assumption that there is zero-thickness in the phase edge between crystalline and amorphous phases. The CNT described above is suitable for describing both, homogeneous and heterogeneous nucleation.

Figure 2 shows schematically the growth of crystals at low supercooling [49]. In the beginning, small spherulites gradually become bigger and with increasing annealing time more crystals can be observed due to ongoing nucleation. After a certain time, crystals will touch each other (impingement) and the crystallization rate will slow down. Finally, a space filling morphology is formed.

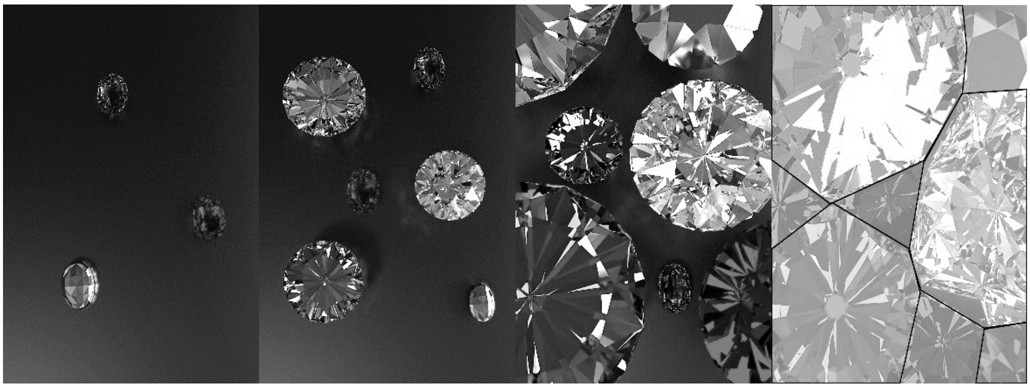

Figure 2 Schematic of the growth of polymer spherulites. The plots from left to right are the morphology with increasing annealing time.

However, recent experiments demonstrated that polymers formed a non-spherulitic morphology at deep supercooling [50]. Figure 3 is the morphology of isotactic polypropylene (iPP) after rapidly cooling down from the melt. The left, middle and right images were mapped by different advanced microscopic techniques. The morphology of the iPP is particle-like rather than spherulitic. The density of these particle-like crystals is high. Also, as shown in the images, the growth of these crystals seems to be independent on each other [51]. The particle-like shaped crystals are commonly named as nodules [52].

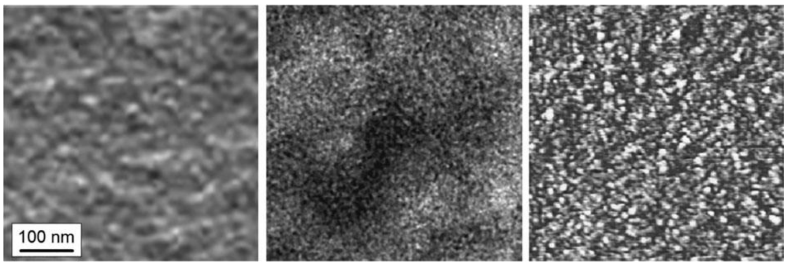

Figure 3 Transmission electron microscopy images (left [53] and center [54]) and an atomic force microscopy image (right [55]) of rapidly cooled films of isotactic polypropylene. The scale bar holds for all three images. (The images from left to right are reproduced with permission from John Wiley and Sons, Elsevier and Springer Nature, respectively)

2.3 Tip-induced nucleation and crystallization

Tip-induced nucleation has been frequently reported in AFM studies of polymer crystallization [27, 28, 30, 56]. Hobbs et al.[27, 28] observed a triangle pattern, always located at one end of the lamellae in AFM images. The triangle pattern was caused by the tapping of the AFM tip. Therefore, they proposed that lamellae begin to grow at the place where the AFM tip first contacted the surface. So, the primary nuclei may be formed by the AFM tip.

At the sample surface, polymers are able to form three-dimensional quasi-single crystals at temperatures near the melting temperature, that is at very low supercooling [57]. The single crystals pile up and form stack-like crystals. The growth of these stack-like crystals follows a screw shape, which refers to the dislocations growth introduced by Frank [58]. The lamellae tends to be “flat-on” rather than “edge-on” in this situation [59]. This phenomenon offers a possibility to study the nucleation mechanism from AFM tip tapping through the morphology of crystals at the surface. For heterogeneous nucleation, the crystals should grow as double-spiral structures, see Figure 4 (A) [5, 60, 61], as the growth only develops in particular directions [5]. For homogeneous nucleation, the crystals can develop to pillar structures with multiple layers, because the possibility of growth should be the same in all directions [57], see Figure 4 (B).

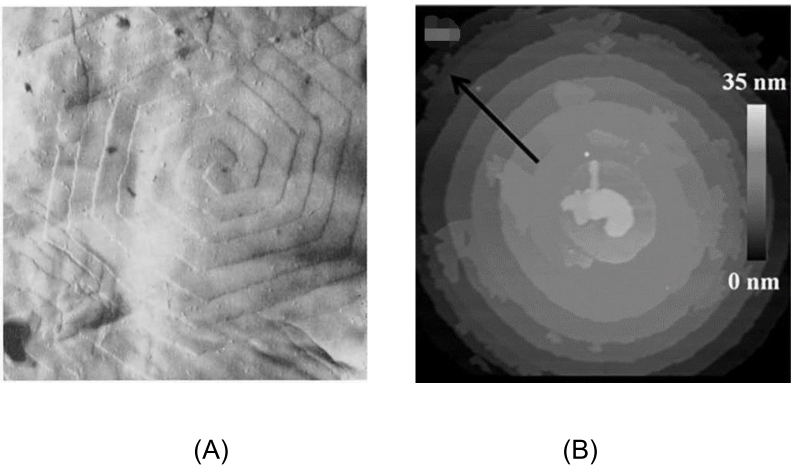

(A) (B)

Figure 4 A: Chain-folded crystal in iPP crystallized from the melt. Double spiral growth is of the same type as commonly found in solution-crystallized polymers. Lamellae are about 15nm thick. Polymer chain axes are perpendicular to the plane of the paper [5]. (Reproduced with permission from American Institute of Physics) B: AFM topographic image showing a stack of lamellar crystals for the section indicated by the red box in the panel. [57] (Reproduced with permission from American Chemical Society)

For the AFM-FSC device tip-induced nucleation will be discussed in chapter 4.1.2.

2.4 Calorimetry for studying crystallization and nucleation of polymers

Calorimetry has been applied to study polymer crystallization by tracing exothermic and endothermic effects during crystallization and melting, respectively [7]. The early work about studying homogeneous nucleation through differential scanning calorimetry (DSC) can be traced by Angell and Oguni with water [62]. At a later moment, Angell applied Tammann's two-stage crystallization method to DSC measurements in aqueous LiCl solutions [63] and $Ca(NO_3)_2$-KNO_3 [64]. This work shows that DSC is a powerful tool to trace homogenous nucleation if the crystallization rate is low.

Even polymers, due to the chain structure, are always forming semi-crystalline morphologies, are often crystallizing quite fast. Therefore, traditional DSCs are still too slow and cannot quench most of the polymers into a fully amorphous state. Hence, DSC can often not be applied to characterize homogenous nucleation kinetics of polymers. Only for slow crystallizing polymers like poly(L-lactide acid) (PLLA) DSC allows for systematic studies [36].

The fast heating and cooling ability of FSC offers a possibility to study homogeneous nucleation kinetics of polymers by calorimetry. In FSC, heater and thermopile are integrated into a few tens' micrometer square area on a chip-sensor. The sample mass for FSC is only a few nanograms. Therefore, the heat capacity from background and sample can be largely reduced. FSC can go up to scanning rates of 1,000,000 K s^{-1} for polymer samples [65].

FSC can easily quench most polymers to any isothermal temperature at such fast cooling rates that crystallization is prevented. Then the isothermal crystallization kinetics at crystallization temperatures between glass transition temperature (T_g) and equilibrium melting temperature ($T_{m,0}$) can be measured [50, 66-68]. Figure 5 is an example that the isothermal crystallization kinetics of poly (ε-caprolactone) (PCL) can be obtained at a wide crystallization temperature range from 15 K below T_g to near $T_{m,0}$ [69].

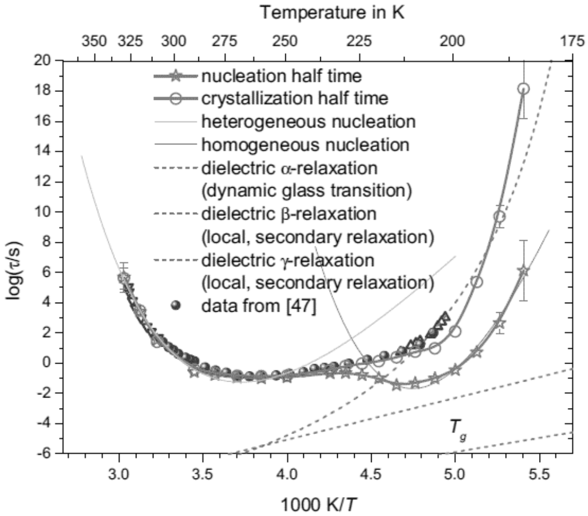

Figure 5 Nucleation and crystallization kinetics of PCL at different annealing temperatures between 180 K and 325 K. [70] (Reproduced with permission from Elsevier).

The characterization of nucleation kinetics by FSC can be carried through two ways; (i) analyzing the enthalpy of cold-crystallization peaks in reheating curves [66, 70, 71]; (ii) using Tammann's two-stage crystallization method [72, 73]. These two methods are illustrated in Figure 6 (A) and (B), respectively. In Figure 6 (A), PCL has been directly quenched to the nucleation temperature from the melt; and the sample has been heated up to the melt after isothermal annealing [70]. In this way, the nuclei formed during isothermal annealing can growth to crystals at reheating, so the enthalpy of the cold-crystallization peak represents the number of nuclei formed during isothermal annealing. In Figure 6 (B), PLLA was nucleated at 333 K and a growth stage at 393 K was added following Tammann's two stage method [74]. If the growth stage kept the same, the changes in final melting enthalpy correspond to the number of nuclei at the end of the nucleation stage.

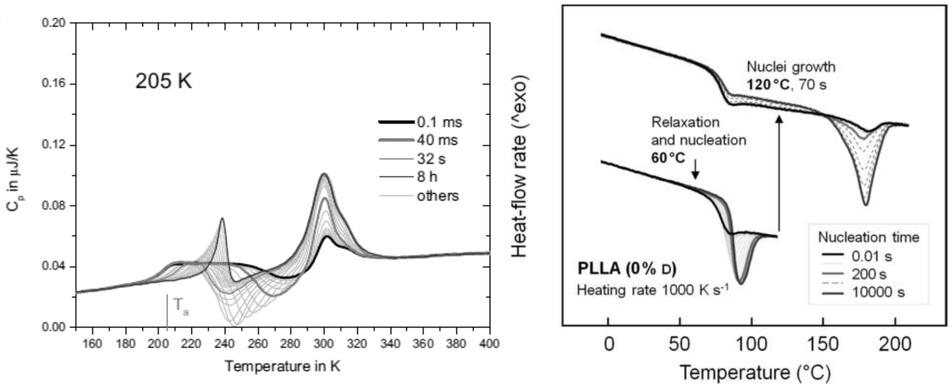

(A) (B)

Figure 6 (A): PCL annealed at 205 K for various times from 0.1 ms to 8 hours. [70] (B): Application of Tammann's two-stage method to PLLA [74]. (Reproduced with permission from Elsevier and American Chemical Society, respectively)

2.5 Mapping polymer nucleation and crystallization.

In-situ AFM can illustrate polymer crystallization in a visual way. Chan's group [31, 75, 76] used a slow AFM to trace polymer crystallization from the nucleation stage up to final spherulites. To obtain *in-situ* data, Chan et al. used a specially synthesized polymer poly (bisphenol A-co-octane) (BA-C8) as the sample. The crystallization rate of this polymer at ambient temperature is so slow that even a slow AFM still can map its crystallization. Meanwhile, Hobbs et al. took another way to *in-situ* study polymer crystallization by AFM [27, 77-79]. They used an AFM with a fast scanner and each AFM image can be recorded in a few seconds; hence, polymer crystallization can be traced by this fast AFM [27, 30].

Figure 7 shows the earliest evidence of nucleation in polymer samples by Chan's group [80]. In figure (A), an embryo is observed in the bottom left; while 10 min after, in figure (B), the embryo in the bottom left disappeared and a new embryo appeared in the top right. This result well agrees with the description of CNT about the non-steady nucleation state.

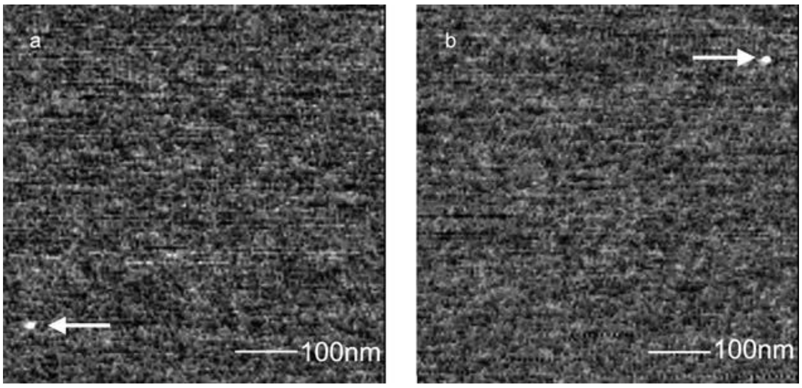

(A) (B)

Figure 7 Phase images obtained on a BA-C8 film at room temperature. (A) An embryo; (B) the embryo in (A) disappeared and a new embryo appeared at a different location [31]. (Reproduced with permission from American Chemical Society)

Besides, Chan’s group also studied the growth behavior of the same sample, BA-C8, as above. Figure 8 shows the growth of the BA-C8 copolymer crystals from an embryo to lamellae [75]. The embryo growth in front direction as well as is branching, which yielded a lamella leaf finally. The series of AFM studies by Chan’s group offered important experimental evidence of polymer nucleation and growth; however, the unique property in the crystallization rate of BA-C8 makes the result unique and cannot be repeated in other polymers [31, 75, 76, 80].

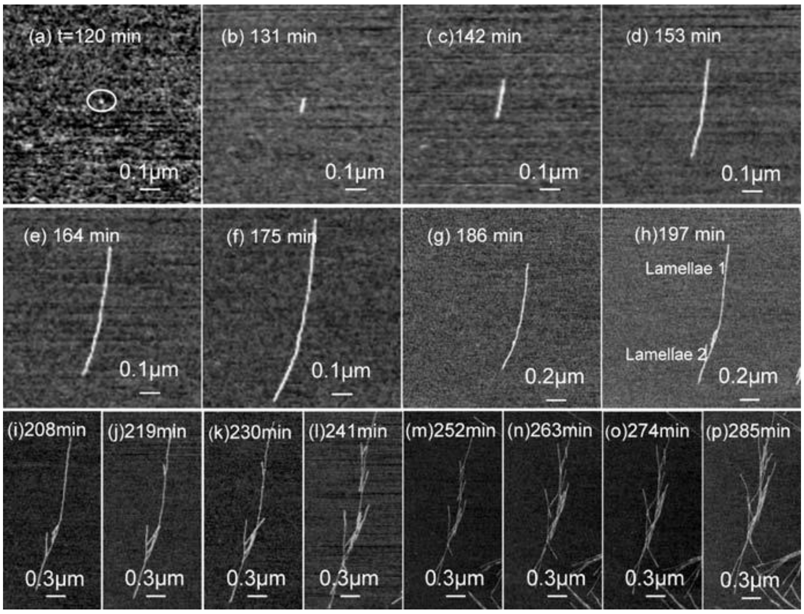

Figure 8 A series of AFM phase images obtained on a BA-C8 film at room temperature. From top left to bottom right, an embryo developed to the lamella, as shown in the images at the first two lines; branching and splaying apart of the subsidiary lamellae, as shown in the images at last line [31]. (Reproduced with permission from American Chemical Society)

By using an AFM with the fast scanner, Hobbs's group performed a real-time study on the lamellar growth of polyethylene (PE) through an *in-situ* AFM [30]. Even the result was similar to what Chan's group did; the fast AFM scanner enables to measure more polymer samples without limitations by their crystallization rates. Figure 9 shows that the PE sample formed a lamellar sheaf and yielded spherulites later [27].

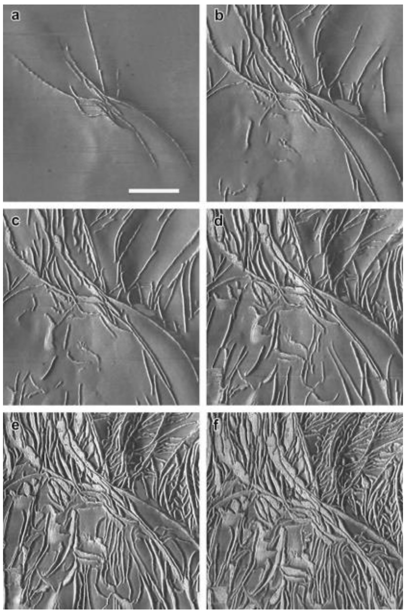

Figure 9 Crystallization of PE from lamellar sheaf to spherulite performed by a real-time in situ AFM through a quiescent melt method [27]. The first four images of them were taken at 406 K. The last two images of them were taken at 401 K and 399 K, respectively. Dark and brilliant color represents a change in phase of 50 deg and the scale bar represents 1 μm. (Reproduced with permission from Springer Nature)

Meanwhile, the *in-situ* AFM equipped with a fast scanner is also a good tool to measure the spherulites growth rate, as shown in Figure 10 [30]. The edge of the spherulite can be easily recognized by AFM, and then the growth rate of spherulites can be estimated.

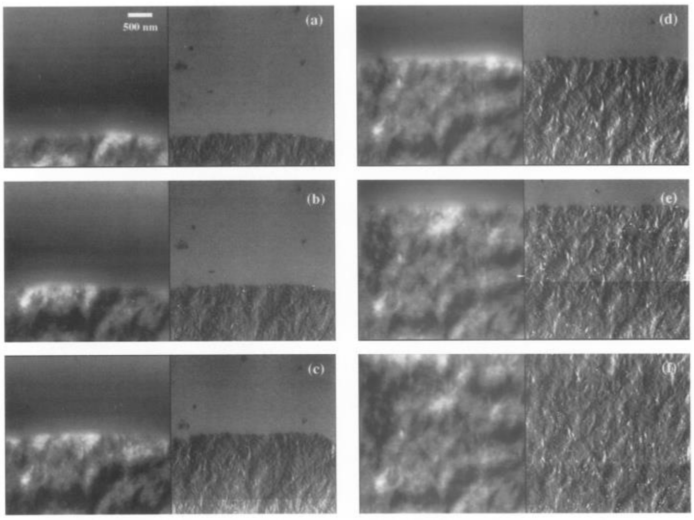

Figure 10 Real time AFM images partially showing a growing spherulite at ambient temperature [30]. The left-hand images are height images and right-hand images are phase images. Each time, AFM images were collected with 170 s intervals. Scale bar in the first image represented 500 nm. (Reproduced with permission from Elsevier)

Another important result by Hobbs's group was that they used this *in-situ* AFM to trace the crystallization of polymers at the early stage. Because the high temperature is not good for nucleation, Hobbs's group applied a stage-cooling method to cool a purified iPP sample from 313 K to 288 K at 5 K min^{-1}, as shown in Figure 11 [78]. Figure 11 (b) illustrates a particle-like crystal, corresponding to a nucleus after little growth.

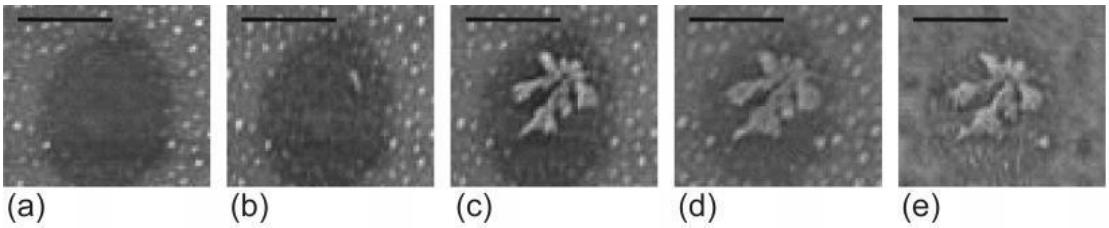

Figure 11 Real-time AFM phase images showing the crystallization of an iPP droplet during cooling [78]. Black to white represents a change in the phase of 50°. The scale bar represents 500 nm. (a) Taken at 313 K, (b) 308 K, (c) 307 K, (d) 296 K, (e) 288 K. (Reproduced with permission from American Chemical Society)

Androsch's group did a series of works on combining POM and AFM microscopy with fast temperature changes for studying polymer crystallization [55, 81]. By combining FSC with POM and AFM, the influence of crystallization temperature on morphology can be illustrated [33, 40, 52, 82, 83]. Figure 12 (A) shows the morphology of polyamide 11 (PA 11) that was quenched to 298 K from the melt and then reheated to 493 K at the rate of 5 K min^{-1}. By this method, crystallization happens at deep supercooling and homogeneous nucleation dominates. Homogeneous nucleation can overcome the limited number of active surfaces, which represent heterogeneous nucleation sites. Homogeneous nucleation leads to the expected high density of crystals. Meanwhile, the viscosity of the system increases as the temperature decreases, which yields metastable crystals rather than well-organized spherulites. Such small size, metastable crystals usually cannot be observed by POM. Figure 12 (B) shows the morphology of PA 11 crystallized on slow cooling the quiescent melt at a rate of 1 K min^{-1}. Well-organized spherulites can be observed, nucleated at low supercooling.

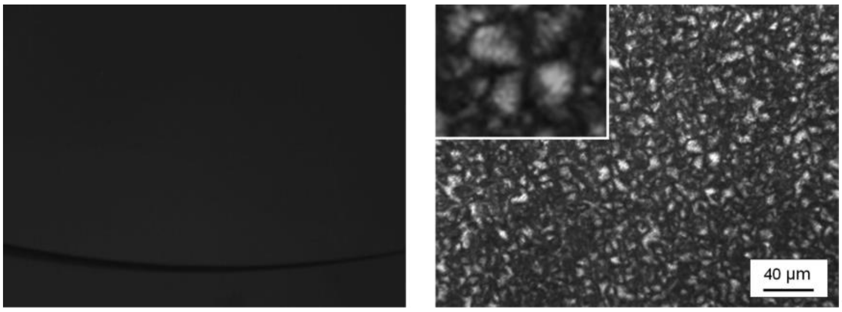

(

A) (B)

Figure 12 POM images of PA 11 crystallized on heating an initially quenched sample (left) or on slow cooling at 1 K min^{-1} (right) [40]. (Reproduced with permission from American Chemical Society)

AFM, having a better resolution than POM, was applied in combination with FSC. As shown in Figure 13 (A), the metastable crystals of PA11 could be observed. These metastable crystals show a particle-like pattern, and they seem to grow independently and form a space filling morphology. The size of metastable crystals was about 10 nm and the number were much higher than the number of spherulites in the same area. These metastable and small crystals are named nodules. This result well agrees with the expected effect of homogeneous nucleation on crystal morphology. Figure 13 (B) shows the lamellae crystals of PA 11, which were formed during slow cooling the melt at the rate of 10 K min^{-1}. The image shows edge-on viewed lamellae with a thickness of about 10−20 nm. Another example for this behavior is PA 66 annealed at 343 K and 473 K [38], as shown in Figure 14.

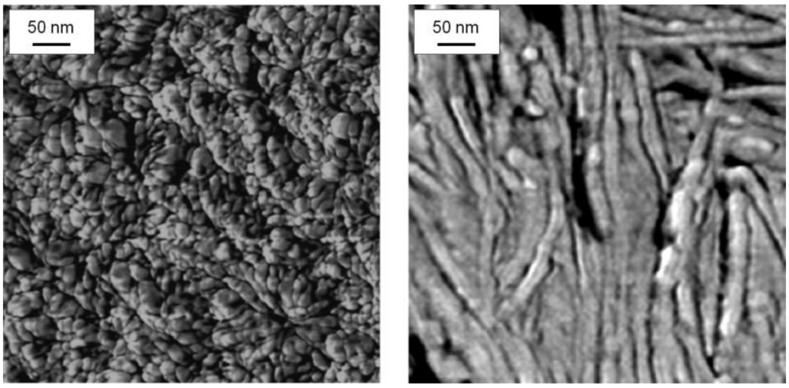

(A) (B)

Figure 13 AFM phase-mode images of PA 11 crystallized on heating and annealing an initially quenched sample at 433 K (left) or on slow cooling at 10 K min^{-1} (right) [40]. (Reproduced with permission from American Chemical Society)

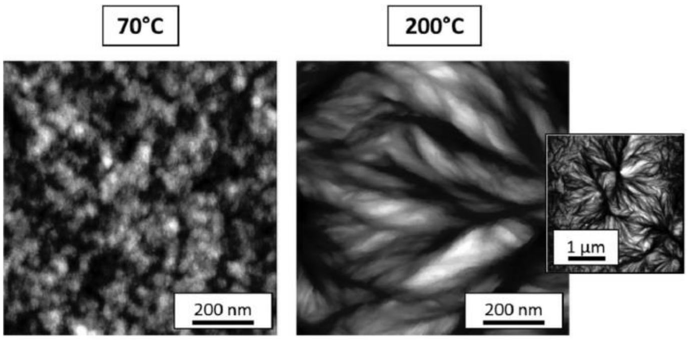

Figure 14 AFM phase-mode images of PA 66 crystallized on heating and annealing an initially quenched sample at about 473 K (left) at about 343 K (right) [38]. (Reproduced with permission from Elsevier)

These examples were used as starting points for the test of the combined AFM-FSC device in chapter 4.

3 Experimental Methods

3.1 Materials

The details of the polymer samples are listed in Table 1. Materials are used as received without further treatments, if not stated otherwise.

Table 1 Information of polymer samples

Polymer samples	Molecular Mass (g/mol)	M_w/M_n	Type	Supplier
PBT	M_w=558,600	2.25		Toray Industry, Inc, Japan
PEEK	M_w=85,000		150 G	Victrex plc., UK
PA 66	M_n=17,000~18,000		Zytel 101L	DuPont, USA
PCL	M_w=20,000	1.73		Sigma-Aldrich, USA
PLLA	M_w=117000	1.8		Sulzer Chemtec Ltd., Switzerland

M_w: weight-average molar mass

M_n: number-average molar mass

3.2 Estimating crystallinity from FSC data

For quantification of crystallinity of the sample, the sample mass was determined from the measured heat capacity step height at the glass transition temperature of the fully amorphous sample and the known step height in the specific heat capacity [84]:

$$m = \frac{\mathit{\Delta} C_p}{\mathit{\Delta} c_p} = \frac{\Delta\Phi}{ß\,\mathit{\Delta} c_p} \tag{7}$$

Where m is sample mass, β is heating rate, $\mathit{\Delta} C_p$ is apparent heat capacity from experiment, $\mathit{\Delta} c_p$ is specific heat capacity at glass transition and $\Delta\Phi$ is measured heat flow step at the glass transition of the fully amorphous sample. Crystallinity (X) was determined as the ratio between the measured heat of fusion and the known heat of fusion of the 100% crystalline polymer:

$$X = \frac{\Delta h}{\Delta h^{\infty}} \tag{8}$$

where Δh^{∞} is heat of fusion of the 100% crystalline material, which is availble from the ATHAS data bank.

3.3 Combined AFM - FSC device

The experimental challenge for my thesis work was the construction, testing and application of a combined AFM-FSC device, not reported before. This combined device was foreseen for detailed studies of polymer crystallization. The development of the combined device was guided by my final task of studying homogeneous crystal nucleation kinetics.

The AFM is a Level AFM from Anfatec, Germany, which can work in two modes [85]. It includes contact mode and non-contact mode. To avoid unwanted cantilever-tip induced crystallization, non-contact mode has been applied here. Simultaneously recorded was topology from height, phase-angle and amplitude of tapping. AFM probes used are standard silica cantilevers, and the parameters are listed in Table 2.

The sample holder of the AFM on top of the scanner tube was replaced by a socket for the TO5 housing of the FSC chip. Chips from Xensor Integration, Netherlands, [86, 87] mounted on a TO5 housing allow direct access of the sample by the AFM probe, as shown in Figure 15 (A). AFM probe scanning on the sample on the chip-sensor is shown in Figure 15 (B). A second empty calorimeter chip, the reference sensor, is placed next to the AFM inside a temperature-controlled box. Both chip sensors are connected to the FSC electronics as described elsewhere [88, 89].

Table 2 Information of AFM probe used in this thesis

AFM probe	Supplier	Resonance frequency (KHz)	Tip radius (nm)	Spring-constant (N m^{-1})	Coating on backside	Ref.
NSC 14	μmasch, USA	110 - 220	8	5	Aluminum	[90]
Scout 70	Nunano, UK	70	5	2	Gold	[91]

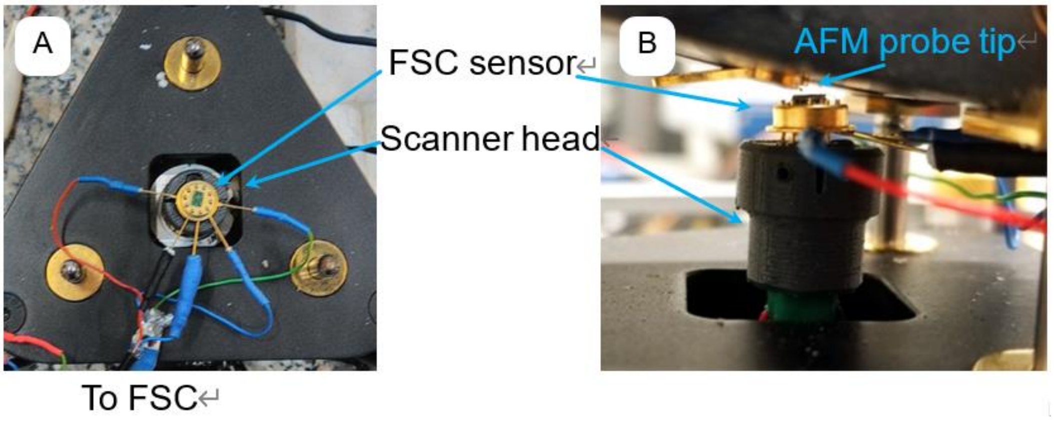

(A) (B)

Figure 15 (A): Photograph of mounting FSC sensor on the AFM scanner. (B): AFM probe approaching the sample on the sensor.

For the unperturbed operation of the FSC as well as the AFM the open/uncovered sensor in the combined device needs to be decoupled from uncontrolled environmental influences like temperature oscillations, airflow or sound waves. A protecting box made by 5 mm acryl glass sheets was placed over the AFM and thermally isolated by 30 mm foamed polystyrene, as shown in Figure 16. The temperature inside the box was reduced to 278 K by a cold finger of a mechanical refrigerator, FT 100, Julabo, Germany. Nitrogen purge was used to ensure dry conditions. The construction allowed mechanical stabilization of the chip sensor and the sample for good quality AFM imaging. At the same time, FSC experiments can be performed without changing the position of the sample. The reduced temperature inside the protecting box slightly extended the range of materials for investigation and the cooling performance of the FSC.

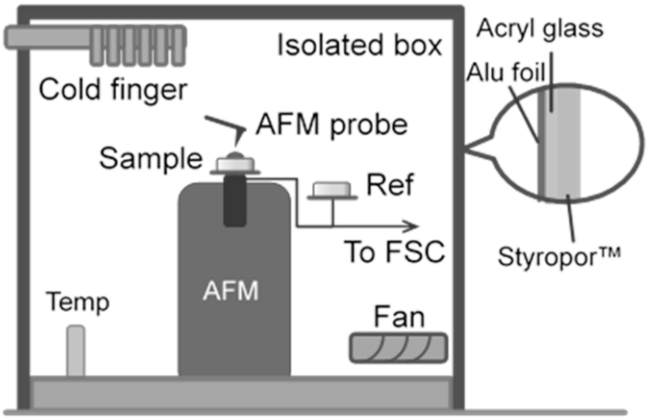

Figure 16 Schematic diagram of the cooling box of AFM-FSC.

3.4 Sample preparation and AFM adjustment

Before mounting the chip sensor in the AFM, the sample was placed on the calorimeter chip sensor under an optical microscope, as described elsewhere [37]. After mounting the sensor in the AFM, polymers were heated several times to above the melting temperature until a stable shape of the sample was reached. A first AFM image of the whole sample was then collected in a non-contact mode in 278 K. Rather flat surface areas near the center of the drop-like sample for more detailed studies were identified from this image, see Figure 17 (B).

The sample on the chip-sensor is generally close to a spherical cup, as shown in Figure 17 (A) and (B). The probe was placed next to the center of the sample, which is available from the optical micrograph, see Figure 17 (A). Due to the limit in the maximum scanning range of 2 µm for the Z-scanner (with Z being the vertical direction), the whole image of the sample of height ca. 10 µm was not available. Close to the sample edge, the scanner lost the signal and imaging was not possible in the area labeled d_3 in Figure 17 (B). In order to increase the accessible area, the reference amplitude was set at a place outside the center by d_1. The corresponding AFM images and more details on AFM adjustment are shown in Figure 17 (C)-(F).

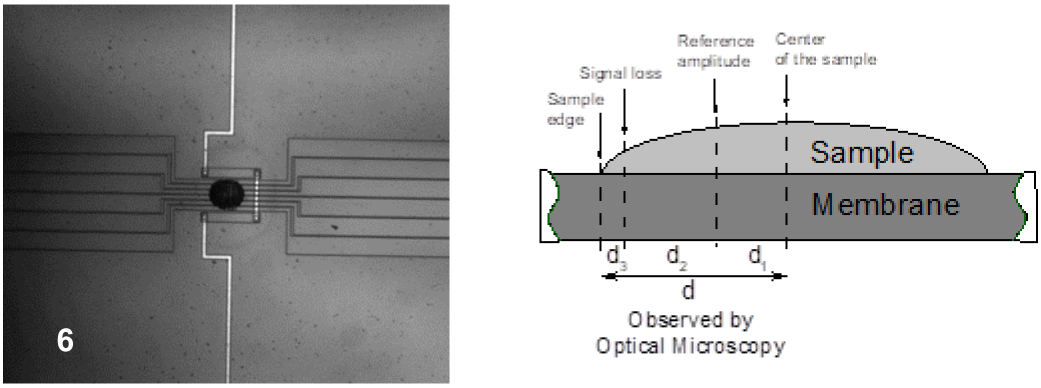

(A) (B)

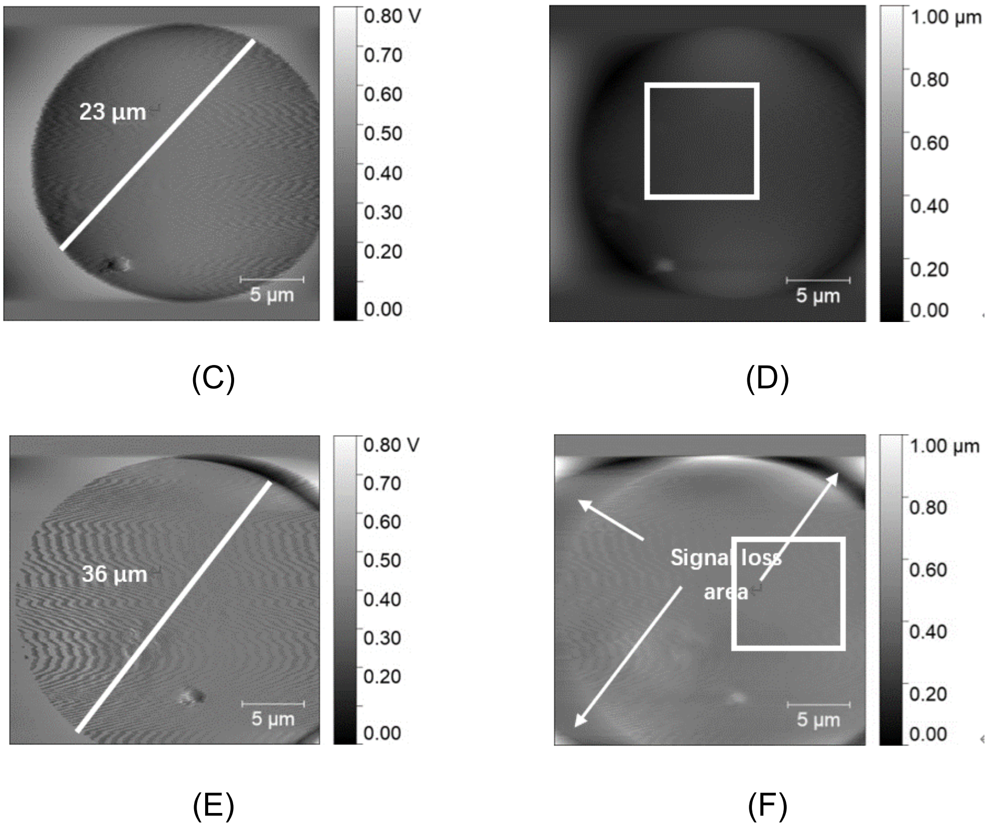

Figure 17 (A) Optical microscopy image of a poly (ether ether ketone) (PEEK) sample on the chip-sensor. (B) Schematics of setting the reference amplitude of the cantilever for the AFM measurement. (C) and (D) AFM images of PA 66 to show the increase of accessible area. AFM image of the sample using the sample center to set the reference amplitude. (E) and (F) AFM image of the sample using the optimal place to set the reference amplitude.

4 Investigation on polymer nucleation and crystallization by AFM-FSC

4.1 Influence of tip induced nucleation and crystallization

4.1.1 *In-situ* imaging during crystallization of PCL

As the first example, we present images *in situ* collected during expected slow crystallization of PCL at low undercooling. Even the anticipated results were not obtained, we present this example to highlight the problems of *in situ* AFM during crystallization and, next, to show how fast scanning calorimetry in combination with AFM can overcome these limitations elegantly and advantageously. The PCL sample was thermally treated according to Figure 18 (A). It was heated above the melting temperature at 450 K firstly and then quenched to 325 K. According to Zhuravlev et al. [66], a half-time of crystallization ($t_{1/2}$) of 10^5 s is expected for crystallization at 325 K. With about 2000 s needed to capture the AFM image, it should be possible to collect about 50 AFM images before half of the sample is crystallized.

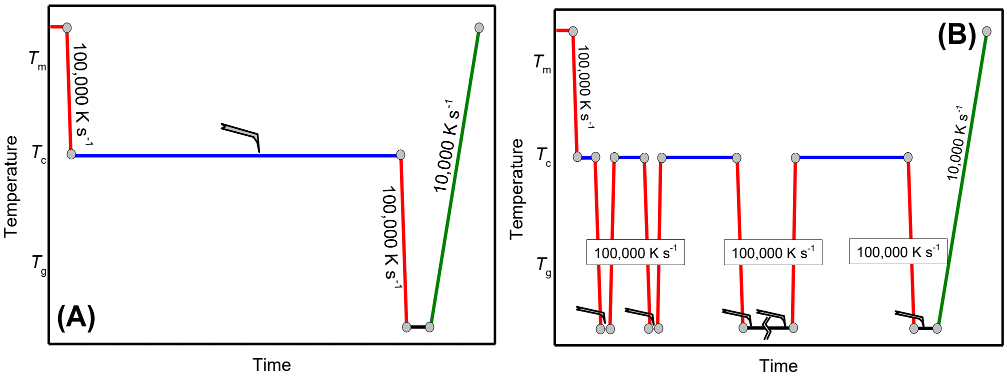

Figure 18 Time-temperature program for studying isothermal crystallization by AFM-FSC combination. (A) – taking AFM images during slow crystallization at a temperature either close to $T_{m,0}$. Or (B) – time-resolved imaging, using ultra-fast cooling and heating ability of FSC. In both cases, the final FSC heating scan after crystallization is taken at 10,000 K s^{-1} starting at ambient temperature.

Figure 19 shows AFM images collected at 325 K between 1000 s and 3000 s (A and B) and between 3000 s and 5000 s (C and D) after quenching from the melt. Unexpectedly, the images are almost identical. A spherulitic structure can be seen already in Figure 19 (A) and (B), but no additional structures are formed even during further annealing for half an hour ((C) and (D)), suggesting that the whole process of crystallization almost completed after 3000s. However, this result is significantly different from the crystallization kinetics of PCL reported by Zhuravlev et al. [66]. Fortunately, the combined AFM-FSC device offers a possibility to identify the reason for this discrepancy. According to the temperature-time profile of Figure 18 (A), the FSC heating scan has been recorded after taking the AFM images of Figure 19 (B).

In accordance with the AFM images, a dramatic crystallinity developed within the total time of 5000 s at 325 K. A melting peak of 0.66 μJ is seen in curve (A) of Figure 20. Removing the AFM probe and annealing the PCL at 325 K for the same time does not result in a measurable melting peak, curve (C) in Figure 20. A comparable melting peak of 0.76 μJ is only observed after annealing for 100,000 s at 325 K with the AFM probe far away from the sample surface, curve (B) in Figure 20. The roughly similar peak positions ($T_{\mathrm{m,onset}}$ ca. 337 K; $T_{\mathrm{m,peak}}$ ca. 353 K) indicate comparable lamellae thicknesses for the crystals grown at 325 K, independent of the nucleation pathway. In order to determine the mass, the sample was tested by FSC with a liquid nitrogen cooling system. The glass transition step of the fully amorphous sample yields the sample mass of ca. 14 ng. Crystallinity estimated by equation (2) was ca. 30% and 35% for the curve (A) and curve (B), respectively. Here we used specific heat of fusion of fully crystalline material from the ATHAS databank: $\Delta h^{\infty} = 156.8$ J g^{-1}. Nucleation kinetics dominates the crystallization kinetics at the low undercooling of about 15 K. The experiments with the AFM probe near the surface obviously show enhanced nucleation.

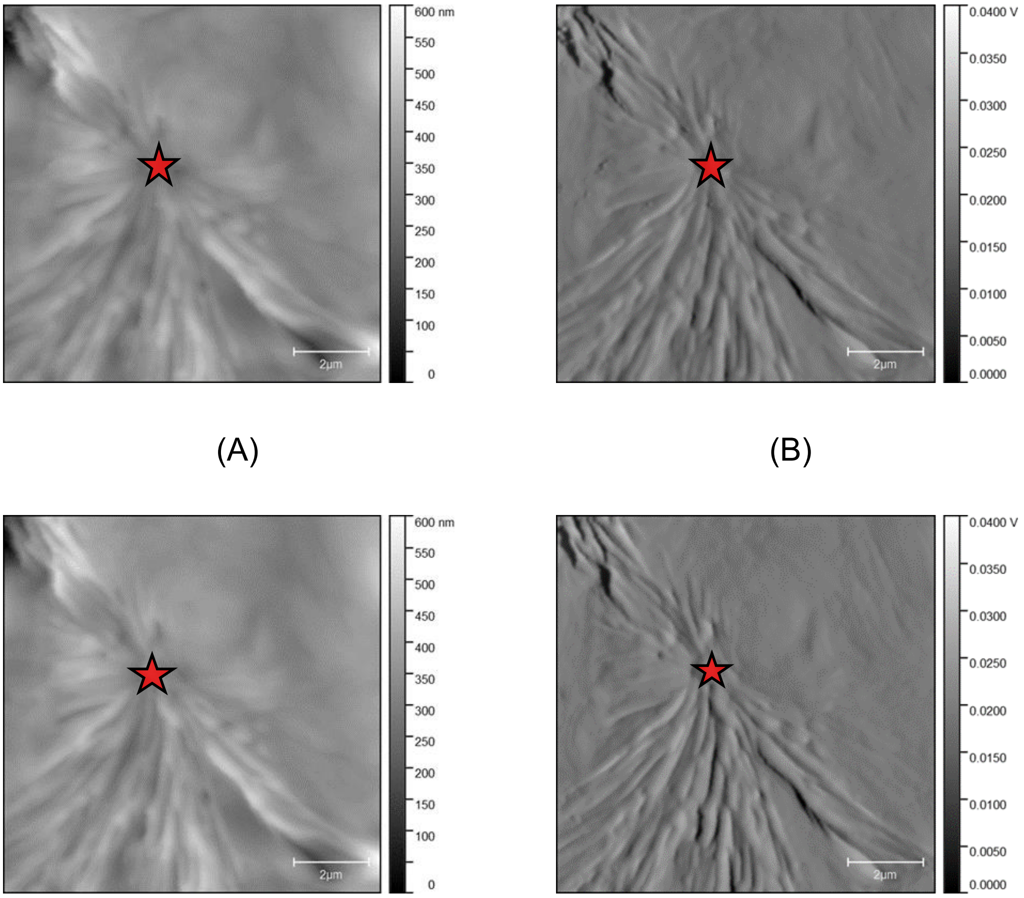

(A) (B)

(C) (D)

Figure 19 AFM images of PCL annealed at 325 K. The left column shows topology and the right column amplitude images. Images (A) and (B) are collected between 1000 and 3000 s and images (C) and (D) between 3000 and 5000 s after the quench.

A star marks the position of the nucleus of the growing spherulite in Figure 19. This position is the place where the AFM tip initially approaches the sample surface before imaging starts in horizontal lines from the top of the images. The approach of the AFM tip to the surface takes about 1,000 s. During this time, a nucleus is formed, even if the AFM tip does not touch the sample surface. The reason for this localized nucleation is not yet known. At least two possible effects must be considered. On the one hand, the AFM tip locally cools the sample surface and may enhance the formation of a nucleus just at the place of lowest temperature. On the other hand, the tip interacts through Van der Waals forces with the sample, which is of the order of 10^{-12} N for a distance of 5 to 10 nm between the AFM tip and the sample. AFM-tip-induced nucleation is a known phenomenon and discussed in several publications, e.g. [92].

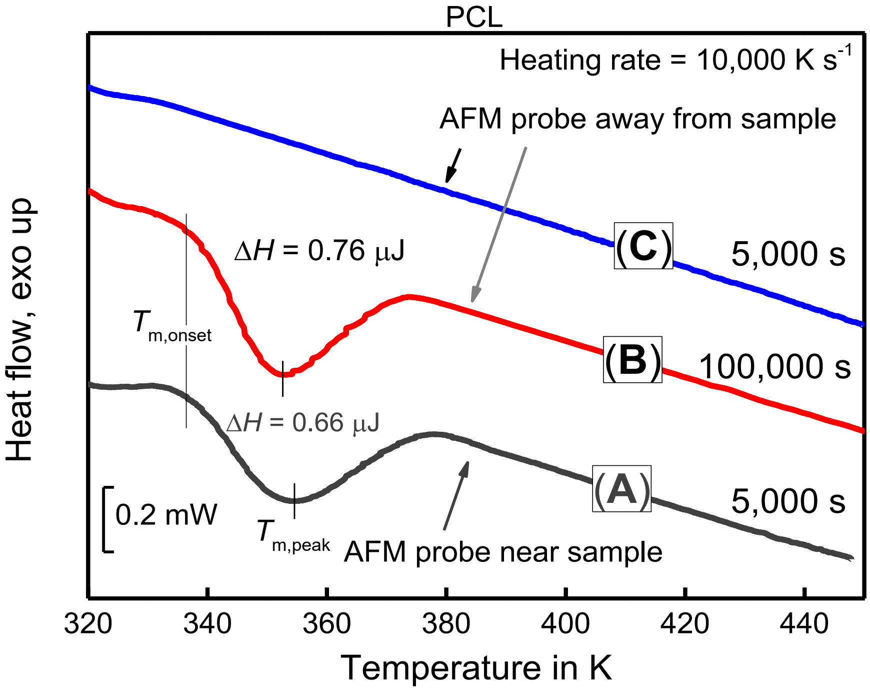

Figure 20 FSC heating scans of PCL after annealing at 325 K under different conditions regarding the placement of the AFM probe. Curve (A) – After collecting the images of Figure 19 (5000 s at 325 K, AFM in non-contact mode, about 5 – 10 nm distance to the sample). Curve (C) – Same annealing time at 325 K as in the case of Curve (A) but with the AFM probe about 100 µm away from the sample. Curve (B) – AFM probe far away from the sample and annealing time at 325 K increased to 100,000 s.

The fact is that interaction between AFM tip and sample is very weak, but it still influences on the crystallization behavior of polymers, which makes an *in-*

situ investigation of isothermal polymer crystallization at the crystallization temperature difficult. Before further improving the experiment method, a key point here is how the tip introduces the nuclei at the surface of the sample. In the following chapter, the mechanism of tip-induced nucleation will be studied through analyzing the three-dimensional quasi-single crystals of PCL grown after tip-induced nucleation.

4.1.2 Tip induced nucleation and crystallization

The temperature-time program follows Figure 18 (A). The PCL sample was melted at 400 K for about 0.01 s at first and quenched to 330 K. Then, AFM images were collected during isothermal annealing at the quenching temperature. After annealing at 330 K for 70 min, the sample was cooled to 278 K and reheated to 400 K at the rate of 10,000 K s^{-1}. Then the progress of crystallization can be evaluated from the reheating curve. To introduce nuclei by AFM, the following approach was applied, which contains four steps: 1) The tip approaches the sample at a location near the center in non-contact mode. The sample is hold at 330 K. After that, the tip is moved 30 µm away from the sample. 2) The temperature-time program of Figure 18 (A) is started and the tip approached the sample, which is hold at 330 K, again and introduces a nucleus through an instant contact. 3) The tip detaches the sample again and the resonance frequency is adjusted. 4) The tip moved back to the sample surface and scans continuously. The time of the AFM tip needed to approach the sample surface was about 19 min, and each AFM image required 20 min to record. The AFM image consists of 512*512 pixels.

The tip-induced nucleation can happen along two different paths. The first one is that some weak stresses generated when the tip is tapping the sample surface. These stresses can introduce some tiny ordered structures and yield some kind of heterogeneous nucleation. Another one is that the temperature near the tip is lower compared to the undisturbed parts of the sample surface, which will result in a deeper supercooling at the places of tapping. The deeper supercooling will enhance homogeneous nucleation.

As shown in the AFM topology image of Figure 21 (A), a bar pattern is observed in the center, indicating the interaction between tip and sample. To estimate the maximum value of stress, which the tip can produce at the contact place on the sample, Hooke's law is applied

$$F_{tip} = A_{cant} * K \tag{9}$$

where A_{cant} is the maximum amplitude of free cantilever, 8.8 nm and K is the spring-constant. Then F_{tip} is determined as 4.4 * $30.8*10^{-9}$ N. According to Zhu et al. [93], this small value caused by soft tapping cannot induce heterogeneous nuclei in polymers. Therefore, the mechanism of the tip-induced nucleation and crystallization should be due to homogeneous nucleation caused by local cooling.

The growth of crystals through the active centers of homogeneous and heterogeneous nuclei follow different ways, which will yield different morphologies during growth [76]. This difference will be apparent in the corresponding single crystal structure. Geil reported a double spiral growth in a single crystal of polypropylene [5]. The double spiral growth indicates that the nuclei more likely grow in one diagonal than another, which corresponds to heterogeneous nucleation [61, 94], see Figure 21 (B), left. Contrary, the active centers of homogeneous nuclei should have the same possibility of growth in all directions. This will lead to a round-like single crystal [95], see Figure 21 (B), right.

Reiter's group reported a three-dimensional quasi-single crystal formed at the sample surface for temperatures near melting [57, 95, 96]. According to the description of differences in homogeneous and heterogeneous nucleation above, the scheme adopted to quasi-single crystals is shown in Figure 21 (B). In Figure 21 (C), the AFM phase image for PCL annealed at 330 K for about 70 min is shown. Stack-like crystals are observed. These crystals can be thought as the piling up of single crystals [57]. By further zoom-in the square area with 4×4 μm^2, a round-like pattern can be observed in Figure 21 (D). Round-like rather than double spiral crystal in the single layer of the stack-like crystals has been observed, suggesting that the tip induced nucleation is homogeneous.

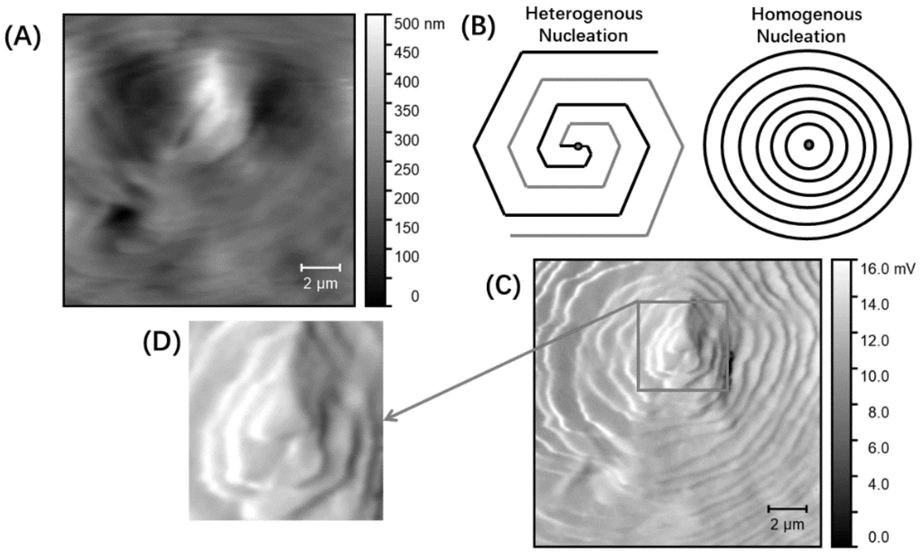

Figure 21 (A) AFM topology image after annealing 30 min at 330 K. (B) Scheme of heterogeneous and homogeneous nucleation in flat-on lamellae [61, 94, 95]. (C) and (D) are the AFM amplitude and zoom-in images after annealing 70 min at 330 K. Zoom in area is marked as the square in figure (C).

Fortunately, the AFM combination with the FSC allows for well-defined interruption of the crystallization process and collecting images at low temperatures where crystallization does not proceed, see Figure 18 (B). This strategy is next applied to follow spherulite growth in poly (ether ether ketone) PEEK.

4.1.3 Linear Growth Rate of PEEK Spherulites

PEEK is an intermediately fast crystallizing polymer. But the behavior goes too fast to allow *in-situ* AFM imaging during crystallization at temperatures near the maximum of the crystallization rate at about 500 K. Nevertheless, the interrupted crystallization, as illustrated in Figure 18 (B), allows for a detailed investigation of spherulitic growth on length scales below that accessible by POM. The PEEK sample was cooled from 680 to 564 K at 100,000 K s^{-1} and then annealed for 0.01 s at this temperature. Afterward, it was cooled down to 300 K at 100,000 K s^{-1} to take the AFM image. The 300 K is significantly below T_g of about 430 K, avoiding any crystallization during the collection of the AFM image. After taking the AFM image, the sample was heated back to 564 K at 100,000 K s^{-1} and crystallization was allowed to continue for another 0.09 s. The next AFM image was again taken after quenching at 300 K. Consequently, the total annealing time before the collection of the second image was 0.1 s. This way, AFM images of the PEEK sample were taken after cumulative annealing times of 0.01, 0.1, 1, 2, 4 and 10 s. Finally, after all AFM images collected, the sample was heated to 680 K and the melting curve was recorded, as shown in Figure 22 curve (B). The curve (A) of Figure 22 shows the heating scan after quenching the melt to 300 K, verifying the amorphous state of the sample. For this sample, T_g was about 427 K. Sample mass was around 39 ng, determined from Eq.(7), using the measured heat capacity step at the glass transition ΔC_p (T_g = 427 K) = 10 nJ K^{-1}. Crystallinity from curves (B) and (C) were ca. 9%. The values taken from the ATHAS databank were: Δh^{∞} = 130 J g^{-1} and Δc_p = 0.254 J g^{-1} K^{-1}.

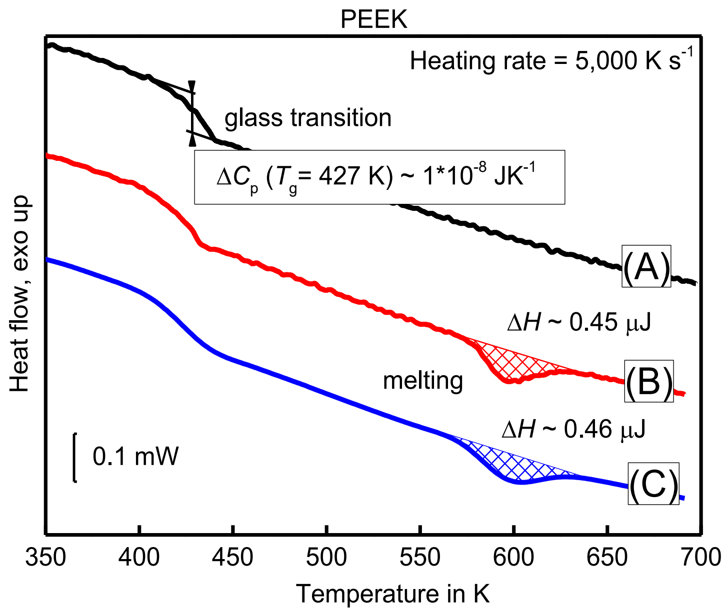

Figure 22 FSC heating curves of PEEK recorded using a rate of 5,000 K s^{-1}. (A) – after quenching the melt to 300 K, (B) – after interrupting annealing at 564 K for a total time of 10 s and (C) – after annealing at 564 K for 10 s without interruptions, according to the temperature-time program in Figure 18 (B) and (A), respectively.

Figure 23 is the AFM images collected at 300 K, after annealing for different annealing time at 564 K, as described above. After one second annealing, the first spherulites show up. With increasing annealing time, the size of the spherulites is increased, and the spherulites are nearly space-filling after 10 s annealing at 564 K. Since crystallinity from the curves in Figure 22 are below 10%, space is filled only at the surface but not in bulk. The AFM-FSC combined device allows following the growth of one and the same spherulite as illustrated with the images of Figure 23. Even the sample is quickly heated and cooled to and from the annealing temperature, the images always have the same spot. The high reproducibility of the position of the AFM tip allows measuring the size of the spherulites as a function of annealing time. The white lines in Figure 23 correspond to the distance between the center and the edge of the investigated spherulite. This way the spherulite radius as a function of time was determined and the growth rate equals the slope of the line in Figure 24 (A).

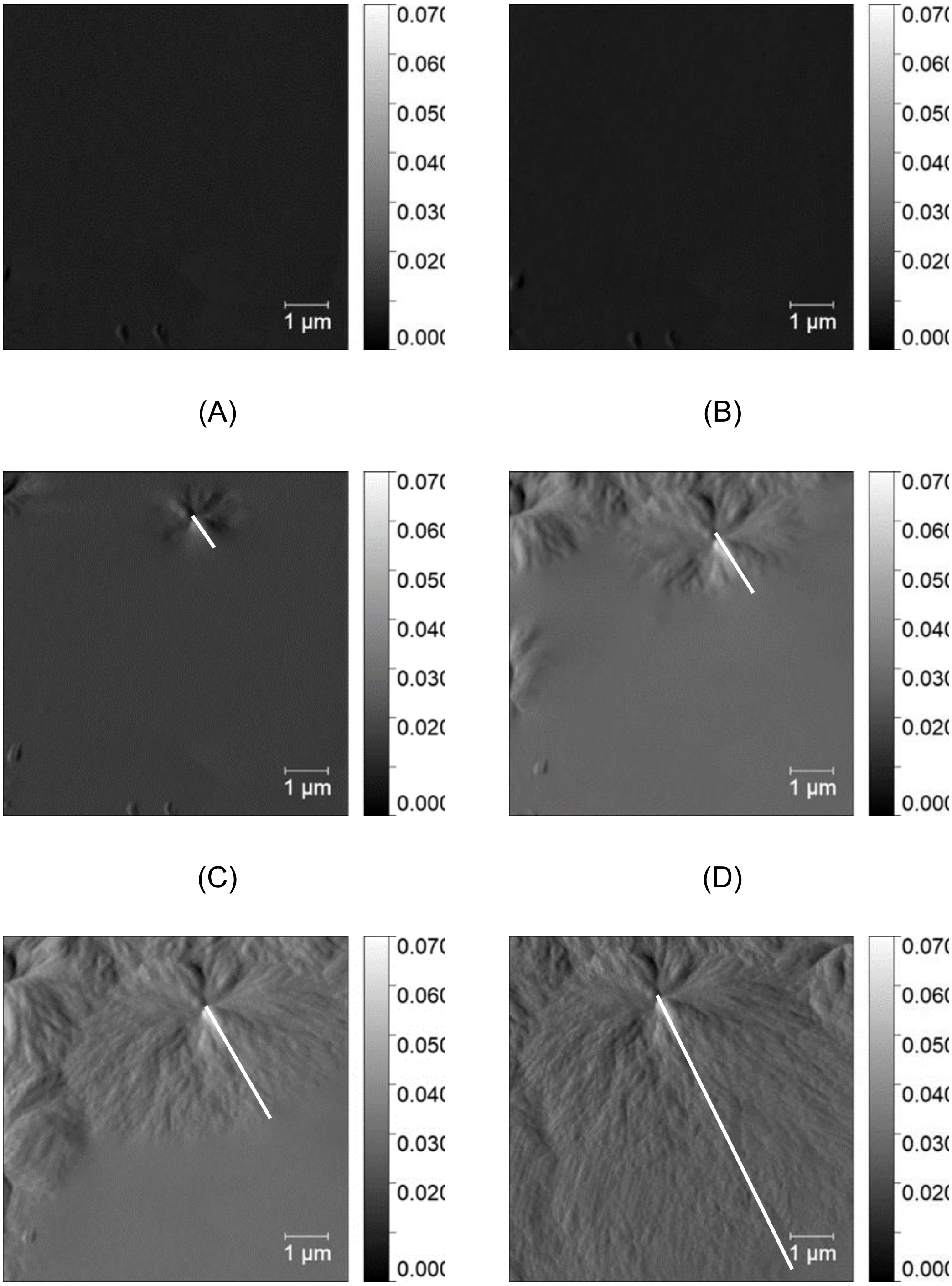

(A) (B)

(C) (D)

(E) (F)

Figure 23 AFM amplitude images showing an area of 8*8 µm^2. PEEK annealed at 564 K for 0.01 s (A), 0.1 s (B), 1 s (C), 2 s (D), 4 s (E) and 10 s (F). The reason for the slight asymmetry of the growth rate in the direction of the blue line and perpendicular to it, images (D) and (E), is not yet known and was not investigated.

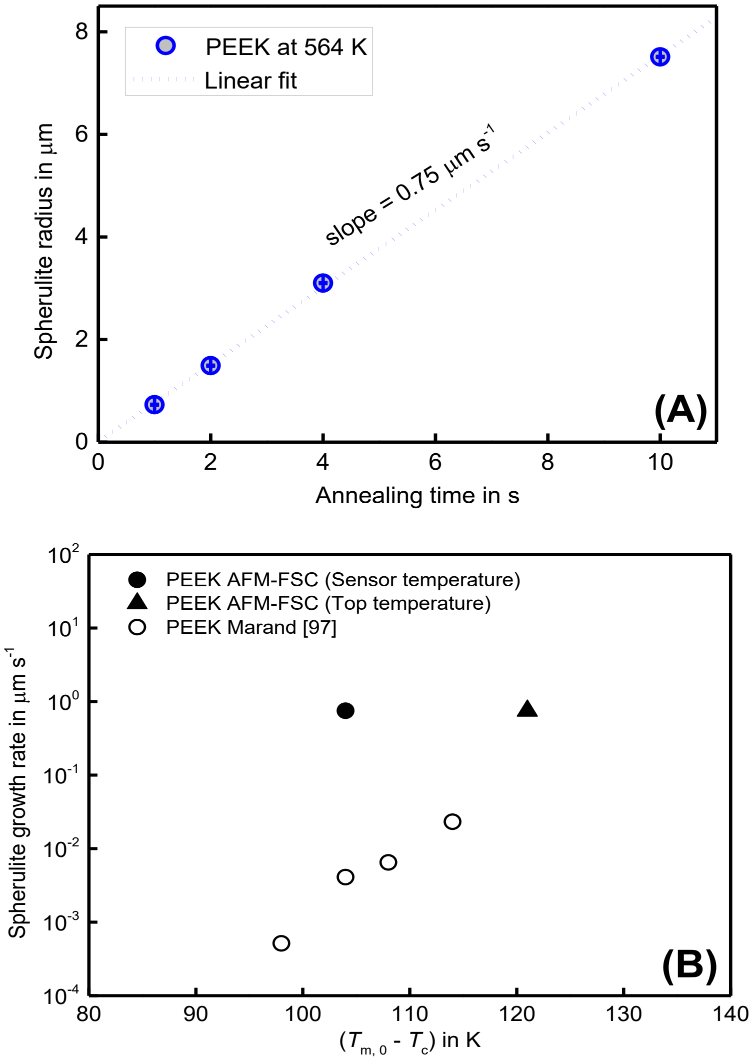

Figure 24 (A): Spherulite radius vs. annealing time for PEEK at a sensor temperature of 564 K by AFM-FSC. (B): Spherulite growth rates of PEEK measured by AFM-FSC and POM as function of undercooling below $T_{m,0}$.

The slope of the data in Figure 24 (A) yields a linear growth rate of 0.75 μm s^{-1} at a sensor temperature of 564 K. The observed linear growth rate is much higher than the POM data reported by Marand et al. [97], as shown in Figure 24 (B). There are several possible explanations: (i) The speed of crystal growth at the surface is faster than that of the bulk due to enhanced surface mobility [98]. (ii) The surface of the sample on the FSC chip is colder than the membrane, where the temperature is measured [88]. To prove if (ii) could explain the discrepancy, in addition to the membrane temperature the surface temperature of the FSC sample was measured. A possible temperature gradient perpendicular to the sensor membrane is caused by a heat flow from the heated membrane to the cold gas in the surrounding [68, 88, 99]. To measure the real temperature on the top of the sample, one tin particle was placed on the sensor membrane beside the sample and a second one on top of the sample, and the sample was heated and cooled at various rates spanning from 1000 to 10,000 K s^{-1}, Figure 25 (A). The extrapolated peak onset temperatures are plotted versus the heating rate in Figure 25 (B).

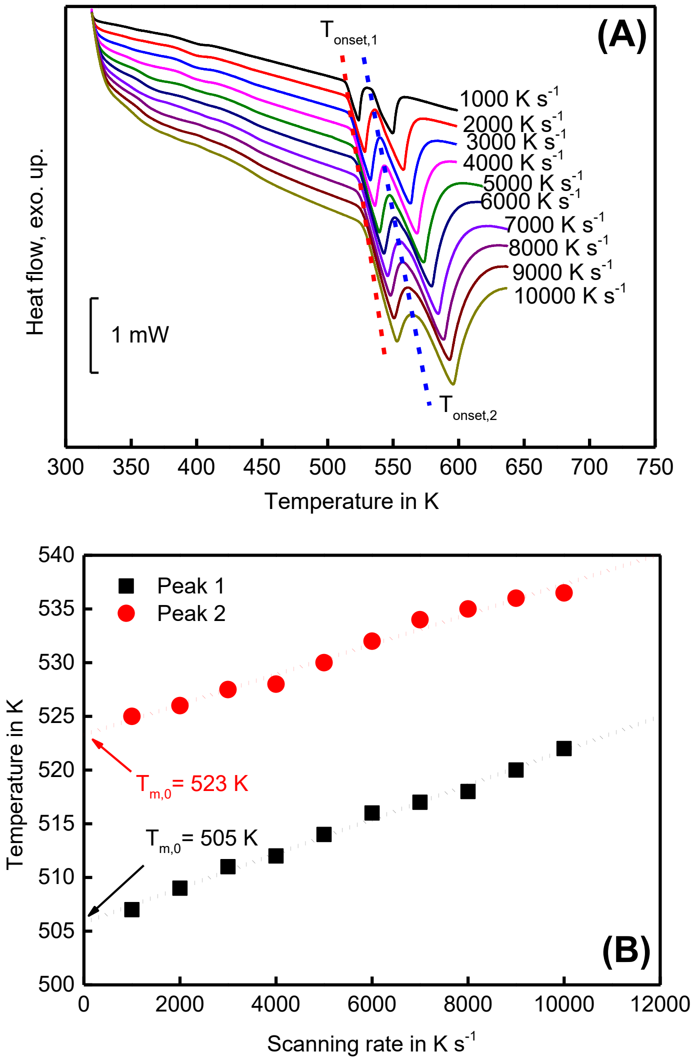

Figure 25 (A): FSC heating scans of a tin particle placed on top of the PEEK sample, yielding the high temperature melting peak, and a tin particle placed beside the sample directly on the sensor membrane, yielding the low temperature melting peak. (B): Melting peak onset temperatures against scanning rate. Tin sample on the sensor (red dots) and tin sample on top of the PEEK sample (black squares).

The extrapolation to zero heating rate of the melting peak onset temperature [100] provides apparent melting temperatures of 505 and 523 K, corresponding to the tin sample on the membrane and top of the PEEK sample, respectively. This evidence indicates that there is an 18 K temperature gradient between the sample top and sample bottom at tin melting temperature. In this case, since spherulites at the top of the sample are investigated, the crystallization temperature in this study is 546 K, when assuming a linear temperature-dependence of the offset. Considering the surface temperature as 546 K, the spherulite growth rate is in agreement with the POM data reported by Marand et al. [97], see Figure 24 (B). Compared to classical POM spherulite growth rate analyses, AFM has an advantage for following spherulite growth at earlier stages, when the structure is too small for POM imaging. Furthermore, the FSC curves after a total annealing time of 10 s were also recorded and are shown in Figure 22. If necessary, heating scans can be recorded after shorter annealing times, but the experiment must to be again conducted from the very beginning if the final stage is of interest too.

4.2 Melt-recrystallization of PLLA

As discussed in the previous section, the tip-induced nucleation and crystallization can be avoided through the method described by the temperature-time profile in Figure 18 (B). In this section, the *in situ* AFM-FSC is applied to study the melt-recrystallization behavior of PLLA. Because melt-recrystallization strongly depends on the nucleation density, this study can further check whether tip-induced nucleation and crystallization is avoided or not during the experiment following the temperature program of Figure 18 (B).

The melt-memory effect has been found in many polymers [101-103]. The crystals were melted first; and then the sample was annealed at this temperature to recrystallize. Because of the melt-memory effect (remaining nuclei), the morphology of crystals can recover to the morphology before the first melting. The corresponding temperature-time profile is shown in Figure 26. First, the PLLA sample was cooled down from 493 K to 333 K at 1000 K s^{-1}. Second, the sample annealed at this temperature for 1000 s to nucleate and transferred to 363 K at 1000 K s^{-1} for growth for 500 s. These two segments enable to nucleate PLLA at a low temperature and to grow these nuclei to crystals at a higher temperature. Third, the sample was reheated to 440 K at 100 K s^{-1} to melt the existing crystals. What’s more, the sample was further annealed at this temperature to recrystallize. This isothermal segment follows the idea in Figure 18 (B), which represents the discrete method. AFM images can be taken during the gap between two isothermal segments at 440 K. Finally, the sample was reheated to 498 K at 100 K s^{-1} to illustrate the melting behavior of the crystallized sample.

The heating scans 1 and 2, as illustrated in Figure 26, and a heating scan of a quenched sample are shown in Figure 27. The heating curve after quenching shows an enthalpy relaxation peak near the glass transition region. No melting peak is seen in the reheating curve, suggesting a crystals-free sample. Besides, the heating scan 1 shows the melting enthalpy that the sample crystallized through Tammann’s two-stage crystallization method. In addition, the heating scan 2 shows the melting enthalpy for the sample recrystallized at 440 K for 200 s. The onsets of the melting peaks of heating scans 1 and 2 are 403 K and 440 K, respectively.

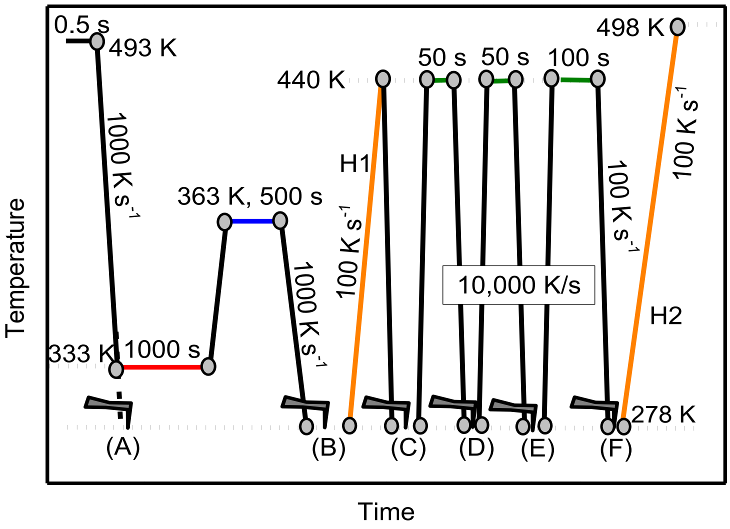

Figure 26 Temperature-time profile of the discrete strategy of AFM-FSC measurement for following melt recrystallization. H1 and H2 correspond to heating scan 1 and heating scan 2, respectively.

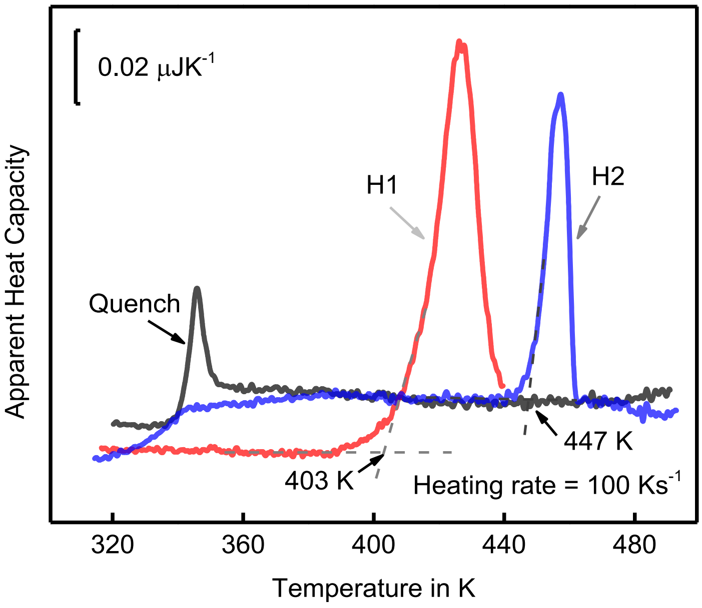

Figure 27 FSC heating curves of the quenched sample, H1, and H2 in Figure 26. H1 and H2 correspond to heating scan 1 and heating scan 2, respectively. The total time at 440 K before H2 was 200 s.

In Figure 28, a series of AFM images shows the morphology of PLLA after thermal treatments described in Figure 26. Figure 28 (A) represents the morphology of the quenched sample. The image shows a structure-free morphology, which agrees with the FSC heating scan after quenching. Besides, Figure 28 (B) shows the morphology of the crystals formed through Tammann's two-stage crystallization method, nucleation at 333 K for 1000 s and development at 363 K for 500 s. The non-spherulitic crystals fill the whole AFM image. Figure 28 (C) shows the morphology after the sample was heated to 440 K and then immediately quenched to ambient. The image changes back to a structure-free morphology, suggesting the crystals formed through Tammann's two-stage crystallization method fully melted. In addition, the images in Figure 28 (D) – (F) show the morphologies of PLLA that was recrystallized at 440 K for 50 s, 100 s and 200 s, respectively. A similar crystal morphology as shown in Figure 28 (B) was observed. This result shows that the sample was first totally molten and then re-crystallized to a morphology similar to the original non-spherulitic morphology. At the positions of the original crystals some melt-memory remains and allows recrystallization of PLLA at the same positions.

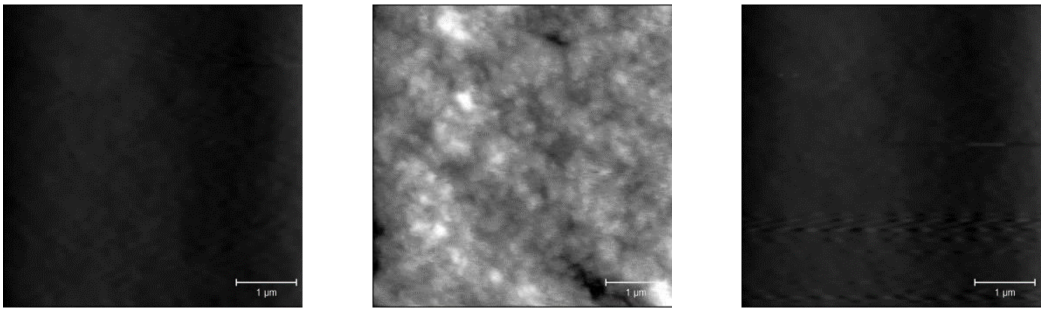

(A) (B) (C)

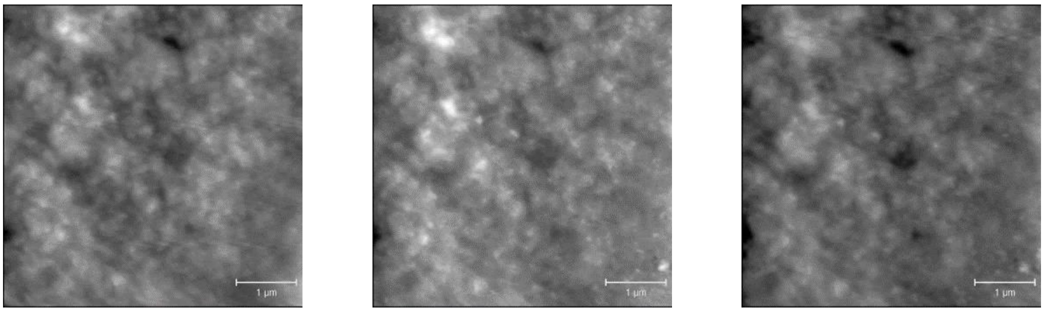

(D) (E) (F)

Figure 28 AFM images corresponding to Figure 26. A: quenched; B: two stage crystallization; C: reheated to 440 K at 100 K s^{-1}. D: recrystallized 50 s. E: recrystallized 100 s. F: recrystallized 200 s. Scale bar represent 1 μm.

The re-crystallization caused by the melt-memory effect highly relies on the number of available nuclei. The result above suggests that the nucleation density kept constant during recrystallization, indicating that the tip-induced nucleation and crystallization was avoided in this experiment.

4.3 Observing non-spherulites crystals under deep supercooling

As discussed above, tip-induced nucleation and crystallization can be avoided during the interrupted *in-situ* AFM-FSC study; while another problem here is whether the resolution of the *in situ* AFM-FSC can meet the requirement of observing non-spherulitic crystals. The sample used for *in situ* AFM-FSC is a non-flat droplet. The sample surface would contain some folds in case of multiple quick heating and cooling treatments. These areas are not good for AFM imaging. To further examine the performance of the AFM-FSC combined device, an experiment following the method reported by Gohn et al. has been repeated [38]. PA 66 was crystallized for 1000 s at 350 and 480 K, respectively. The isotherm was chosen long enough to allow for the completion of crystallization. The sample was cooled at 100,000 K s^{-1} from 580 K to 480 K or 350 K, respectively, annealed for 1000 s and afterward cooled to 278 K for AFM imaging. This temperature is below the T_g of polyamide 66 (PA 66) of about 323 K [104] and allows imaging without further crystallization. Finally, the sample was re-heated to 580 K to investigate the melting of the formed crystals. AFM images of topology in the left and amplitude in the right, of PA 66 crystallized at the two annealing temperatures are shown in Figure 29. Lamellae are observed after crystallization at 480 K; however, in the same scanning area of this sample, after crystallization at 350 K the lamellae are replaced by non-lamellar particle-like objects, with an apparent size of about 30–50 nm. If these objects are composed of smaller domains as discussed by Baer et al. [105] or the image is influenced by tip-smearing [106], is outside the scope of the present thesis. Nevertheless, this result is similar to the result by Gohn et al. [38]. Unlike their study, which requires the destruction of the sensor for collecting the AFM image, here, the two images have been taken from the same sample in the same area, only after different successive thermal treatments performed by FSC in the AFM.

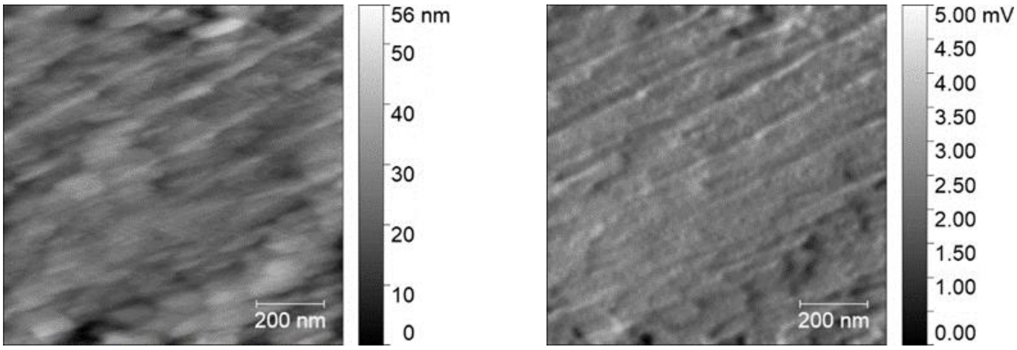

(A) (B)

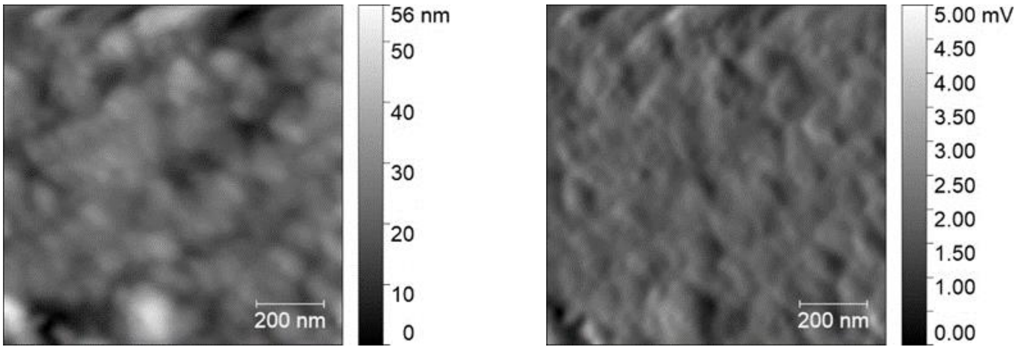

(C) (D)

Figure 29 Topology (left) and amplitude (right) images taken at 278 K after annealing the melt of PA 66 for 1,000 s at 480 K (A and B) and 350 K (C and D).

After taking the images shown in Figure 29, the samples were melted by heating to 580 K at 10,000 K s^{-1}, with the corresponding FSC curves shown in Figure 30. After annealing at 350 K, a double- and after annealing at 480 K a single-melting peak is observed. The double melting peak appearing after annealing at 350 K was not further evaluated, but may be explained as suggested by Furushima et al. by reorganization during heating [107]. From Eqs. 7 and 8, the sample mass was estimated to be ca. 7 ng and the crystallinities achieved at 350 K and 480 K are ca. 62% and 64%, respectively. The values taken from the ATHAS databank were: Δh_∞ = 145 J g^{-1} and Δc_p = 0.4 J g^{-1} K^{-1} [108]. Figure 30 shows the very different melting traces of the two samples, in accordance with the different morphologies in the AFM images of Figure 29.

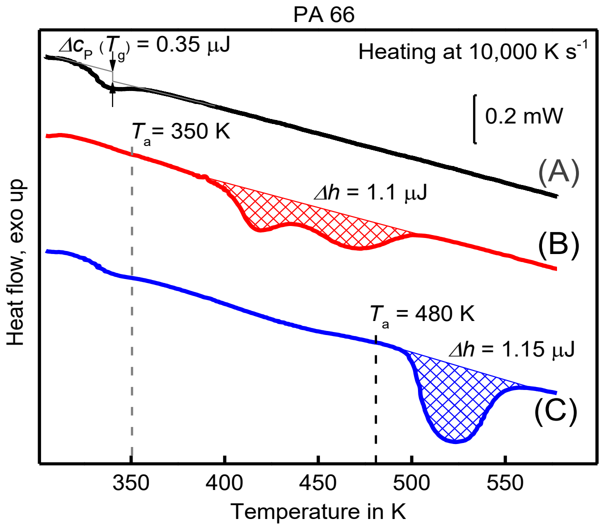

Figure 30 FSC melting curves of PA 66: (A) –quenched sample, (B) – annealed at 350 K for 1,000 s, (C) – annealed at 480 K for 1,000 s.

5 Homogenous nucleation in Polymers

5.1 Homogenous Crystal Nucleation in poly(butylene terephthalate) (PBT)

Prior to Tammann's two-stage crystallization experiment on PBT, the sample was checked for the absence of crystallization at 290 K, which is the nucleation temperature. For that, the AFM images were captured after 1,000 s, 4,000 s, and 5,000 s annealing. The temperature-time profile of the experiment is schematically shown in Figure 31. The heating rate was 10,000 K s^{-1}, which ensure the cold-crystallization to be recorded.

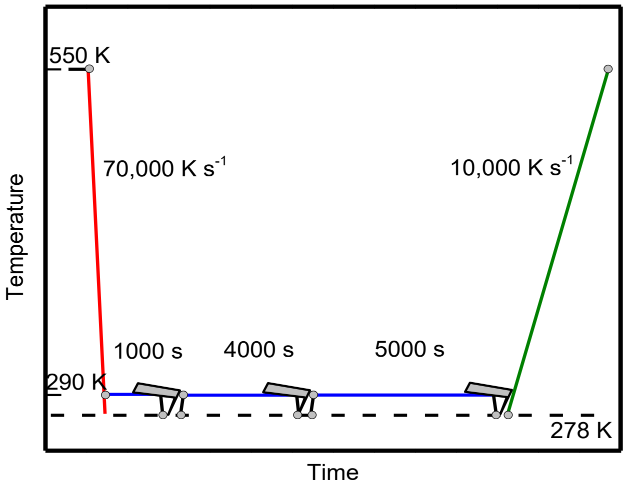

Figure 31 Temperature-time profile of pre-checking the sample of PBT by annealing at 290 K for in total 10,000 s.

Figure 32 shows the heating curves of as-quenched (A) and PBT after annealing at 290 K for 10,000 s (B). Curve (A) shows a glass transition step and no cold crystallization and melting peaks, indicating a “nuclei free” amorphous sample. After 10,000 s annealing, there was a glass transition, cold-crystallization followed by a melting peak. The crystallization and melting peaks have been integrated and their total area was nearly zero, suggesting no previous crystallization but nucleation after 10,000 s resulting in the cold-crystallization peak.

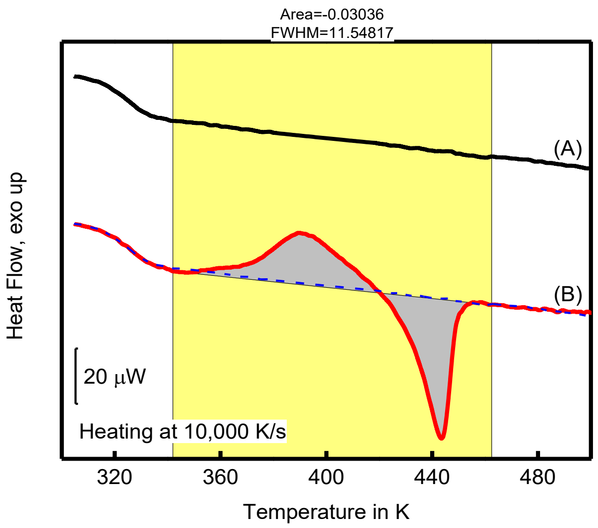

Figure 32 Heating of PBT after cooling at 70,000 K s^{-1} (A) and after annealing at 290 K for 10,000 s (B). The integration as done in OriginLab™ software using a straight line as baseline.

Figure 33 shows AFM images of PBT after quenching and annealing at 290 K for different times. According to all the images collected by AFM, there are not any structures observed, which means that no crystals formed after annealing at 290K for 10,000 s. By comparing with the data in Figure 32, it could be proposed that there was only a nucleation process during annealing at 290 K from 0 to 10,000 s, but still no crystal growth. In order to perform a quantitative study of homogeneous crystal nucleation of PBT, a temperature profile resembling Tammann´s two-stage nucleation and development scheme was applied [109]. Figure 34 (A) shows the temperature-time program realizing Tammann's two-stage nucleation and development scheme in the AFM-FSC device. The other figures for temperature-time profiles for supporting experiments are explained below.

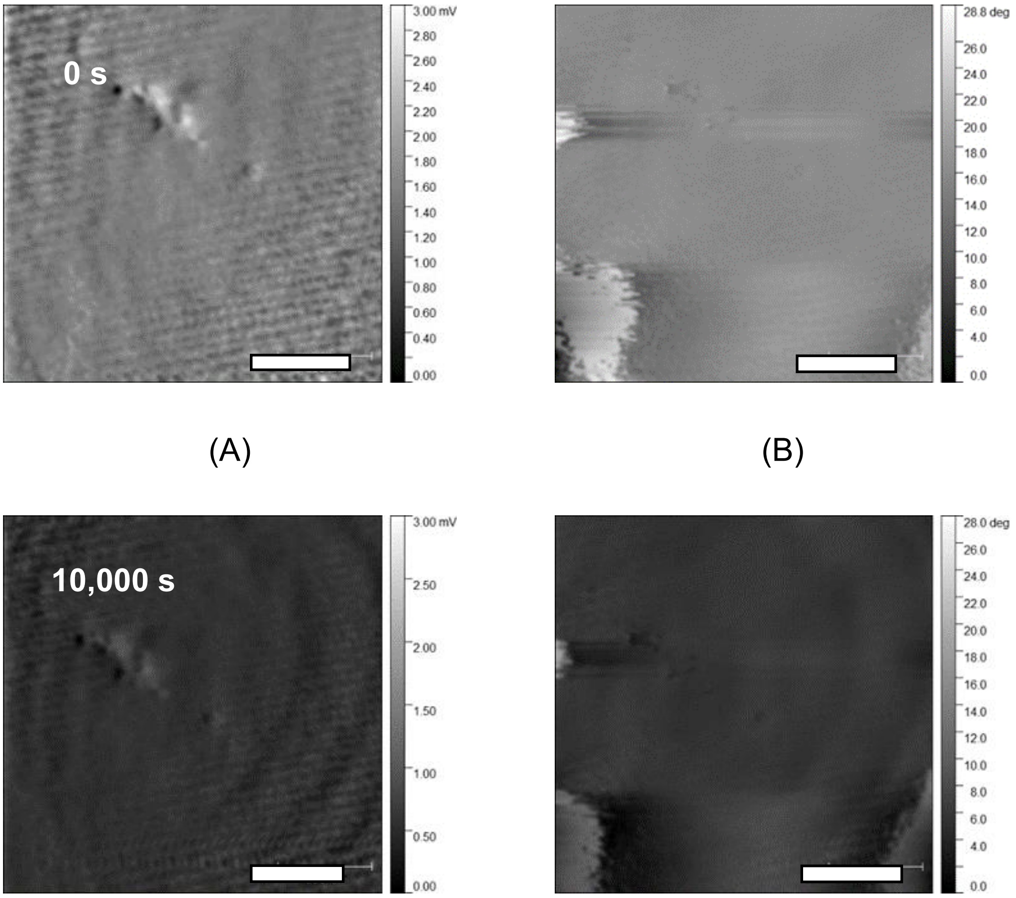

(A) (B)

(C) (D)

Figure 33 AFM amplitude (left) and phase (right) images of PBT before and after annealing at 290 K for 10,000 s. Intermediate images were omitted because no change was seen. (Scale bar represent 500 nm)

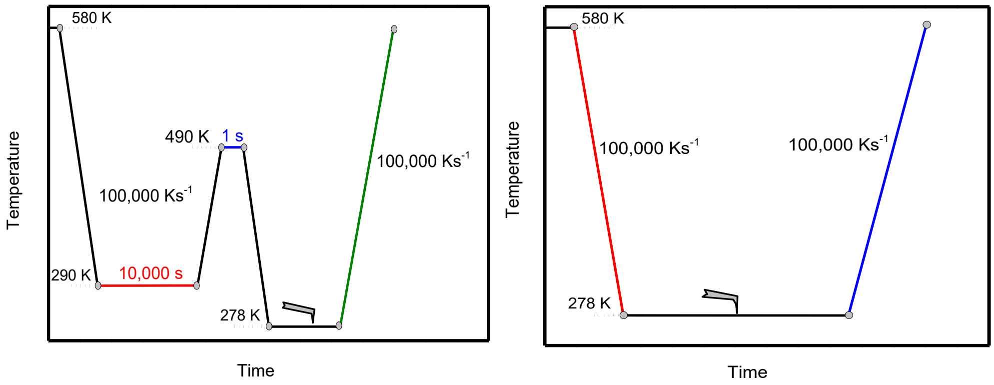

(A) t_{nucl}: 10,000 s, t_{grow}: 1s (B) t_{nucl}: 0, t_{grow}: 0

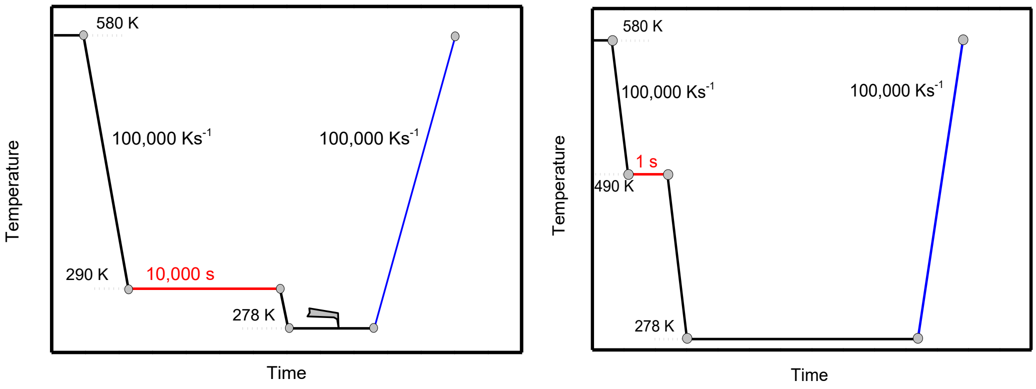

(C) t_{nucl}: 10,000 s, t_{grow}: 0 (D) t_{nucl}: 0, t_{grow}: 1s

Figure 34 Temperature-time profiles for nucleation studies of PBT. For details, see text.

All cooling and heating scans were performed at 100,000 K s^{-1}. (A) – Tammann's two-stage nuclei development method. PBT was first cooled to the nucleation temperature of 290 K, and nucleated for different times. Then the sample was heated to the growth temperature of 490 K and crystal growth from existing nuclei was allowed for 1 s. The corresponding images were taken at ambient temperature. After each nucleation experiment, the sample was heated to 580 K for observation of the crystallinity by the melting enthalpy. (B) - quenching to ambient temperature of 278 K and imaging of the fully amorphous sample; (C) – quenching to the nucleation temperature of 290 K, annealing for 10,000 s and taking an image at 278 K; (D) – melt-crystallization at 490 K for 1 s, followed by imaging at ambient temperature.

At sufficient fast cooling (> 50,000 K s^{-1}, [110]), no crystals and nuclei are observed. To verify the amorphous state of the PBT sample after quenching at 100,000 K s^{-1} to the ambient temperature of 278 K, the scheme of Figure 34 (B) was used. As displayed in Figure 35 (A) and (B), some small particles, probably dust or other solid impurities, in otherwise featureless surroundings appear. These particles provided an easy judgment of the AFM probe-positioning stability regarding the scan area after repeated heating and cooling scans. The heating scan after taking this AFM image is presented as the curve (A) in Figure 36. At a heating rate of 100,000 K s^{-1}, only the glass transition at around 310 K was seen, and neither cold crystallization nor melting peaks were detected. In combination with the information provided in Figure 36 (A), it was confirmed that cooling at 100,000 K s^{-1} produced a “nuclei free” amorphous sample.

Subsequently, the morphology of the PBT sample after nucleation at 290 K for 10,000 s without any growth stage, see the temperature-time profile shown in Figure 34 (C), was investigated. The AFM images were shown in Figure 35 (C and D). Again, only the particles in an unstructured surrounding were seen. The heating scan at 100,000 K s^{-1} was shown as curve (B) in Figure 36. The corresponding heating scan at 10,000 K s^{-1} after annealing at 290 K for 10,000 s showed the glass transition, cold crystallization and subsequent melting of the just crystallized material (Figure 32, curve (B)), which was not seen without annealing at 290 K, (Figure 32, curve (A)), proving the creation of nuclei during the annealing at 290 K for 10,000 s. However, in Figure 36 curve (B), the heating scan at 100,000 K s^{-1} shows no cold-crystallization, suggesting that no growth occurred on heating at 100,000 K s^{-1}. Therefore, the application of Tammann’s two-stage nuclei development method seemed to be justified.

As the last test to evaluate the applicability of Tammann’s two-stage crystallization scheme, the morphology of a melt-crystallized sample, that is, of a sample which was not subject to prior nucleation near T_g, was analyzed, seeing temperature program in Figure 34 (D). Since in bulk polymers of sufficient volume always heterogeneities are present, growth from these heterogeneous nuclei is expected [13]. The AFM images are shown in Figure 35 (E) and (F). Besides the dust particles, some micrometer-sized structures appear. The black square in Figure 35 (F) marks the edges of some of them. From the AFM image one gets the impression that, in particular, surface crystals are formed. This is supported by the heating scan after this treatment, curve (C) in Figure 36. Integration of the peak results in the crystallinity of ca. 7%. At a heating rate of 100,000 K s^{-1}, cold crystallization and recrystallization are prevented [110]. The melting peak after annealing for 1 s at 490 K without previous nucleation is significantly smaller compared to the melting peak after additional nucleation at 290 K for 10,000 s; curve (D) and the dashed line overlaid on the curve (C) in Figure 36. Sample mass was estimated from the measured heat capacity step at the glass transition and known specific heat capacity of the fully amorphous sample from ATHAS databank and equals ca. 0.5 ng. After pre-nucleation (curve (D)), crystallinity was ca. 29%. The crystallinity without pre-nucleation (curve (C)) was ca. 9%. The crystallinity after annealing for 10,000 s at 490 K (curve (E)) was ca. 60%.

Finally, we applied Tammann's two-stage nuclei development scheme to PBT, see Figure 34 (A). The sample was quenched from the melt to the nucleation temperature of 290 K, held there for 10,000 s and then heated to 490 K for 1 s, allowing the formed nuclei to develop to crystals. In Figure 35 (G) and (H), a much finer crystalline morphology appeared, as compared to Figure 35 (E) and (F). The number of objects was significantly increased by the preceding nucleation stage. Crystallization now proceeded not only at the sample surface but seemed to occupy the whole volume, as can be judged by comparing curves (D) and (E) in Figure 36. Curve (E) corresponded to the maximum possible crystallinity for annealing at 490 K. After nucleation for 10,000 s at 390 K and development for 1 s at 490 K about 50% of the maximum possible crystallinity was reached.

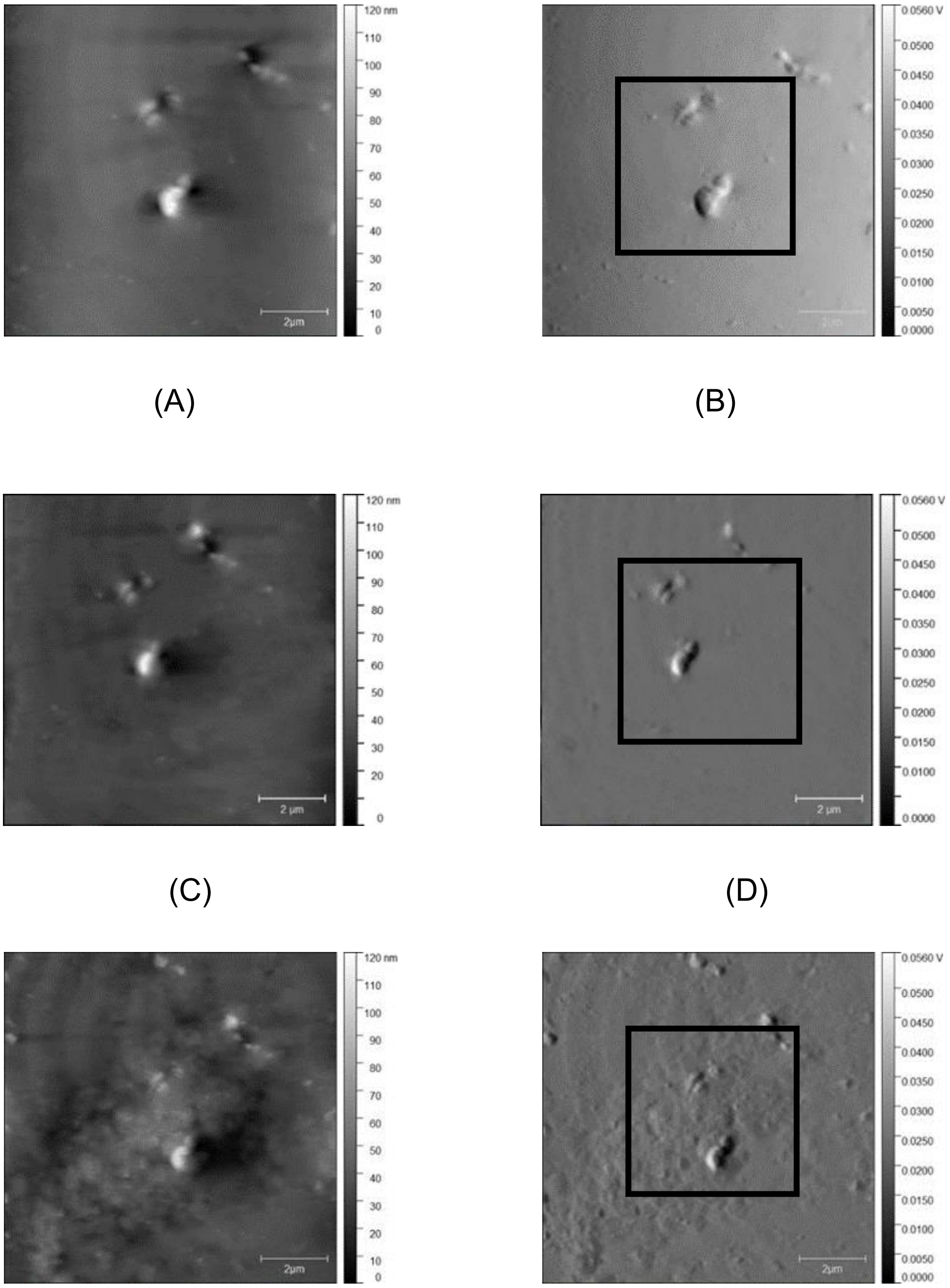

(A) (B)

(C) (D)

(E) (F)

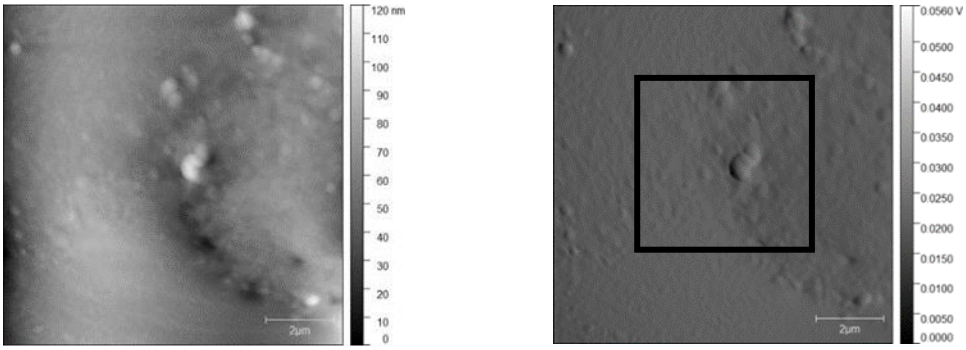

(G) (H)

Figure 35 AFM images of PBT with a 10×10 μm^2 scan area. The sample was quenched (A and B), annealed at 290 K for 10,000 s (C and D), annealed at 490 K for 1 s (E and F) and annealed at 290 K for 10,000 s and at 490 K for 1 s (G and H). The left images (A, C, E, G) show the topology and the right images (B, D, F, H) amplitude differences. Zoomed-in images of the areas marked by the black square are shown in Figure 37.

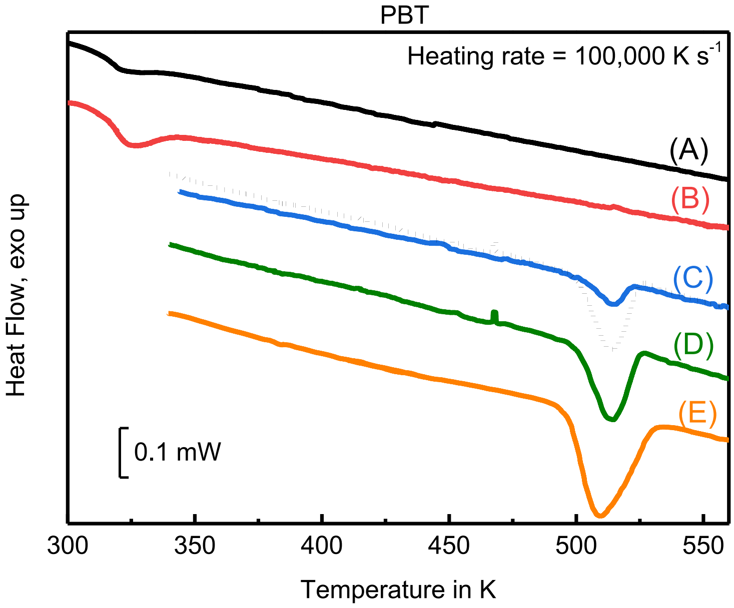

Figure 36 FSC melting curves at heating rate of 100,000 K s^{-1}. (A) –Quenched sample. (B) – Annealing at 290 K for 10,000 s. (C) – Annealing at 490 K for 1 s. (D) – Annealing at 290 K for 10,000 s followed by a development stage at 490 K for 1 s. (E) – Annealing at 490 K for 10,000 s (The dotted curve overlaid on curve (C) is the duplication of curve (D) for comparison)

Figure 37 presents sections of 5 × 5 μm^2 area from the amplitude images of Figure 35. The quenched sample, Figure 37 (A) and (B), did not show any structure except the dust particle (marked by black circle) used as a location marker. In Figure 37 (C), spherulites of about 2 μm diameter could be observed. They are highlighted by the green square. However, with annealing at 290 K for 10,000 s before annealing at 490 K for 1 s, a much finer morphology appeared in Figure 37 (D). At further zooming-in, Figure 37 (F), the size of such granular structures could be estimated being of the order of 100 nm. The number of crystals could be counted as about 40 within a 2 × 2 μm^2 area. Contrary to the essentially homogeneous nodular morphology with sizes of about 10 nm observed after crystallization at 343 K in reference [39], here the structure was much coarser and much more diverse. In Figure 37 (F), particle sizes were between 20 and 200 nm, indicating a non-uniform growth. Estimating the nuclei density by assuming an average distance between nuclei of 100 nm, we end up with about 10^{12} nuclei per mm^3. This is still a high nuclei density, but about 3 orders of magnitude smaller than literature reported [39]. In Figure 37 (E), the PBT was melt-crystallized at 490 K for 2 s, which showed spherulites in a clearer way (marked by green square).

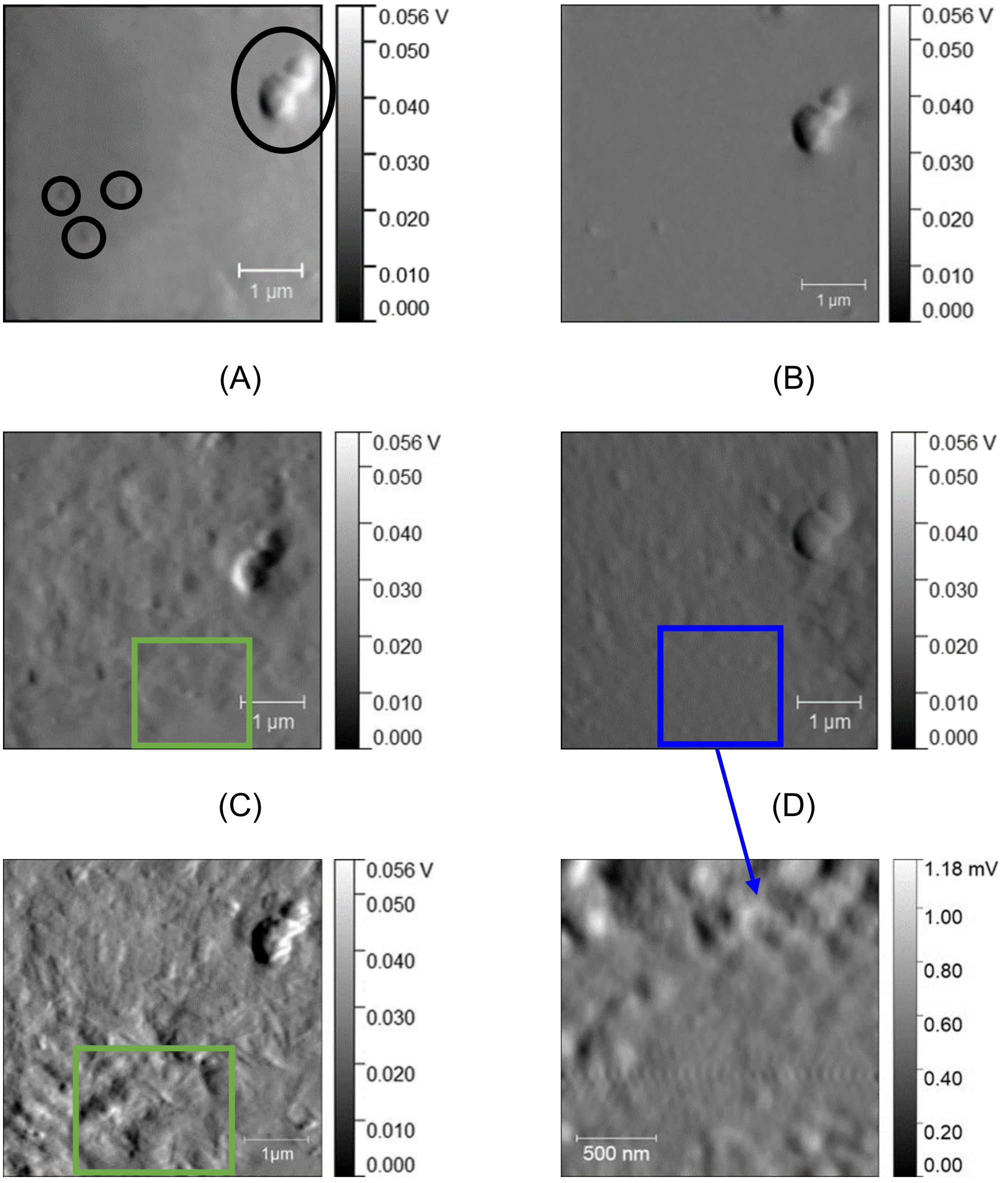

(A) (B)

(C) (D)

(E) (F)

Figure 37 Zoomed-in AFM amplitude images from Figure 35. The images (A), (B), (C) and (D) are zoomed-in images of Figure 35 (B), (D), (F) and (H), respectively. The image (E) is the morphology of PBT melt-crystallized at 490 K for 2 s. The image (F) is a further zoom-in from image d showing a granular morphology with particle sizes of order 100 nm.

Even PBT can be studied by the combined AFM-FSC device employing Tammann's method, there were still two limitations for the PBT sample. The difference between oven temperature and glass transition temperature of PBT is rather small, which makes it difficult to obtain a fully amorphous sample. In addition, the crystallization rate of PBT is fast. This problem can be solved in two ways. First, a more suitable sample, i.e. PA 66, can be used to replace PBT for investigating homogeneous nucleation in polymers. Second, Tammann's two stage crystallization method can be further optimized, in which the growth stage can be replaced by a simple reheating segment.

5.2 Steady-state homogeneous crystal nucleation rate of PA 66

Compared with PBT, PA 66 has a slower crystallization rate with a minimum half-time of crystallization longer than 10^{-3} s and a lower critical cooling rate to suppress crystallization of 500–1000 K s^{-1}. The T_g is rather high (323 K), which enables using the FSC without employing very low sub-ambient temperatures [38, 111]. Analysis of the crystallization rate revealed a bimodal nucleation-controlled temperature-dependence with homogeneous crystal nucleation dominating at temperatures lower than about 400 K [38]. Crystallization at higher temperature proceeds via heterogeneous nucleation and growth of lamellae and spherulites, while crystallization via homogeneous nucleation at lower temperatures yields the formation of small nodular domains. For these reasons, PA 66 is considered a good candidate for applying Tammann's method and to study homogeneous nucleation by the AFM-FSC combination.

5.2.1 FSC analysis of nucleation and crystallization of PA 66 at 310 K

The nucleation and crystallization kinetics of PA 66 are studied by FSC employing the temperature-time profile illustrated in Figure 38 (A). The sample was heated to 580 K, that is, to above the $T_{m,0}$ of 574 K, to obtain a relaxed melt. Then the polymer was rapidly cooled to 310 K, that is, to slightly below T_g, using a rate of 100,000 K s^{-1}. Such a high cooling rate is sufficiently fast to suppress both crystallization and formation of nuclei on cooling. Subsequently to the cooling step, the obtained glass was subjected to isothermal annealing for different times between 0.1 and 100,000 s, allowing nucleation and crystallization (red segment). After cooling the sample to 278 K, an analysis-heating scan, representing the growth- or nuclei-development-stage in Tammann's method, is performed (green segment). Note that the selected heating rate of 10,000 K s^{-1} permits cold-crystallization but only in the presence of nuclei formed during annealing, thus allowing following the progress of nucleation by the enthalpy of cold-crystallization.

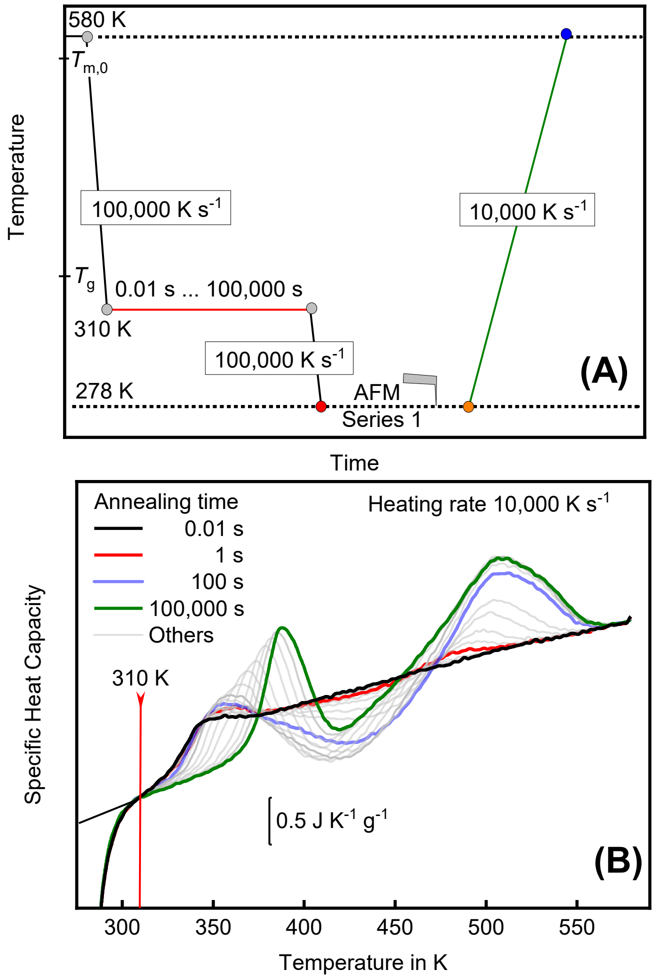

Figure 38 **(A)** Temperature-time profile for studying isothermal nucleation and crystallization of PA 66 at 310 K. The glass transition temperature (T_g) of 323 K and equilibrium melting temperature ($T_{m,0}$) of 574 K are indicated at the temperature axis. **(B)** FSC heating scans of PA 66 after isothermal annealing at 310 K for different times between 0.01 s and 100,000 s, as indicated in the legend. The heating rate is 10,000 K s^{-1}, and the red vertical line indicates the temperature of prior annealing.

Figure 38 (B) shows analysis-heating scans in specific-heat-capacity units, with the plot including ATHAS databank heat-capacity data of liquid and solid

PA 66 (black lines), and information about the annealing temperature (red vertical line). Few curves are highlighted by black, red, blue, and green coloring, representing different stages of nucleation and crystal growth at the annealing temperature. Short-term annealing for only 0.1 s (black curve) does not allow both nucleation and crystallization, and, as such, only the heat-capacity increment at T_g is detected. If the sample is annealed for 1 s (red curve), in addition to the glass transition, exothermic cold-crystallization due to nuclei formation is detected between 400 and 450 K, followed by a small melting peak close to 500 K. The areas of the crystallization and melting peaks are identical, which proves absent crystallization at the annealing temperature of 310 K. Qualitatively similar behavior is seen in annealing experiments lasting up to 400 s (blue curve), however, with the increasing areas of the cold-crystallization- and melting-peaks indicating an increasing number of nuclei. Annealing longer than 400 s, finally, permits crystallization at the annealing temperature recognized by an increase of the glass transition temperature, which in addition is superimposed by a melting peak, by minor cold-crystallization, and final melting (see the green curve in Figure 38 (B)).

Quantitative data about the nucleation and crystallization kinetics are obtained by analysis of the annealing-time dependence of the Δh_{cc} and Δh_{total}, respectively, as shown in Figure 39 (A) and (B). The total enthalpy-change was obtained by integrating the curves between the annealing temperature (310 K) and $T_{m,0}$ (574 K), down to zero, and subtracting the same integral of the non-annealed sample. The cold-crystallization enthalpy was estimated by integrating the corresponding exothermic cold-crystallization peaks using the heat capacity of liquid PA 66 as a baseline. The data reveal that cold-crystallization due to nuclei formation is observed if the annealing time exceeds about 1 s, while annealing for 100 s, or longer, causes crystallization, as indicated with the upturn of the total enthalpy-change. The change of slope of the total enthalpy-change after about 3000 s is associated with a transition from primary to secondary crystallization. A series of AFM images were collected as indicated in Figure 38 (A) to show the morphology after annealing at 310 K, named ‘Series 1’ and shown in Figure 43.

The half-times of nucleation and crystallization are obtained by a double Avrami fit of the two data sets [70, 112], with the fitting functions represented by Eqs. (9) and (10), respectively:

$$\Delta \mathrm{h}_{cc} = -(\Delta \mathrm{h}_{nucl'}\left(1 - \exp\,(-\frac{t}{t_{half,nucl}} ln2)^{n}\right) + \Delta \mathrm{h}_{het}) + \Delta \mathrm{h}_{total} \tag{9}$$

$$\Delta \mathrm{h}_{total} = \Delta \mathrm{h}_{crys'}\left(1 - \exp\,(-\frac{t}{t_{half,crys}} ln2)^{n}\right) + \mathrm{A}_2\left(ln\left(t - t_{half,crys}\right)\right) * \left(\frac{1}{2}\frac{\left|t - t_{half,crys}\right|}{t - t_{half,crys}} + 1\right) \tag{10}$$

In Eqs. (9) and (10), $\Delta h_{\mathrm{nucl'}}$ is the maximum cold-crystallization enthalpy due to formation of homogeneous nuclei in Figure 39 (A), $\Delta h_{\mathrm{crys'}}$ is the final enthalpy of primary crystallization in Figure 39 (B), *t* is the annealing time, *n* is the Avrami index, A_2 is a constant related to secondary crystallization and $t_{\mathrm{half,nucl}}$ and $t_{\mathrm{half,crys}}$ are the half-times of nucleation and primary crystallization, respectively. Cold-crystallization due to the presence of heterogeneous nuclei (Δh_{het}) is absent under the chosen experimental conditions, yielding $\Delta h_{\mathrm{het}} = 0$. Eq.(9) simplifies accordingly. The presence of heterogeneous nuclei would cause cold-crystallization also at short annealing times, which, however, is not observed at the heating rate of 10,000 K. The fit of the data shown in Figure 39 yields half-times of homogeneous crystal nucleation and primary crystallization of about 24 and 670 s, respectively. Finally, the half-times were determined for annealing temperatures between 310 K and 420 K and are shown in below.

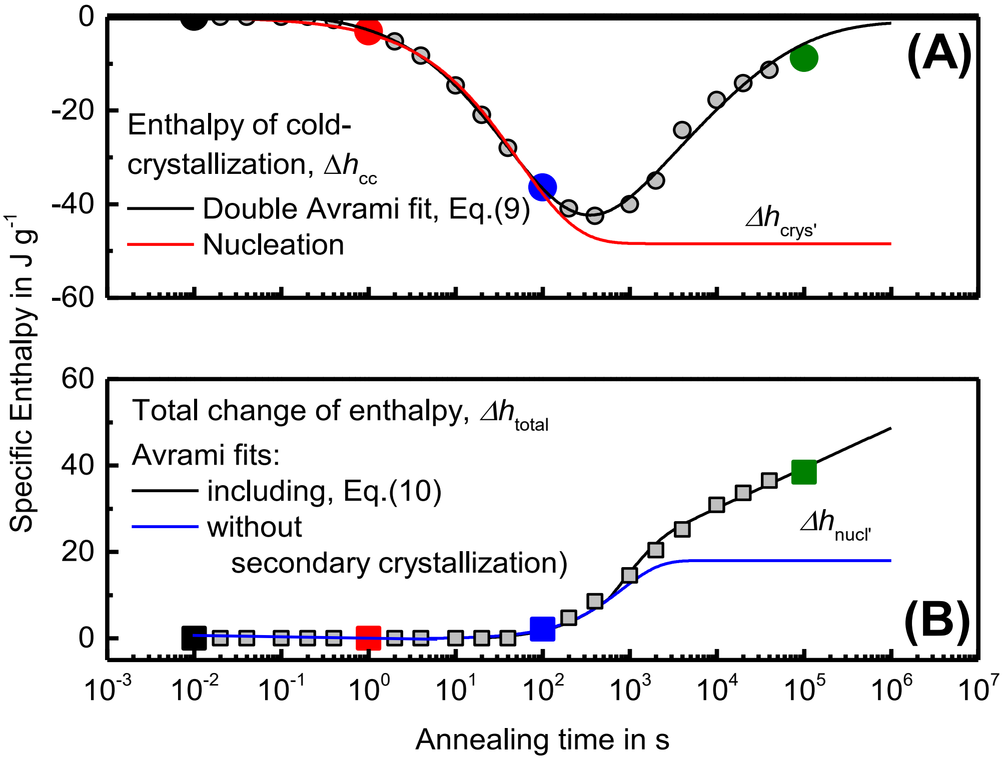

Figure 39 **(A)** Cold-crystallization enthalpy and **(B)** total enthalpy change of PA 66 on heating, both as function of annealing time at 310 K. The highlighted data points Figure 39 correspond to the highlighted curves in Figure 38 (B).

5.2.2 AFM-FSC analysis of the enthalpy of formation of one PA 66 crystal at pre-defined growth conditions

In order to trace nucleation by AFM, Tammann's method has been applied. The temperature-time program of the experiment shows Figure 40 (A). After removal of the thermal history by heating to 580 K for 10 ms, the sample is cooled to 310 K at a rate of 100,000 K s^{-1}, followed by isothermal annealing at this temperature for the annealing time between 0.01 and 100,000 s, in analogy to the annealing experiment described above. Additionally, after the annealing step, the sample is heated to 460 K at 10,000 K s^{-1}, isothermally held at this temperature for 1 ms, and cooled down to 278 K at 10,000 K s^{-1}, allowing the growth of nuclei to detectable crystals mainly at heating (blue segment). Note that the temperature of 460 K was selected such to allow cold-crystallization but to avoid melting. The isothermal segment of 1 ms at 460 K was included in the temperature profile for instrumental reasons, required for turning the heating ramp into a cooling ramp. After cooling the sample to 278 K, a second set of AFM images was collected, named ‘Series 2’, to illustrate the morphology formed in the development stage of Tammann’s method, that is, formed mainly during heating, but also during annealing at 460 K, and during re-cooling to 278 K. Finally, a further analysis-heating scan is performed, in order to evaluate the achieved crystallinity (green segment).

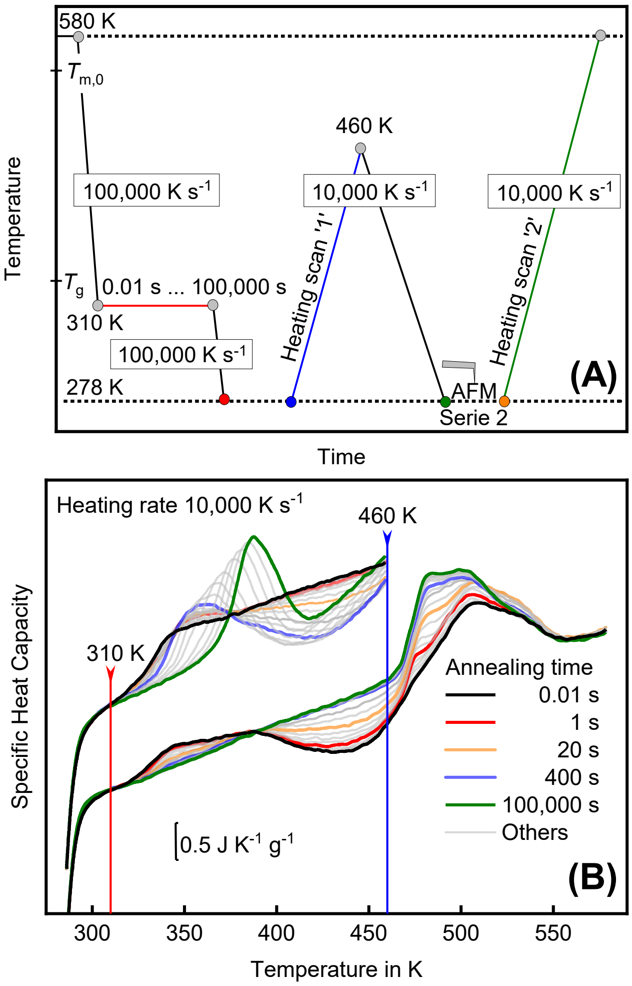

Figure 40 **(A)** Temperature-time profile for studying crystal nucleation in PA 66 employing Tammann's method. The isothermal red segment represents the nucleation stage while the blue heating ramp, the isotherm, and the re-cooling represent the growth stage, allowing growth of nuclei to crystals. **(B)** FSC heating scans '1' to a maximum temperature of 460 K (top set of curves), allowing growth of nuclei but avoiding melting, and final FSC heating scans '2' for evaluation of the crystallinity as a function of the annealing time (bottom set of curves).

Figure 40 (B) shows with the top and bottom sets of curves heating scans '1' and ‘2’ (see blue and green segments in Figure 40 (A)), respectively. The top data set verifies the reproducibility of the nucleation and growth experiment described in Figure 39. For annealing times longer than about 1 s, cold-crystallization is detected and a semicrystalline structure is expected at the end of the growth stage. Inspection of the final analysis heating scans (bottom set of curves), however, reveals information that nuclei formation, when initially annealing between 0.01 and 20 s, continues e.g. during cooling from 460 K to 278 K or during collection of the AFM ‘Series 2’, as distinct cold-crystallization is detected in the heating scan 2 for these short annealing times. For example, after 0.01 s annealing (black curve in Figure 40) no cold-crystallization appears in heating scan 1 but significant cold crystallization is seen in heating scan 2. Nevertheless, the total enthalpy change determined from heating scan 2 is still zero, indicating that without nuclei formed during annealing, there are no detectable crystals formed on heating to 460 K, annealing and cooling back to 278 K.

The highlighted curves in Figure 40 (B) are shown in Figure 41 (A) and (B) together with the baselines used for integration. The resulting enthalpies of cold crystallization during heating scan ‘1’ (Δh_{cc}) and the total enthalpy change from heating scan ‘2’ (Δh_{total}) are shown in Figure 42.

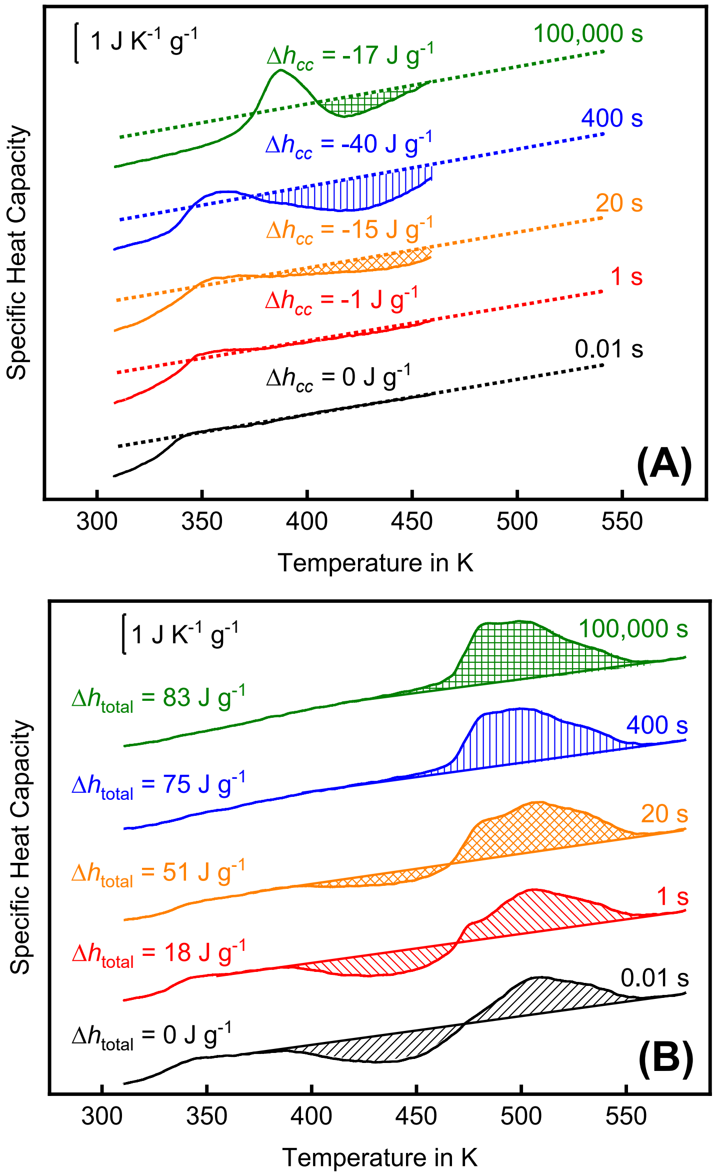

Figure 41 **(A)** Selected heating scans '1' with the baseline used for integrating the cold-crystallization peak (Δh_{cc}). **(B)** Selected heating scans '2' with the baseline used for integrating cold-crystallization and melting peaks (Δh_{total}).

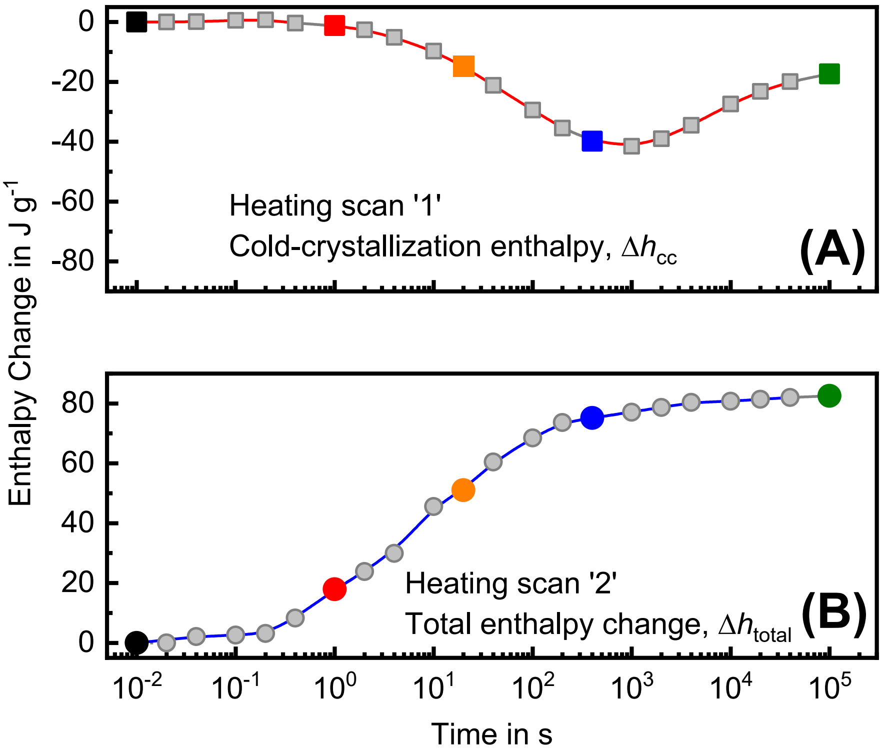

Figure 42 **(A)** Cold-crystallization enthalpy in heating scan ‘1’ and **(B)** total enthalpy change in heating scan ‘2’. Both as a function of annealing time at 310 K. The highlighted data points in Figure 5 correspond to the highlighted curves in Figure 3 (B) and Figure 4.

The FSC heating scans ‘1’ were evaluated regarding the enthalpy of cold-crystallization, providing information about the fraction of crystals formed at the heating scan 1 and with that information about the nuclei formed during annealing similar to Figure 42 (A). Integration of the heating scans ‘2’, covering the cold-crystallization peak and the melting peak, in contrast, reveals information about the total enthalpy change, that is, about the fraction of crystals formed in the preceded development-stage.

In the hypothetical case that all crystallization occurs at heating and nothing at the isotherm and on cooling, one expects similar absolute values of opposite sign in Figure 42 (A) and (B). However, comparing cold crystallization enthalpy from heating scan 1, Figure 42 (A), with the total enthalpy change from heating scan 2, Figure 42 (B), results in a significant difference. The change of total enthalpy from heating scan 2 is about twice the cold crystallization enthalpy from heating scan 1.

From the observation above regarding the short annealing times and this discrepancy, we conclude that (i) no crystals form during the development stage without nuclei created before the development stage and (ii) crystals growing from nuclei created during the nucleation stage are able to grow on heating (Δh_{cc}) and additionally at the isotherm and on cooling. However, from (i) we can assume that the number of crystals in the AFM images of Series 2, after the development stage, corresponds to the number of overcritical nuclei present after the nucleation stage. With this assumption, the cold crystallization enthalpy from heating scan '1' (Δh_{cc}) allows estimating the number of nuclei present after the nucleation stage as explained below.

Figure 43 shows AFM images of the morphology of a PA 66 sample collected immediately after cooling the melt at 100,000 K s^{-1} to 278 K (top left) and after additional isothermal annealing at 310 K for different time up to 100,000 s, as indicated; note that all micrographs were taken at 278 K. The phase-angle color scale is adjusted such that amorphous regions are shown in blue while crystals appear in green and red. Most important, the morphology detected by AFM excellently agrees with the calorimetrical data of Figure 40 (A). The FSC data revealed that crystallization begins after about 100 s, which is in accord with the first appearance of heterogeneities/crystals in the corresponding AFM image of Figure 43. Annealing for longer time causes a further increase of the crystal number and their growth, and after 100,000 s, a space-filled semi-crystalline morphology is achieved.

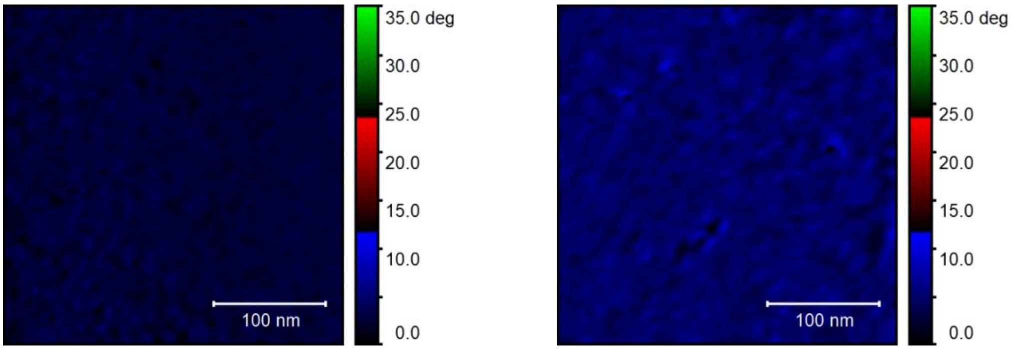

Quench

10 s

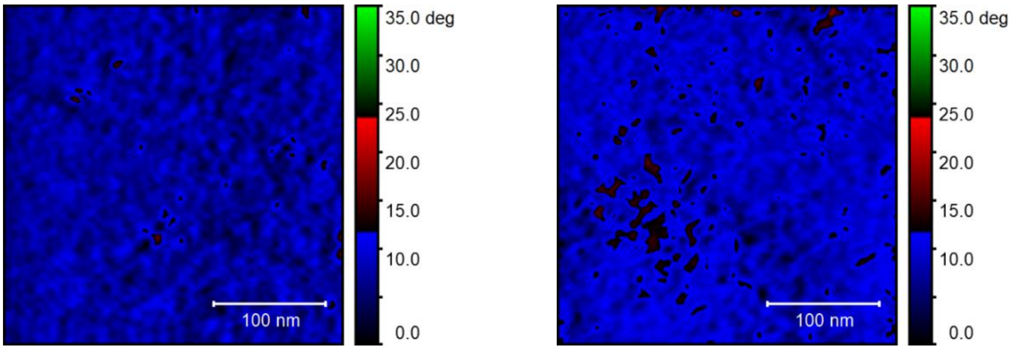

100 s

1,000 s

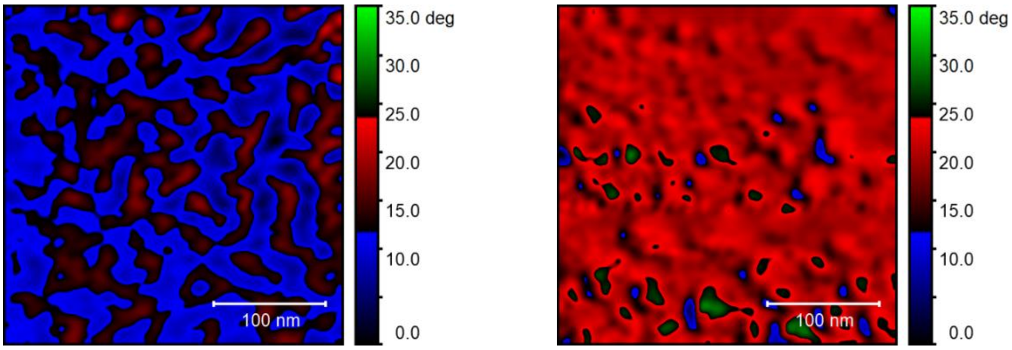

10,000 s

100,000 s

Figure 43 AFM phase images of PA 66 collected after cooling the melt at 100,000 K s^{-1} to 278 K (top left), and after additional annealing at 310 K for 10, 100, 1000, 10,000, and 100,000 s as indicated. These images correspond to AFM 'Series 1' in Figure 40 (A). The scale bar corresponds to 100 nm.

Figure 44 shows AFM images of PA 66 of Series ‘2’, collected after subjecting the polymer to Tammann’s method. The images (A) to (N) represent different annealing/nucleation times, while the growth conditions were kept unchanged (see red and green segments in Figure 40 (A)). Quenching the melt to 310 K and annealing up to 0.4 s does not cause nucleation and therefore cold-crystallization is absent on heating to 460 K. Therefore, the images (A) to (C) are featureless. Starting from image (D), bright spots with an increasing number appear, interpreted as visible crystals with a size of around 100 nm, grown from previously formed nuclei. Note, at this point in research estimation and interpretation of the absolute size of crystals is out of the scope since the employed AFM is optimized for FSC coupling but not for observation of high-resolution images. However, AFM can detect these crystals allowing estimation of the nuclei density through counting the number. With increasing annealing time, more and more crystals are observed. When the annealing time at 310 K exceeds 1000 s (image (M)), then the contrast between amorphous and crystalline phases disappears, and is completely lost at an annealing time of 2000 s (image (N)). Referring to the bottom right image in Figure 43, we suggest impingement of crystals and achievement of a space-filled semi crystalline morphology.

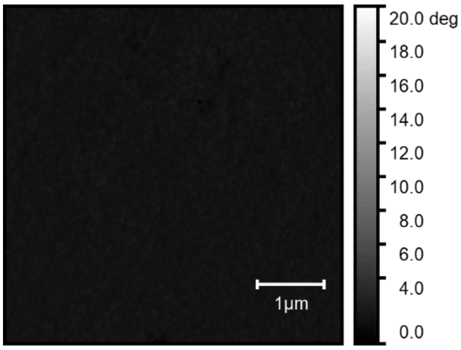

(A) Quenched

$\mathit{Num}_{\text{cryst}}$: 0, $N_{\text{v}}(t)$: 0

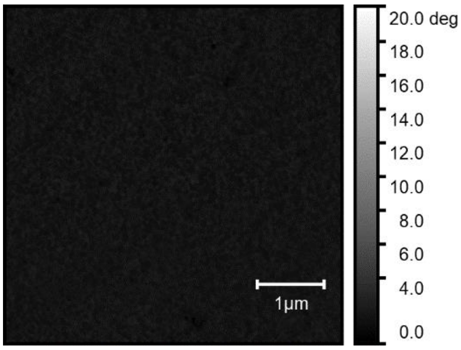

(B) 0.01 s

$\mathit{Num}_{\text{cryst}}$: 0, $N_{\text{v}}(t)$: 0

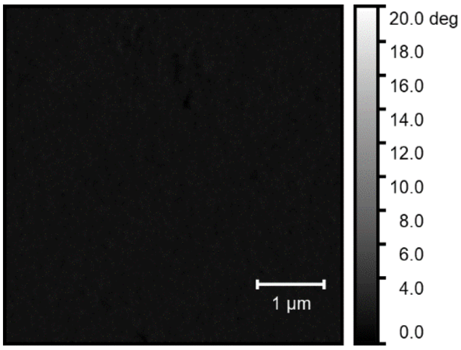

(C) 0.4 s

$\mathit{Num}_{\text{cryst}}$: 0, $N_{\text{v}}(t)$: 0

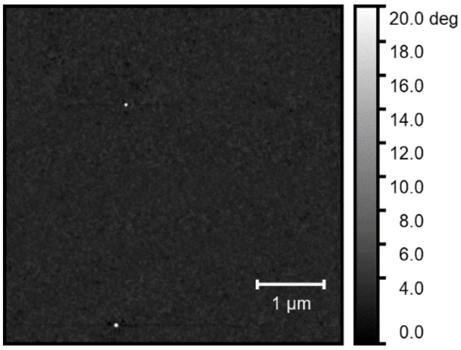

(D) 1 s

$\mathit{Num}_{\text{cryst}}$: 2, $N_{\text{v}}(t)$: 8.00×10^{17} m^{-3}

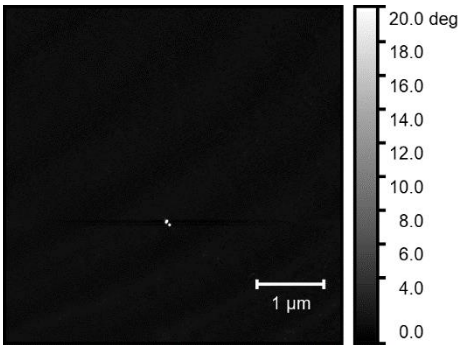

(E) 2 s

$\mathit{Num}_{\text{cryst}}$: 3, $N_{\text{v}}(t)$: 1.2×10^{18} m^{-3}

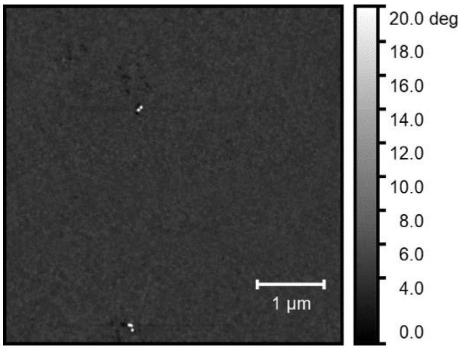

(F) 4 s

$\mathit{Num}_{\text{cryst}}$: 5, $N_{\text{v}}(t)$: 2×10^{18} m^{-3}

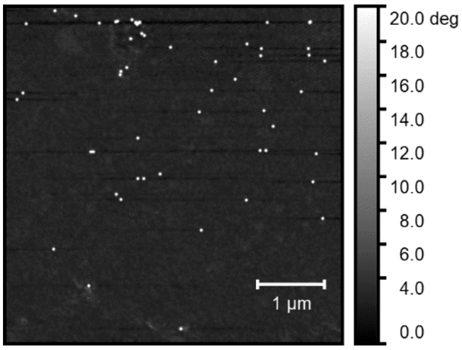

(G) 10 s

Num$_{\text{cryst}}$: 55, $N_v(t)$: 2.2×10^{19} m^{-3}

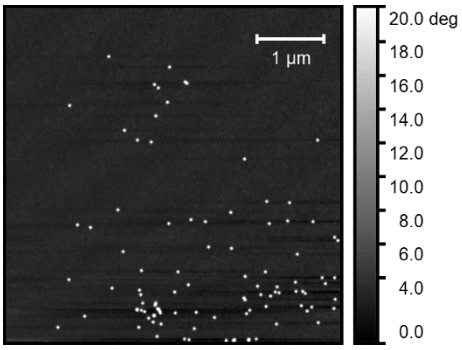

(H) 20 s

Num$_{\text{cryst}}$: 94, $N_v(t)$: 3.8×10^{19} m^{-3}

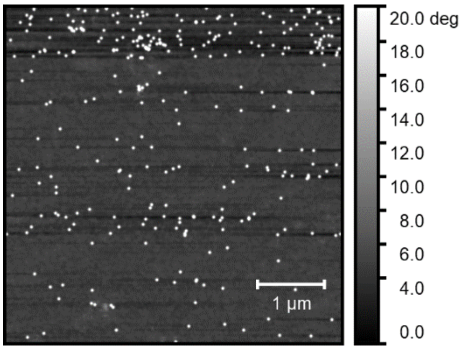

(I) 40 s

Num$_{\text{cryst}}$: 259, $N_v(t)$: 1×10^{20} m^{-3}

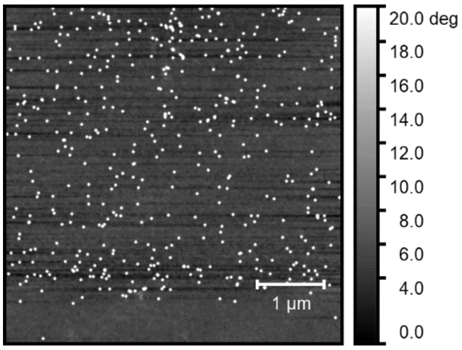

(J) 100 s

Num$_{\text{cryst}}$: 421, $N_v(t)$: 1.7×10^{20} m^{-3}

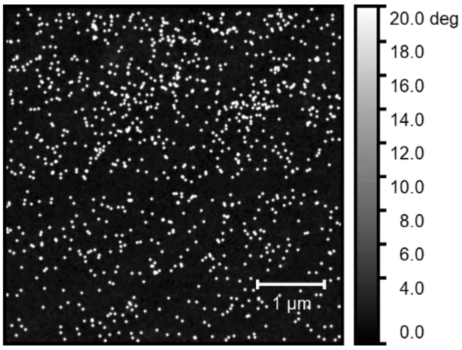

(K) 200 s

Num$_{\text{cryst}}$: 795, $N_v(t)$: 3.2×10^{20} m^{-3}

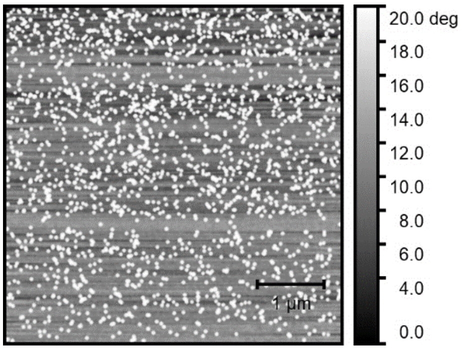

(L) 400 s

Num$_{\text{cryst}}$: 1220, $N_v(t)$: 4.9×10^{20} m^{-}

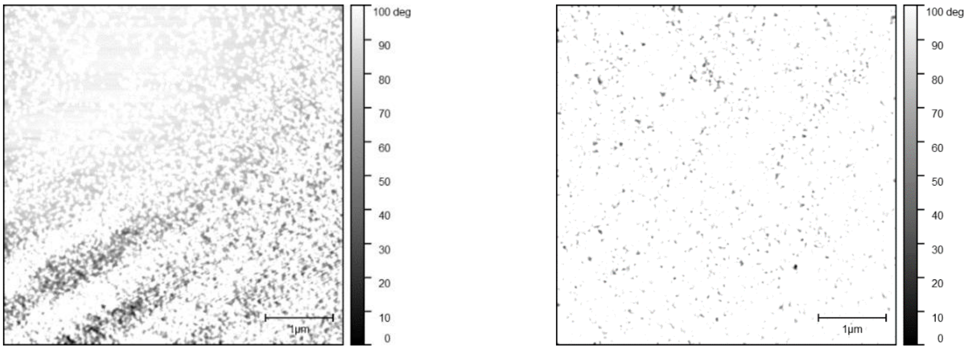

(M) 1000 s (N) 2000 s

The scales for phase angle between the cantilever oscillation and the driving force in (M) and (N) are different from all other images (100 deg instead of 20 deg).

Figure 44 AFM phase images of PA 66 collected after annealing at 310 K according to Tammann's method. Referring to Figure 40 (A), the images correspond to AFM 'Series 2'. The annealing time is indicated at the various images. The scale bar corresponds to 1 µm. The reproducibility of images is documented in the Appendix A1. Number of crystals observed in the images: (Num_{cryst}). $N_{\mathrm{v}}(t)$ is the volume density of crystals determined from Num_{cryst} as described in the text.

The number of nuclei and the resulting area density, estimated from the AFM images using ImageJ software is given below each image. Nuclei area density was transformed to volume density by assuming the same nuclei density in each slice of 100 nm thickness. Such assumption is common for determining particle volume densities from area densities [113]. The uncertainty caused by this assumption for the determined crystal number density, $N_{\mathrm{v}}(t)$, is not analyzed, and errors given below represent statistical uncertainties only. The resulting volume densities shows Figure 45 (A) as a function of the annealing time (see Appendix A2 for further details). For annealing times shorter than 50 s, a linear relation between the nuclei number and the annealing time is obvious, representing steady-state nucleation. For annealing times longer than 100 s, saturation occurred, related to the high number of nuclei formed, and space constraints. Regarding the initial, linear part of the curve, an attempt to rationalize the obtained data within the frame of the CNT is possible.

As described by CNT [45, 46, 114-116], the relationship between the $N_V(t)$ at a particular annealing time t and the I_{st} is given by Eq.(11):

$$N_V(t) = I_{st}\tau\left[t - \frac{\pi^2}{6}\tau - 2\tau\sum_{m=1}^{\infty}\frac{(-1)^m}{m^2}\exp\left(-m^2\frac{t}{\tau}\right)\right] \tag{11}$$

In Eq.(11), m is an integer between unity and infinity and τ is the time lag of forming clusters (nuclei) of critical size. This expression can be simplified to Eq.(12) for times, t, much longer than τ:

$$N_V(t) = I_{st}\left(t - \frac{\pi^2}{6}\tau\right) \tag{12}$$

In the experimental data of Figure 45 (A), τ cannot directly be estimated while the so-called induction time t_{ind} can be assessed through linear fitting, being the onset time in the experimental curve of the nuclei density versus the annealing time. The relationship between t_{ind} and τ shows Eq.(13):

$$\tau = t_{ind}\frac{6}{\pi^2} \tag{13}$$

Combining Eqs.(11) to (13), I_{st} can be estimated at ($t - t_{ind}$) > 0 by Eq.(14):

$$I_{st} = \frac{N_V(t)}{t - t_{ind}} \tag{14}$$

By fitting the data of Figure 45 (A), through Eq.(14), I_{st} and t_{ind} can be obtained as $(2.3 \pm 0.2)\times10^{18}\ m^{-3}\ s^{-1}$ and 3 s, respectively.

Assuming, as discussed above, that all overcritical nuclei formed at the nucleation stage grow to observable crystals at heating to 460 K and continue to grow at the isotherm and at cooling, we can estimate the contribution of each single crystallite to the observed Δh_{cc} from heating scan 1. If each nucleus in average contributes the same amount to the measured cold-crystallization enthalpy of heating scan 1, Eq.(15) below provides the relation between the volume based cold-crystallization enthalpy $\Delta h'_{cc}$ and the number density of nuclei from the AFM images. Eq.(15) allows conversion of measured transition enthalpies in units of J g^{-1} (Δh) into units of J m^{-3} ($\Delta h'$), employing the density of the sample ($\rho_{sample} \approx 1.1$ g cm^{-3}) [117]:

$$\Delta h' = \Delta h \cdot \rho_{\mathrm{sample}} \tag{15}$$

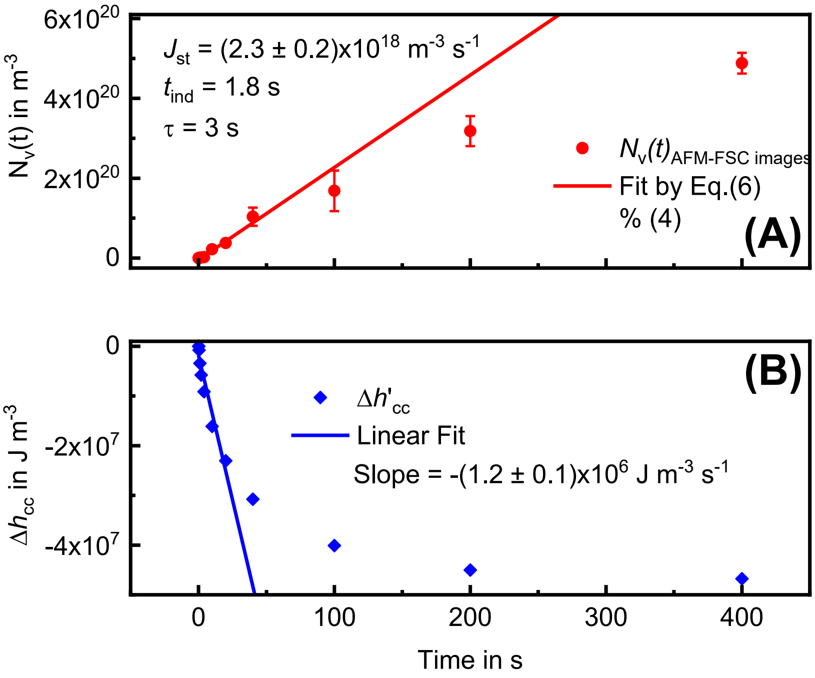

Figure 45 Number-density of crystals developed by nucleation at 310 K and growth during heating to 460 K, isothermal annealing at 460 K for 1 ms, and subsequent re-cooling **(A)**, and corresponding enthalpy of crystallization **(B)**, both as a function of the annealing time.

Figure 45 shows for the annealing time interval between 0 and 400 s on a linear time scale the dependencies of the nuclei density $N_v(t)$, Figure 45 (A), and of the cold-crystallization enthalpy $\Delta h'_{cc}$, Figure 45 (B). In the time interval where the number of nuclei identified in the AFM images depends essentially linearly on time, below 50 s, also a linear dependence of Δh_{cc} on time is expected, which, however, is not strictly observed. Nevertheless, for annealing times below 50 s, the curve is close to linear and the enthalpy contribution of each single crystallite ($\Delta h'_{cc,single}$) to the measured cold-crystallization enthalpy ($\Delta h'_{cc}$) at heating rate 10,000 K s^{-1} can be determined via Eq.(16) as $\Delta h'_{cc,single} = (5.2 \pm 0.5)\times10^{-13}$ J:

$$\Delta h'_{cc,single} = \left(\frac{d\Delta h'_{cc}/dt}{I_{st}}\right)_{at\ linearity} \tag{16}$$

With this quantity, the dependence of the number of supercritical nuclei on time, $N_v(t)$, can be estimated from $\Delta h'_{cc}(t)$, which enables estimation of nucleation rates for a wide temperature range since only calorimetric data are required.

5.2.3 FSC analysis of the temperature-dependence of nucleation rates of PA 66

Figure 46 shows the temperature-time program for studying isothermal nucleation and crystallization rates at different annealing temperatures between 310 and 420 K. Samples are cooled at a rate of 100,000 K s^{-1} to a pre-defined temperature, followed by annealing for different time up to 100,000 s. The nucleation and crystallization kinetics are then obtained, again, through the reheating curves, shown in the Appendix A3.

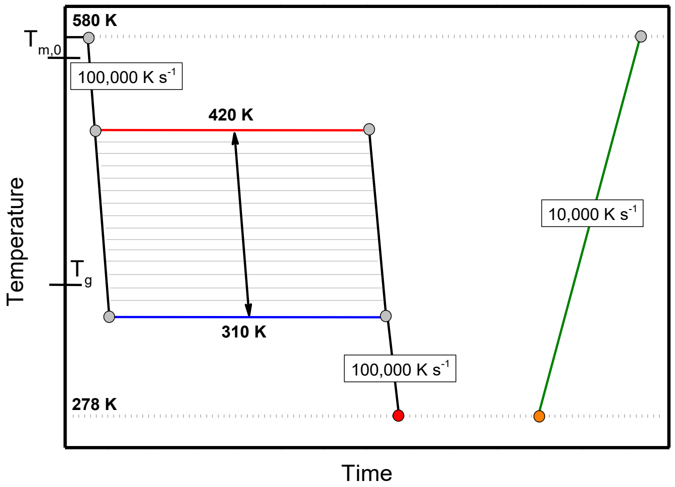

Figure 46 Temperature-time profile for studying rates of homogeneous nucleation at different temperatures between 310 and 420 K. The glass transition temperature (T_g) of 323 K and equilibrium melting temperature ($T_{m,0}$) of 574 K are indicated at the temperature axis.

Figure 47 (A) shows the total change of enthalpy and Figure 47 (B) the cold-crystallization enthalpy of PA 66 as a function of the time of annealing at the indicated temperatures, derived from the analysis-heating scans shown in Appendix A3 Figure A5 and A4, respectively (see also green-colored segment in Figure 46). In Figure 47, as the annealing temperature increases from 310 K to 420 K, the rates of crystallization and nucleation increase. Similar as for the data of Figure 40, double Avrami fitting (see Eqs.(9) and (10)) allowed estimation of half-times of nucleation and crystallization, $t_{\mathrm{half,nucl}}$ and $t_{\mathrm{half,crys}}$, respectively, for the various annealing temperatures, as shown in Figure 48. Both, $t_{\mathrm{half,nucl}}$ and $t_{\mathrm{half,crys}}$ show a similar dependence on the annealing temperature. When annealing at temperatures higher than 375 K, then cold-crystallization cannot be observed and $t_{\mathrm{half,nucl}}$ cannot be quantified, suggesting that heterogeneous nucleation becomes dominant. In addition, Figure 48 also shows the τ-values obtained through Eq.(13), revealing a distinct minimum at 345 K. Comparing the data of the present work with earlier published crystallization-rate data obtained on the same material [38] reveals excellent agreement. However, while crystallization based on homogeneous nuclei is fastest at about 380 K, the maximum nucleation rate is detected at 350–360 K; similarly, τ shows a minimum at around 345 K.

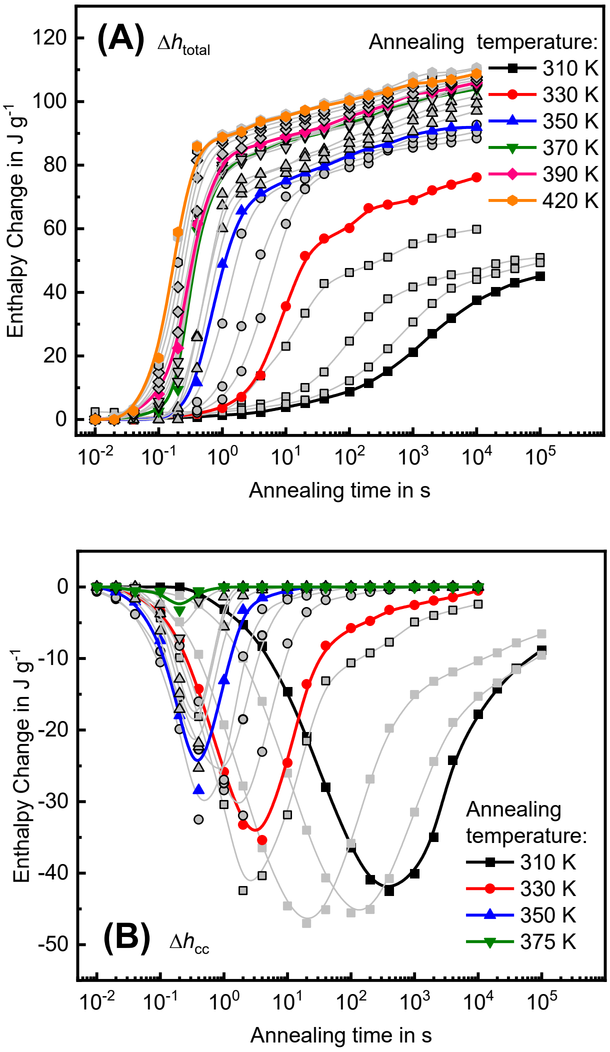

Figure 47 **(A)** Total enthalpy change and **(B)** cold-crystallization enthalpy of PA 66 as a function of the time of annealing at the indicated temperatures. The temperature increment for the grey colored curves equals 5 K.

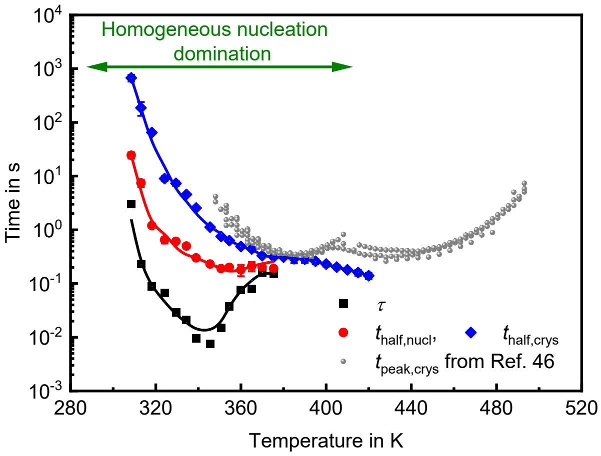

Figure 48 Time lag of forming nuclei of critical size, half-time of isothermal nucleation, half-time of isothermal crystallization and peak-time of isothermal crystallization as a function of temperature. Additional crystallization peak-time data are obtained from the literature.[38]

By using the above described isothermal FSC experiments at different annealing temperatures, the $N_v(t, T)$ can be quantitatively estimated by Eq.(17):

$$N_v(\mathrm{t},\mathrm{T}) = \frac{\Delta h'_{cc}(t,T)}{\Delta h'_{cc,single}} \tag{17}$$

$\Delta h'_{cc}(t, T)$ is the enthalpy of cold-crystallization during heating to 460 K after annealing at different temperatures for different times. In the case of identical growth conditions, it is expected that the size of all crystals forming from the nuclei is independent of the initial size and structure of the nuclei, that is, independent on the nucleation time and temperature. As a representative example, Figure 49 (A) shows the enthalpy of cold-crystallization Δh_{cc} as a function of the annealing time at 345 K. The number of nuclei $N_v(t)$ is estimated through Eq.(17) for the linear part of the curve, and the steady-state nucleation rate I_{st} is calculated through Eq.(14). The nuclei number $N_v(t)$ is plotted as a function of the annealing time in Figure 49 (B) while results obtained from data sets involving nucleation at different temperatures are available in the Appendix

A5.

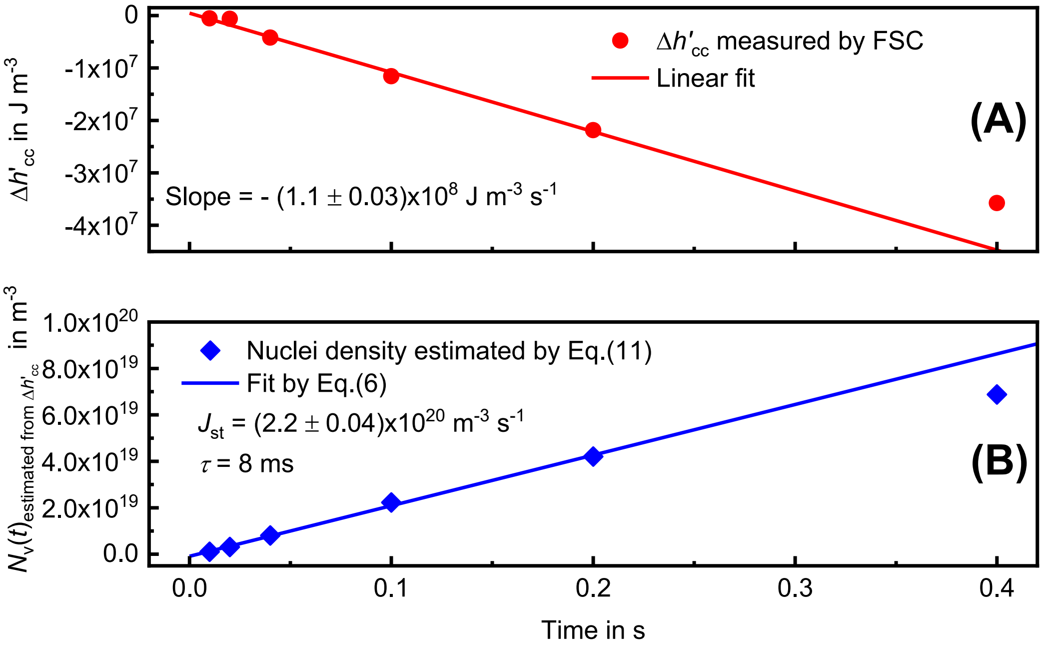

Figure 49 **(A)** Experimentally observed enthalpies of cold-crystallization and **(B)** estimated nuclei number $N_v(t)$ as a function of the time of annealing at 345 K. The linear fits exclude the point at 0.4 s.

Figure 50 shows I_{st} as a function of temperature within the analyzed temperature range between 310 and 375 K. Within this temperature interval, the nucleation rate varies by, roughly, two orders of magnitude between 10^{17} and 10^{19} m^{-3} s^{-1}. The maximum nucleation rate is observed at 345 K. According to the CNT, the dependence of I_{st} on temperature is described by Eq.(18):

$$I_{st} = c\sqrt{\frac{\sigma}{k_B T}}\left(\frac{D}{d_0}\right)\exp\left(-\frac{W_c}{K_B T}\right) \tag{18}$$

Furthermore, $d_0 \approx 3.34$ nm is the length of a monomer in the unit cell, the shape parameter c is estimated as $1/d_0^3$ and W_c is the work of formation of a nucleus of critical size. The diffusion coefficient is estimated by Eq.(19), assuming that the system behaves like a liquid:

$$D = D_0 \exp\left(-\frac{E_D}{k_B T}\right) \tag{19}$$

where D_0 = 3.3×10^{-4} m^2 s^{-1} is the maximum value of D and W_c can be estimated through Eq.(20) [118]:

$$W_c = k_B T_{m,0} \frac{\omega}{\left(1-\frac{T}{T_{m,0}}\right)^2}; \qquad \omega = \frac{16\pi\alpha^3\varphi}{3}\left(\frac{\Delta H_m}{k_B T_{m,0}}\right) \tag{20}$$

In Eq.(20), $T_{m,0}$ = 574 K [108], φ is equal to 1 for homogeneous nucleation [118], and α is assumed as 0.45 [119]. As shown in Figure 50 with the red line, the CNT can describe the experimental results at high temperatures well, but largely overestimates the results at low temperatures. For inorganic materials and metals, this phenomenon has been widely reported. A sound explanation is that the effective diffusion coefficient D near the glass transition temperature (T_g) is not properly described by Eq.(19) as diffusion would stop only when the temperature is 0 K, far from reality. Experimental results show that nucleation and growth both fade at temperatures lower than 30…50 K below T_g [6, 67, 120].

Abyzov et al. [119] proposed to take into account the spatial heterogeneity of the liquid when the temperature is near and below T_g. In liquid-like regions, nucleation proceeds via the CNT while in solid-like regions, nucleation is suppressed. In order to fit the experimental data, $P(T)$ is introduced in the CNT. Thus, CNT$_{\text{low-temp}}$ is expressed by Eq.(21):

$$I_{\mathrm{st}} = P(T)\cdot \mathrm{c}\sqrt{\frac{\sigma}{k_B T}}\left(\frac{D}{d_0}\right)\exp\left(-\frac{W_c}{K_B T}\right) \tag{21}$$

They suggested estimating $P(T)$ through an empirical Eq.(22):

$$P(T) = \frac{V_n}{V} = \begin{cases} 1\ (T > T_{sw}) \\ \exp\left[-K_v (T_{sw} - T)^{\beta}\right]\ (T < T_{sw}) \end{cases} \tag{22}$$

Eq.(21) is able to resolve the problems in the application of CNT for many materials, including PA 66 of the present study (see blue line in Figure 50).

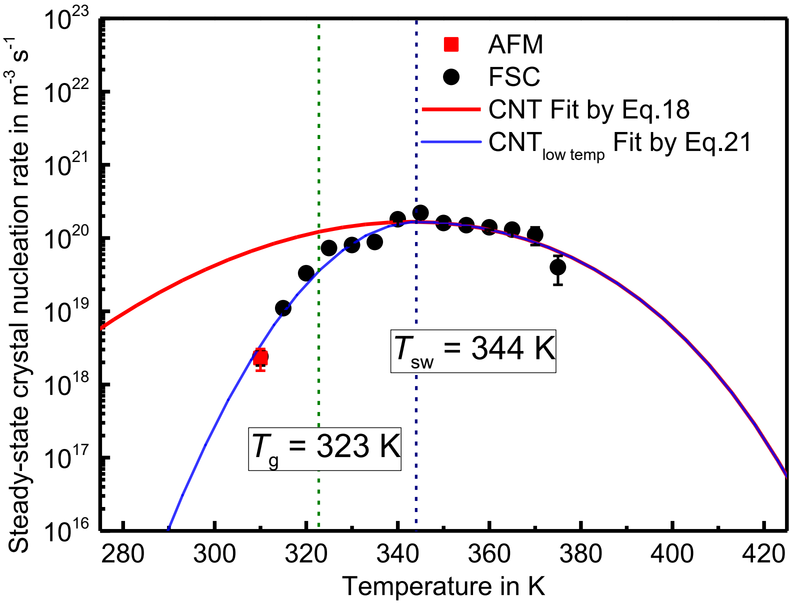

Figure 50 Steady-state crystal nucleation rate of PA 66 as a function of temperature estimated by calorimetry (black points). The data are fitted by Eqs.(18) and (21), as shown by the red and blue lines, respectively. The parameters, obtained by nonlinear least square fitting, are as follows: $E_D = 7.6\times10^5$ J mol^{-1}, $\Delta\sigma = 0.036$ J m^{-2}, T_{sw} = 344 K, $K_v = 0.0025$ and $\beta = 2$.

With an optimized Tammann's two-stage crystallization method, the dependence of nucleation density on annealing time for PA 66 at 310 K has been successfully investigated by AFM-FSC. Moreover, using the enthalpy contribution of each individual crystallite, the FSC data can be utilized to estimate the density of nuclei from the reheating scan segments after isothermal annealing. Thus, the nucleation kinetics of PA 66 at temperatures between 310 and 375 K was investigated through FSC. The temperature dependence of the steady-state nucleation rate of PA 66 and other polymers can be estimated by this approach.

6 Conclusion

The AFM-FSC combined device provides an efficient tool for the detailed studies of morphology developments after annealing for very different times (ms to days) and cooling and heating in a very wide range of scanning rates (up to 1,000,000 K s^{-1}). The performance of the AFM-FSC device was tested by investigating different morphological features for different kinds of polymers. Crystallization pathways were widely varied to allow, for example, heterogeneous and homogeneous crystal nucleation. Such studies are not limited to polymers but any other crystallizing system, giving some contrast in AFM. The FSC does not only provide a very fast hot stage for the AFM; it also allows studying the thermal behavior of the sample just after taking the AFM image. Furthermore, the micrometer-sized hot-spot of the FSC chip and total heating powers of the order of less than 10 mW do not disturb the AFM extensively. Thermal treatments can be repeated either applying the same thermal treatment for improving the statistical relevance of the results or with changing parameters to obtain some dependencies. In both cases, the high reproducibility of the image location is very beneficial.

The *in situ* AFM-FSC provides quantitative information on homogeneous crystal nucleation in PA 66. PA 66 was subjected to Tammann's two-stage crystal nuclei development method, including quenching the relaxed melt to the nuclei-formation temperature of 310 K, annealing for different times to allow crystal nucleation, supplemented by an analysis of nuclei-growth to crystals by heating the sample. The employed specific experimental setup allows a precise correlation of AFM images and FSC heating curves. The number of detectable crystals/nuclei from the AFM images is of the order of 10^{10} to 10^{13} m^{-2}. By variation of the nucleation time and converting the area densities to volume densities, a value of the steady-state nucleation rate equal to (2.3±0.2)×10^{18} m^{-3} s^{-1} at 310 K has been evaluated. Comparing the total enthalpy of cold crystallization in the development stage of Tammann's method, obtained by FSC, with the number of crystals, observed by AFM, yields the specific enthalpy of melting/formation of one individual crystal of (5.2±0.5)×10^{-13} J. This value holds for the specific growth conditions applied, here heating at 10,000 K s^{-1} to 460 K. With the (5.2±0.5)×10^{-13} J and the measured cold crystallization enthalpy in the development stage, after nucleation at different temperatures for different times, provides an reliable estimate for the nuclei densities. Application of this approach, that is, correlating transition enthalpies with nuclei numbers, for analysis of crystal nucleation in a wide range of temperatures between 310 and 375 K yielded a maximum homogeneous nucleation rate close to 1019 m^{-3} s^{-1} at around 350 K. The present study offers a qualitatively new approach of analyzing the kinetics of homogeneous nucleation of polymers. In addition, it allows one to employ the specific AFM-FSC setup as a valuable tool for direct observation of crystal-specific enthalpies of crystallization.

7 References

1. Tang, X., W. Chen, and L. Li, *The Tough Journey of Polymer Crystallization: Battling with Chain Flexibility and Connectivity.* Macromolecules, 2019.
2. Hu, W.B., *Growth rate equations of lamellar polymer crystals.* Polymer Crystallization, 2018. **Early View**: p. e25831.
3. Strobl, G., *Colloquium: Laws controlling crystallization and melting in bulk polymers.* Reviews of Modern Physics, 2009. **81**(3): p. 1287-1300.
4. Strobl, G., *Crystallization and melting of bulk polymers: New observations, conclusions and a thermodynamic scheme.* Progress in Polymer Science, 2006. **31**(4): p. 398-442.
5. Geil, P.H., *Folded Molecules in Lamellas Crystallized from Molten Polymers.* Journal of Applied Physics, 1962. **33**(2): p. 642-643.
6. Wunderlich, B., *Macromolecular physics*. Vol. 2. 2012: Elsevier.
7. Wunderlich, B., *Thermal analysis of polymeric materials*. 2005: Springer Science & Business Media.

8. Hobbs, S., *Polymer Microscopy.* Journal of Macromolecular Science—Reviews in Macromolecular Chemistry, 1980. **19**(2): p. 221-265.
9. Lotz, B., J. Wittmann, and A. Lovinger, *Structure and morphology of poly (propylenes): a molecular analysis.* Polymer, 1996. **37**(22): p. 4979-4992.
10. Guo, Q., *Polymer morphology: principles, characterization, and processing*. 2016: John Wiley & Sons.
11. Saalwächter, K., *Applications of NMR in Polymer Characterization–An Introduction.* 2019.
12. Sawyer, L.C., D.T. Grubb, and G.F. Meyers, *Polymer Microscopy*. 2008, New York, NY: Springer New York. 1-540.
13. Schick, C., R. Androsch, and J.W.P. Schmelzer, *Homogeneous crystal nucleation in polymers (topical review).* J Phys Condens Matter, 2017. **29**: p. 453002.
14. Androsch, R. and C. Schick, *Crystal nucleation of polymers at high supercooling of the melt*, in *Polymer Crystallization I*, F. Auriemma, G.C. Alfonso, and C.d. Rosa, Editors. 2015, Springer International Publishing: Switzerland. p. 257-288.
15. Schick, C. and V. Mathot, *Fast Scanning Calorimetry.* Springer International Publishing AG Switzerland, 2016: p. 1-795.
16. Androsch, R., M.L.D. Lorenzo, and C. Schick, *Optical microscopy to study crystal nucleation in polymers using a fast scanning chip calorimeter for precise control of the nucleation pathway.* Macromol Chem Phys, 2018. **219**(3): p. 1700479 (1-10).
17. Williams, D.B. and C.B. Carter, *The Transmission Electron Microscope: A Textbook for Materials Science*. 2009, Boston, MA: Springer US. 1-760.
18. Tencé-Girault, S., et al., *About the Art and Science of Visualizing Polymer Morphology using Transmission Electron Microscopy.* 2018. **219**(3): p. 1700483.
19. Kim, S., et al., *Minimization of focused ion beam damage in nanostructured polymer thin films.* Ultramicroscopy, 2011. **111**(3): p. 191-9.
20. Zhao, B., et al., *Formation of amorphous structure in Sn3.5Ag droplet by in situ fast scanning calorimetry controllable quenching.* Applied Physics Letters, 2013. **103**(13).
21. Zhao, B., et al., *Structure observation of single solidified droplet by in situ controllable quenching based on nanocalorimetry.* Journal of Alloys and Compounds, 2013. **580**: p. 386-391.
22. Egerton, R.F., P. Li, and M. Malac, *Radiation damage in the TEM and SEM.* Micron, 2004. **35**(6): p. 399-409.
23. Grapes, M.D., et al., *Combining nanocalorimetry and dynamic transmission electron microscopy for in situ characterization of materials processes under rapid heating and cooling.* Review of Scientific Instruments, 2014. **85**(8): p. -.
24. Yi, F., et al., *A multi-environment nanocalorimeter with electrical contacts for use in a scanning electron microscope.* Materials Horizons, 2017. **4**(6): p. 1128-1134.
25. Savage, R.C., N. Mullin, and J.K. Hobbs, *Molecular Conformation at the Crystal–Amorphous Interface in Polyethylene.* Macromolecules, 2015. **48**(17): p. 6160-6165.
26. Morita, S., et al., *Noncontact atomic force microscopy*. Vol. 3. 2015: Springer.
27. Hobbs, J.K., *In-situ AFM of polymer crystallization.* Chinese journal of polymer science,

2003. **21**(2): p. 135-140.

28. Hobbs, J.K., O.E. Farrance, and L. Kailas, *How atomic force microscopy has contributed to our understanding of polymer crystallization.* Polymer, 2009. **50**(18): p. 4281-4292.
29. Zhou, J.-J., et al., *Atomic force microscopy study of the lamellar growth of isotactic polypropylene.* Polymer, 2005. **46**(12): p. 4077-4087.
30. Hobbs, J.K., et al., *Direct observations of the growth of spherulites of poly(hydroxybutyrate-co-valerate) using atomic force microscopy.* Polymer, 1998. **39**(12): p. 2437-2446.
31. Li, L., et al., *Direct Observation of Growth of Lamellae and Spherulites of a Semicrystalline Polymer by AFM.* Macromolecules, 2001. **34**: p. 316-325.
32. Chen, E.-Q., et al., *In situ observation of low molecular weight poly(ethylene oxide) crystal melting, recrystallization.* Polymer, 2003. **44**(19): p. 6051-6058.
33. Mileva, D., et al., *Morphology of mesophase and crystals of polyamide 6 prepared in a fast scanning chip calorimeter.* Polymer, 2012. **53**(18): p. 3994-4001.
34. Ding, Q., et al., *Morphology of α-crystals of poly (butylene 2, 6-naphthalate) crystallized via a liquid crystalline mesophase according to Ostwald's rule of stages.* Polymer, 2020: p. 122404.
35. Jin, L., et al., *Crystallization behavior and morphological characterization of poly(ether ether ketone).* Polymer, 2014. **55**(20): p. 5255-5265.
36. Salmerón Sánchez, M., et al., *Effect of the cooling rate on the nucleation kinetics of poly (L-lactic acid) and its influence on morphology.* Macromolecules, 2007. **40**(22): p. 7989-7997.
37. Schick, C. and V. Mathot, *Fast Scanning Calorimetry*. 2016: Springer.
38. Gohn, A.M., et al., *The effect of supercooling of the melt on the semicrystalline morphology of PA 66.* Thermochimica Acta, 2017. **655**: p. 313-318.
39. Androsch, R., et al., *Density of heterogeneous and homogeneous crystal nuclei in poly (butylene terephthalate).* European Polymer Journal, 2015. **66**: p. 180-189.
40. Mollova, A., et al., *Effect of Supercooling on Crystallization of Polyamide 11.* Macromolecules, 2013. **46**(3): p. 828-835.
41. Van den Brande, N., G. Van Assche, and B. Van Mele, *Isothermal Crystallization of PC61BM in Thin Layers Far below the Glass Transition Temperature.* Crystal Growth & Design, 2015. **15**(11): p. 5614-5623.
42. Cormia, R.L., F.P. Price, and D. Turnbull, *Kinetics of Crystal Nucleation in Polyethylene.* The Journal of Chemical Physics, 1962. **37**(6): p. 1333-1340.
43. Chatterjee, A.M., F.P. Price, and S. Newman, *Heterogeneous nucleation of crystallization of high polymers from the melt. III. Nucleation kinetics and interfacial energies.* Journal of Polymer Science: Polymer Physics Edition, 1975. **13**(12): p. 2391-2400.
44. Fokin, V.M., et al., *Crystal nucleation in glass-forming liquids: Variation of the size of the “structural units” with temperature.* Journal of Non-Crystalline Solids, 2016. **447**: p. 35-44.

45. Gibbs, J., *The Collected Papers, Vol. 1, Thermodynamics*. 1928, Longmans, Green and Co., New York.

46. Fokin, V.M., et al., *Homogeneous crystal nucleation in silicate glasses: A 40 years perspective.* Journal of Non-Crystalline Solids, 2006. **352**(26-27): p. 2681-2714.

47. Abyzov, A.S., V.M. Fokin, and E.D. Zanotto, *Predicting homogeneous nucleation rates in silicate glass-formers.* Journal of Non-Crystalline Solids, 2018. **500**: p. 231-234.

48. Zanotto, E.D., J.W.P. Schmelzer, and V.M. Fokin, *Nucleation, Growth, and Overall Crystallization in Inorganic Glasses*.

49. Keith, H.D. and J. F. J. Paddek, *The Optical Behavior of Spherulites in Crystalline Polymers. Part 11. The Growth and Structure of the Spherulites.* Journal of Polymer Science, 1959. **135**(39): p. 123-138.

50. Androsch, R. and C. Schick, *Crystal Nucleation of Polymers at High Supercooling of the Melt.* Advances in Polymer Science, 2015: p. 1-32.

51. Schick, C. and R. Androsch, *Nucleation‐controlled semicrystalline morphology of bulk polymers.* Polymer Crystallization, 2018. **1**(4): p. e10036.

52. Mileva, D., et al., *Homogeneous nucleation and mesophase formation in glassy isotactic polypropylene.* Polymer, 2012. **53**(2): p. 277-282.

53. Gezovich, D.M. and P.H. GEIL, *Morphology of Quenched Polypropylene.* Polymer engineering and science, 1968. **8**(3): p. 202-209.

54. Wang, Z.-G., et al., *Phase transformation in quenched mesomorphic isotactic polypropylene.* Polymer, 2001. **42**: p. 7561-7566.

55. Zia, Q., et al., *Crystal morphology of rapidly cooled isotactic polypropylene: A comparative study by TEM and AFM.* Polymer Bulletin, 2008. **60**(6): p. 791-798.

56. Ivanov, D.A., B. Nysten, and A.M. Jonas, *Atomic force microscopy imaging of single polymer spherulites during crystallization: application to a semi-crystalline blend.* Polymer, 1999. **40**: p. 5899–5905.

57. Majumder, S., et al., *Growth Kinetics of Stacks of Lamellar Polymer Crystals.* Macromolecules, 2018. **51**(21): p. 8738-8745.

58. Frank, F.C., *Influence of Dislocations on crystal growth.* Discussions of the Faraday Society 1949. **5**: p. 48-54.

59. Burton, W.K., N. Cabrera, and F.C. Frank, *Role of Dislocations in Crystal Growth.* Nature, 1949. **163**(4): p. 398-399.

60. Barnes, W.J. and F.P. Price, *Morphology of Polymer Crystals: Screw Dislocations in Polyethylene, Polymethylene Oxide and Polyethylene Oxide.* Polymer, 1964. **5**: p. 283–292.

61. Keith, H.D. and W.Y. Chen, *On the origins of giant screw dislocations in polymer lamellae.* Polymer 2002. **43**: p. 6263–6272.

62. Oguni, M. and C.A. Angell, *Hydrophobic and hydrophilic solute effects on the homogeneous nucleation temperature of ice from aqueous solutions.* The Journal of Physical Chemistry, 1983. **87**(11): p. 1848-1851.

63. MacFarlane, D.R., R.K. Kadiyala, and C.A. Angell, *Homogeneous nucleation and growth of ice from solutions. TTT curves, the nucleation rate, and the stable glass*

criterion. The Journal of Chemical Physics, 1983. **79**(8): p. 3921-3927.

64. Senapati, H., K.K. Kadiyala, and A. C.A., *One-and two-step calorimetric studies of crystallization kinetics in simple ionic glass-forming liquids. 1. Calcium nitrate-potassium nitrate system.* The Journal of Physical Chemistry, 1991. **95**(18): p. 7050-7054.
65. Minakov, A.A. and C. Schick, *Ultrafast thermal processing and nanocalorimetry at heating and cooling rates up to 1 MK/s.* Rev Sci Instrum, 2007. **78**(7): p. 073902.
66. Zhuravlev, E., et al., *Kinetics of nucleation and crystallization in poly(epsilon caprolactone) (PCL).* Polymer, 2011. **52**(9): p. 1983-1997.
67. Schick, C., R. Androsch, and J.W.P. Schmelzer, *Homogeneous crystal nucleation in polymers.* Journal of Physics Condens Matter, 2017. **29**(45): p. 453002.
68. Androsch, R., C. Schick, and M.L. Di Lorenzo, *Kinetics of Nucleation and Growth of Crystals of Poly(l-lactic acid).* Advances in Polymer Science, 2017. **279**: p. 235-272.
69. *Poly(epsilon-caprolactone) (PCL) Heat Capacity, Enthalpy, Entropy, Gibbs Energy: Datasheet from "The Advanced THermal Analysis System (ATHAS) Databank – Polymer Thermodynamics" Release 2014 in SpringerMaterials (https://materials.springer.com/polymerthermodynamics/docs/athas_0049)*, M. Pyda, Editor., Springer-Verlag Berlin Heidelberg & Marek Pyda.
70. Zhuravlev, E., et al., *Kinetics of nucleation and crystallization in poly(ε-caprolactone) (PCL).* Polymer, 2011. **52**(9): p. 1983-1997.
71. Wurm, A., et al., *Crystallization and Homogeneous Nucleation Kinetics of Poly(ε-caprolactone) (PCL) with Different Molar Masses.* Macromolecules, 2012. **45**(9): p. 3816-3828.
72. Androsch, R., C. Schick, and A.M. Rhoades, *Application of Tammann's Two-Stage Crystal Nuclei Development Method for Analysis of the Thermal Stability of Homogeneous Crystal Nuclei of Poly(ethylene terephthalate).* Macromolecules, 2015. **48**(22): p. 8082-8089.
73. Zhuravlev, E., et al., *Experimental Test of Tammann's Nuclei Development Approach in Crystallization of Macromolecules.* Crystal Growth & Design, 2015. **15**(2): p. 786-798.
74. Androsch, R. and C. Schick, *Interplay between the Relaxation of the Glass of Random l/d-Lactide Copolymers and Homogeneous Crystal Nucleation: Evidence for Segregation of Chain Defects.* J Phys Chem B, 2016. **120**(19): p. 4522-8.
75. Li, L., et al., *A Direct Observation of the Formation of Nuclei and the Development of Lamellae in Polymer Spherulites.* Macromolecules, 1999. **32**: p. 8240-8242.
76. Lei, Y.-G., et al., *Growth process of homogeneously and heterogeneously nucleated spherulites as observed by atomic force microscopy.* Polymer, 2003. **44**(16): p. 4673-4679.
77. Humphris, A.D.L., M.J. Miles, and J.K. Hobbs, *A mechanical microscope: High-speed atomic force microscopy.* Applied Physics letters, 2005. **86**: p. 034106.
78. Kailas, L., et al., *A Real-Time Study of Homogeneous Nucleation, Growth, and Phase Transformations in Nanodroplets of Low Molecular Weight Isotactic Polypropylene*

Using AFM. Macromolecules, 2007. **40**: p. 7223-7230.

79. Zhao, B., et al., *Large scan area high-speed atomic force microscopy using a resonant scanner.* Reviews of Scientific Instruments, 2009. **80**(9): p. 093707.
80. Chan, C.-M. and L. Li, *Direct Observation of the Growth of Lamellae and Spherulites by AFM.* Advanced Polymer Science, 2005. **188**: p. 1-41.
81. Zia, Q., R. Androsch, and H.-J. Radusch, *Effect of the Structure at the Micrometer and Nanometer Scales on the Light Transmission of Isotactic Polypropylene.* Journal of Applied Polymer Science, 2010. **117**: p. 1013–1020.
82. Androsch, R. and M.L. Di Lorenzo, *Crystal Nucleation in Glassy Poly(l-lactic acid).* Macromolecules, 2013. **46**(15): p. 6048-6056.
83. Rhoades, A.M., et al., *Effect of cooling rate on the crystal polymorphism in beta-nucleated isotactic polypropylene as revealed by a combined WAXS/FSC analysis.* 2016. **1736**: p. 020076.
84. Cebe, P., et al., *Using flash DSC for determining the liquid state heat capacity of silk fibroin.* Abstracts of papers, 2015. **615**: p. 8-14.
85. Anfatec. Measurement Science and Technology & Scanning Probe Microscopy]. Available from: http://www.anfatec.de/anfatec/mic.html.
86. La Spina, L., et al., *Reduction of surface roughness of a silicon chip for advanced nanocalorimetry.* Sensors and Actuators A: Physical, 2008. **144**(2): p. 403-409.
87. van Herwaarden, A.W., *Overview of calorimeter chips for various applications.* Thermochimica Acta, 2005. **432**(2): p. 192-201.
88. Zhuravlev, E. and C. Schick, *Fast scanning power compensated differential scanning nano-calorimeter: 1. The device.* Thermochimica Acta, 2010. **505**(1-2): p. 1-13.
89. Zhuravlev, E. and C. Schick, *Fast scanning power compensated differential scanning nano-calorimeter: 2. Heat capacity analysis.* Thermochimica Acta, 2010. **505**(1-2): p. 14-21.
90. Micromasch. *AFM Probe NSC 14*. Cantilevers of the 14 series are generally used in tapping mode for imaging relatively soft samples to obtain better phase contrast and reduce surface deformations caused by tip tapping. Probes with coatings can also be used in conductive AFM techniques.]. Available from: https://www.spmtips.com/afm-probes-14-series.afm.
91. Nunano. Available from: https://www.nunano.com/store/scout-70r.
92. Pearce, R. and G.J. Vancso, *Imaging of Melting and Crystallization of Poly(ethylene oxide) in Real-Time by Hot-Stage Atomic Force Microscopy.* Macromolecules, 1997. **30**: p. 5843-5848.
93. Zhu, D., et al., *AFM-tip-induced crystallization of poly(ethylene oxide) melt droplets.* Frontiers of Chemistry in China, 2007. **2**(2): p. 174-177.
94. Keith, H.D. and F.J. Padden Jr., *Twisting orientation and the role of transient states in polymer crystallization.* Polymer, 1984. **25**: p. 28-42.
95. Zhang, H., et al., *Correlating polymer crystals via self-induced nucleation.* Phys Rev Lett, 2014. **112**(23): p. 237801.
96. Majumder, S., et al., *Controlling the Growth of Stacks of Correlated Lamellar Crystals*

of a Block Copolymer. Macromolecules, 2019.

97. Herd, M. and A. Prasad, *On the Observation of a New Morphology in Poly(ary1ene ether ether ketone). A Further Examination of the Double Endothermic Behavior of Poly(ary1ene ether ether ketone).* Macromolecules, 1992. **25**: p. 1731-1736.
98. Ye Sun, H.X., Shuang Chen, M. D. Ediger, Lian Yu, *Crystallization near Glass Transition: Transition from Diffusion-Controlled to Diffusionless Crystal Growth Studied with Seven Polymorphs.* J. Phys. Chem. B, 2008. **112**: p. 5594-5601.
99. Toda, A. and M. Konishi, *An Evaluation of Thermal Lags of Fast-Scan Microchip DSC with Polymer Film Samples.* Thermochimica Acta, 2014. **589**: p. 262-269.
100. G.W.H.Höhne, et al., *The temperature calibration of scanning calorimeters.* Thermochimica Acta, 1990. **160**(1): p. 1-12.
101. Martins, J.A., W. Zhang, and A.M. Brito, *Origin of the melt memory effect in polymer crystallization.* Polymer, 2010. **51**(18): p. 4185-4194.
102. Alfonso, G.C. and P. Scardigli, *Melt memory effects in polymer crystallization.* Macromolecular Symposia, 1997. **118**(1): p. 323-328.
103. Muthukumar, M., *Communication: Theory of melt-memory in polymer crystallization*. 2016, AIP Publishing LLC.
104. Boyd, R.H., *The dielectric constant of lamellar semicrystalline polymer.* J. Polym. Sci.: Polym. Phys. Ed., 1983. **21**: p. 505-514.
105. Langhe, D.S., A. Hiltner, and E. Baer, *Transformation of isotactic polypropylene droplets from the mesophase into the α-phase.* Journal of Polymer Science Part B: Polymer Physics, 2011. **49**: p. 1672-1682.
106. Zia, Q. and R. Androsch, *Effect of atomic force microscope tip geometry on the evaluation of the crystal size of semicrystalline polymers.* Measurement Science and Technology, 2009. **20**(9): p. 097003.
107. Furushima, Y., et al., *Two crystal populations with different melting/reorganization kinetics of isothermally crystallized polyamide 6.* Journal of Polymer Science Part B: Polymer Physics, 2016.
108. *Nylon 6,6 α (NYLON66) Heat Capacity, Enthalpy, Entropy, Gibbs Energy: Datasheet from "The Advanced THermal Analysis System (ATHAS) Databank – Polymer Thermodynamics" Release 2014 in SpringerMaterials (https://materials.springer.com/polymerthermodynamics/docs/athas_0027)*, M. Pyda, Editor., Springer-Verlag Berlin Heidelberg & Marek Pyda.
109. Tammann, G., *Über die Abhängigkeit der Zahl der Kerne, welche sich in verschiedenen unterkühlten Flüssigkeiten bilden, von der Temperatur.* Zeitschrift für Physikalische Chemie, 1898. **25**: p. 441-479.
110. Furushima, Y., et al., *Melting and recrystallization kinetics of poly(butylene terephthalate).* Polymer, 2017. **109**: p. 307-314.
111. Toda, A., R. Androsch, and C. Schick, *Insights into polymer crystallization and melting from fast scanning chip calorimetry.* Polymer, 2016. **91**: p. 239-263.
112. Zhuravlev, E., et al., *Kinetics of nucleation and crystallization of poly(ε-caprolactone) – Multiwalled carbon nanotube composites.* European Polymer Journal, 2014. **52**: p. 1-

11.
113. McKinney, M.L., *Estimating volumetric fossil abundance from cross-sections: a stereological approach.* Palaios, 1986: p. 79-84.
114. Becker, R. and W. Döring, *Kinetische behandlung der keimbildung in übersättigten dämpfen.* Annalen der Physik, 1935. **416**(8): p. 719-752.
115. Volmer, M., *Kinetik der Phasenbildung, Steinkopff, Dresden u.* Stuttgart, Germany, 1939.
116. Frenkel, J., *„Kinetic Theory of Liquids "University Press*. 1946, Oxford.
117. Frensch, H. and B.-J. Jungnickel, *Some novel crystallization kinetic peculiarities in finely dispersing polymer blends.* Colloid & Polymer Science, 1989. **267**(1): p. 16-27.
118. Schmelzer, J.W.P., et al., *Crystallization of glass-forming liquids: Maxima of nucleation, growth, and overall crystallization rates.* Journal of Non-Crystalline Solids, 2015. **429**: p. 24-32.
119. Abyzov, A.S., et al., *The effect of heterogeneous structure of glass-forming liquids on crystal nucleation.* Journal of Non-Crystalline Solids, 2017. **462**: p. 32-40.
120. Hoffman, J.D., G.T. Davis, and J.I. Lauritzen, *The rate of crystallization of linear polymers with chain folding*, in *Treatise on solid state chemistry*. 1976, Springer. p. 497-614.

8 Abbreviations

Polymers names

iPP - isotactic Polypropylene

PA 11 - Polyamide 11

PA 66 - Polyamide 66

BA-C8 - Poly (bisphenol A-co-octane)

PBT - Poly (butylene terephthalate)

PBN - Poly (butylene-2,6-naphthalate)

PCL - Poly (ε-caprolactone)

PE - Polyethylene

PEEK - Poly (ether ether ketone)

Theories and thermal properties items

t - Annealing time

n - Avrami coefficient of crystallization

k_B - Boltzmann constant

CNT - Classical nucleation theory

$\mathrm{CNT}_{\mathrm{low\ temp}}$ - CNT at temperatures near and below T_g ()

α- Critical size of the cluster

T_{sw} - Critical temperature of forming the heterogeneous liquid

X - Crystallinity

ρ_{amor} - Density of amorphous phase

ρ_{crys} - Density of crystalline phase

ρ_{sample} - Density of sample

DNA - Deoxyribonucleic acid

ΔG_{V} - Difference between the free energies of liquid and crystal per unit volume of the crystal

$\Delta\sigma$ - Difference of the specific interfacial energy between melt and crystalline phases

D - Effective diffusion coefficient governing the processes of aggregation of amorphous segments to crystal phase

Δh_{het} - Enthalpy change due to cold crystallization at this heating rate on heterogeneities

Δh_{cc} - Enthalpy of cold-crystallization

$\Delta h'_{\mathrm{cc}}$ - Enthalpy of cold-crystallization with the unit $\mathrm{Jm^{-3}}$

$T_{\mathrm{m,0}}$ - Equilibrium melting temperature

K_{v} - Fitting parameter of Eq.(20) proposed by Abyzov et al.

Q - Fitting parameter of Eq.(20) proposed by Abyzov et al.

$\Delta h_{\mathrm{crys'}}$ - Final enthalpy of primary crystallization at infinite time

FIB - Focused ion beam

$\Delta h_{\mathrm{nucl'}}$ - Limiting cold crystallization enthalpy due to homogeneous nuclei

d_0 - Length of a monomer in the unit cell

A_{cant} - Maximum of amplitude of free cantilever

$\Delta h_{\mathrm{recovery.max}}$ - Maximum of enthalpy recovery

F_{tip} - Maximum of stress that tip works on the sample surface

D_0 - Maximum value of effective diffusion coefficient

Δh - Measured heat of fusion

$\Delta \Phi$ - Measured heat flow step at the glass transition of the fully amorphous sample

$N_{v}(t, T)$ - Nuclei density at different annealing times and temperatures

$t_{1/2 \text{ nucl}}$ - Half-time of nucleation

$t_{1/2}$ - Half-time of crystallization

Δh^{∞} - Heat of fusion of the fully crystalline material

ß - Heating rate

HRTEM - High-resolution transmission electron microscopy

t_{ind} - Induction time of nucleation

$T_{\text{m,onset}}$ - Onset temperature of melting peak

$t_{\text{ind cry}}$ - Onset time of crystallization

t_{onset} - Onset time of the curve of nuclei density against time

$T_{\text{m,peak}}$ - Peak temperature of melting peak

h - Planck constant

m - Sample mass

A_2 - Secondary crystallization parameter of the Avrami equation

$\Delta h'_{\text{cc}}(t, T)$ - Specific enthalpy with the unit Jm^{-3} at different annealing times and temperatures

ΔC_{p} - Specific heat capacity at the glass transition step

Δh_{cc} - Specific heat of cold-crystallization

$\Delta h'_{\text{cc,single}}$ - Specific heat of a single nucleus at reheating at 10,000 Ks^{-1} with the unit Jm^{-3}

Specific surface free energy of the critical nucleus-melt interface (σ)

K - Spring-constant

I_{st} - steady-state nucleation rate

W_c - The work of formation of a nucleus of critical size

$\Delta h'_{total}$ - Total enthalpy with the unit Jm^{-3}

$N_v(t)$ - Time-dependence of the number of super-critical nuclei per unit volume of the system

τ - Time-lag required to establish the critical size of nuclei

$P(T)$ - Volume proportionality of the liquid-like amorphous phase in the total amorphous region at a particular temperature

VFT - Vogel–Fulcher–Tammann

A - VFT fitting parameter A

B - VFT fitting parameter B

T_0 - Vogel temperature

Devices and electronics names

AFM - Atomic force microscopy

AFM-FSC - Atomic force microscopy – combination - fast scanning calorimetry

DSC - Differential scanning calorimetry

FSC - Fast scanning calorimetry

Appendix

A1: AFM images by repeating experiments

The AFM experiment has been repeated to check the repeatability and to estimate the error bar, as shown in Figure S1.

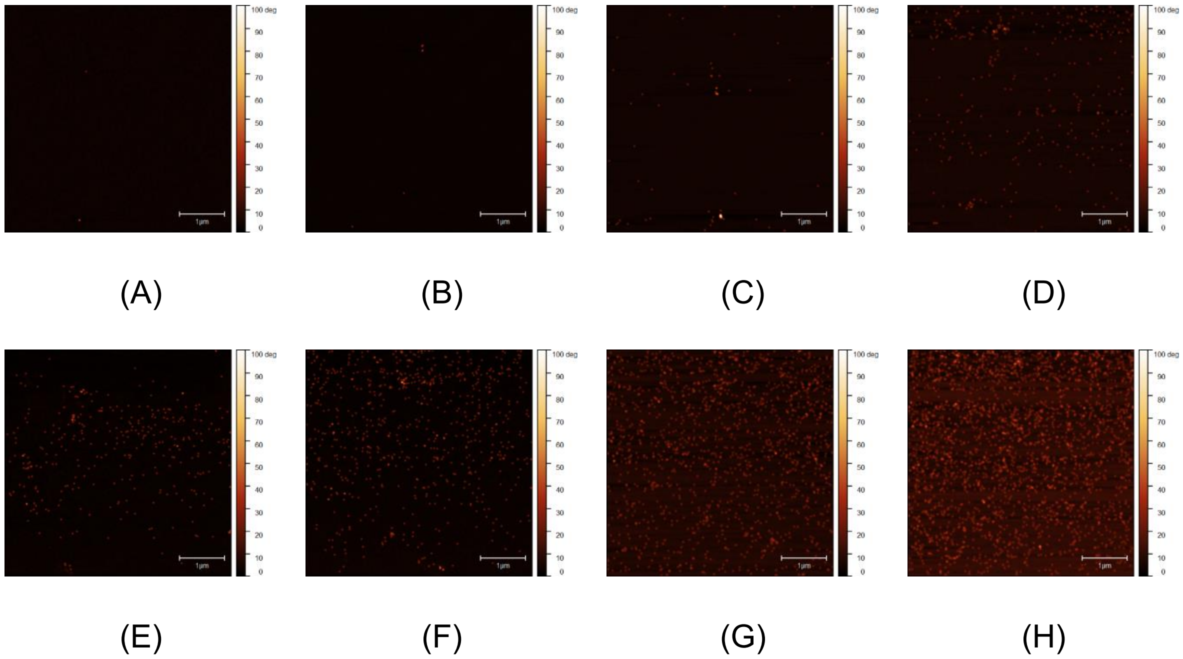

(A) (B) (C) (D)

(E) (F) (G) (H)

Figure A1. AFM image of PA 66 (Phase of angle) after thermal treatment for growing nuclei with different annealing times (A) 2 s, (B) 4 s, (C) 10 s, (D) 20 s, (E) 40, (F) 100 s, (G) 200 s, (H) 400 s.

A2: Influence of Oven Temperature on Specific Enthalpy

The specific heat capacity against temperature by FSC with oven temperatures of 278 K and 83 K is shown in Figure S2 (A) and (B). Both figures show similar curves. The integrated results of cold-crystallization are shown in Figure S2 (C) and (D), respectively. The data obtained from FSC with an oven temperature of 83 K displays better linearity than the data at 278 K because some extra enthalpy is introduced at the time between the previous isothermal annealing and reheating. This external enthalpy influences the linearity of the data at short annealing times. Furthermore, even with extra enthalpy, the fitting shows the same result. The curve of 83 K shows the same value but with a smaller uncertainty than the curve of 278 K.

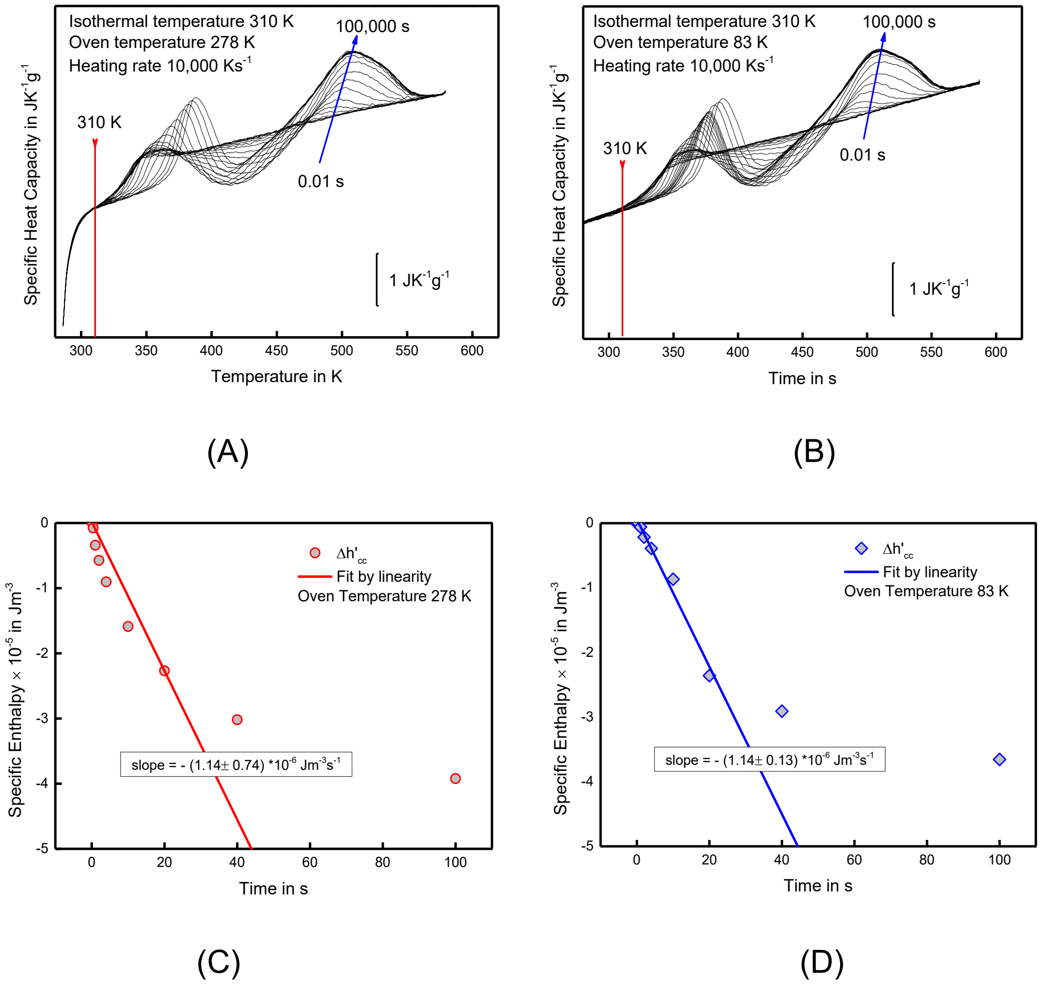

(A)

(B)

(C)

(D)

Figure A2. Specific heat capacity against temperature with oven temperatures 278 K (A) and 83 K (B). Specific enthalpy against annealing time with oven temperatures 278 K (C) and 83 K (D).

A3: Isothermal Experiments at Different Annealing Temperatures

Figure S3 shows the FSC reheating curve of isothermal annealing at different temperatures from 315 to 420 K. The nucleation kinetics is studied by cold-crystallization behavior and fitted by double Avrami Fitting, as shown in Figure

A4. The crystallization kinetics is shown in Figure A5.

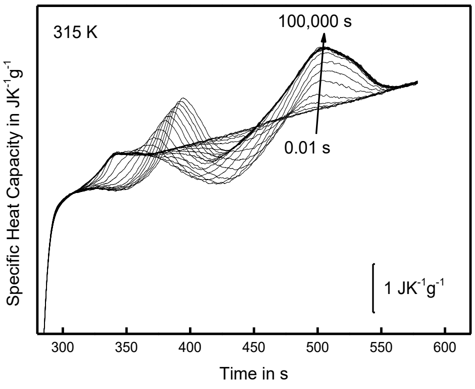

(A)

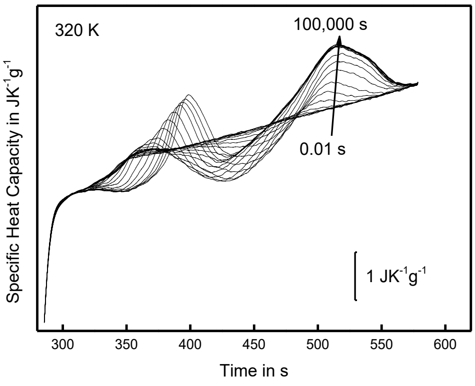

(B)

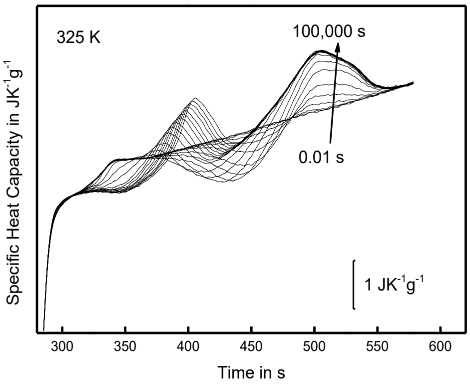

(C)

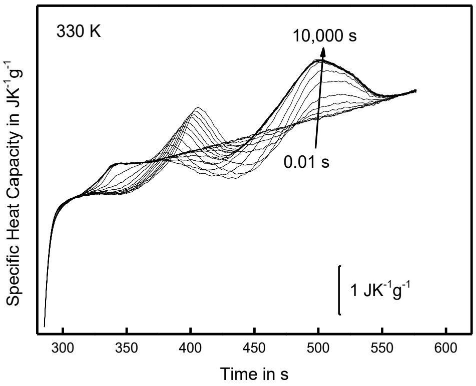

(D)

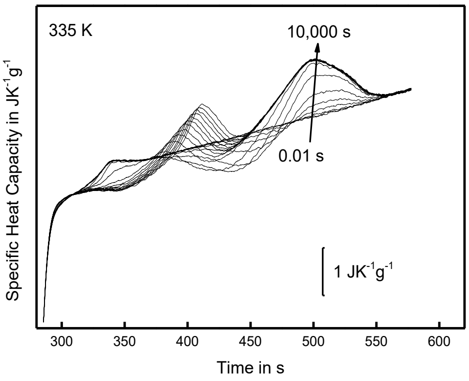

(E)

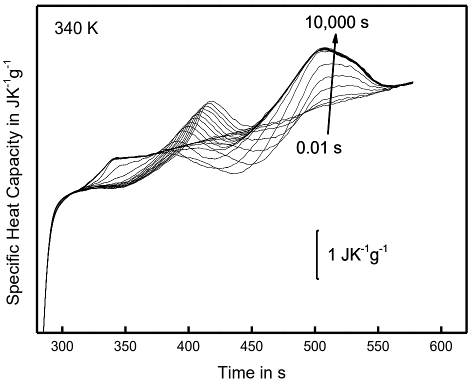

(F)

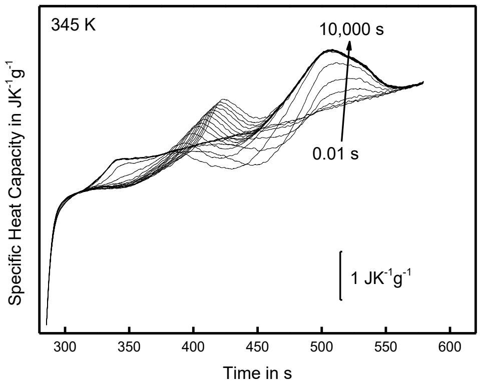
345 K
10,000 s
0.01 s
1 JK^{-1}g^{-1}
Specific Heat Capacity in JK^{-1}g^{-1}
300
350
400
450
500
550
600
Time in s

(G)

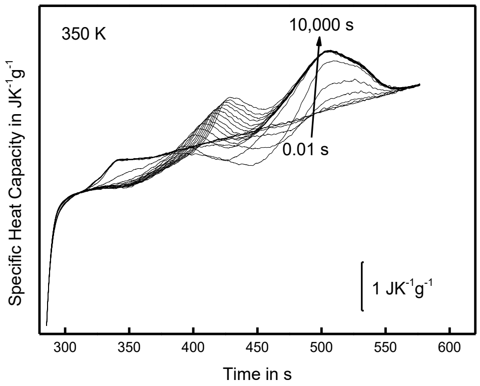
350 K
10,000 s
0.01 s
1 JK^{-1}g^{-1}
Specific Heat Capacity in JK^{-1}g^{-1}
300
350
400
450
500
550
600
Time in s

(H)

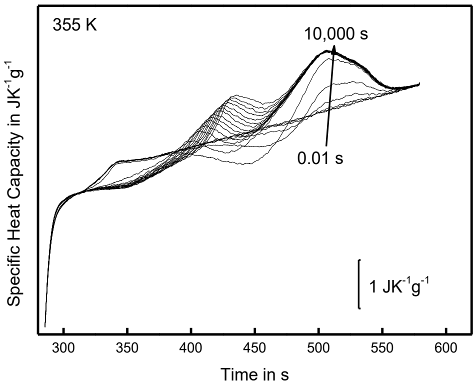
355 K
10,000 s
0.01 s
1 JK^{-1}g^{-1}
Specific Heat Capacity in JK^{-1}g^{-1}
300
350
400
450
500
550
600
Time in s

(I)

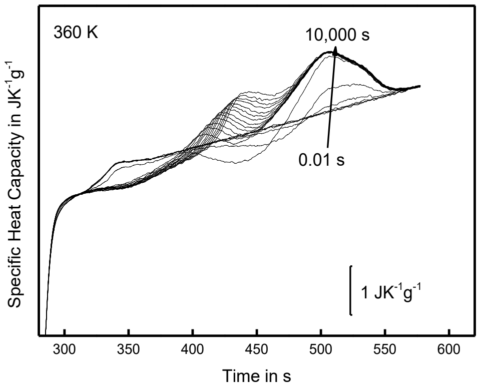
360 K
10,000 s
0.01 s
1 JK^{-1}g^{-1}
Specific Heat Capacity in JK^{-1}g^{-1}
300
350
400
450
500
550
600
Time in s

(J)

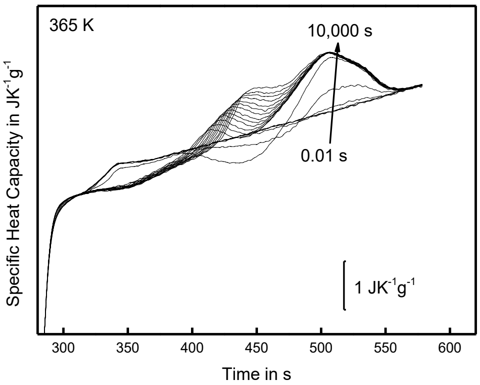
365 K
10,000 s
0.01 s
1 JK^{-1}g^{-1}
Specific Heat Capacity in JK^{-1}g^{-1}
300
350
400
450
500
550
600
Time in s

(K)

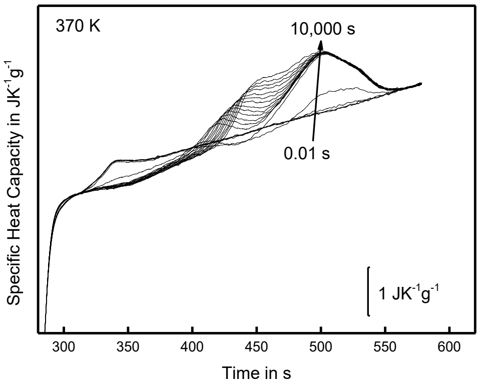
370 K
10,000 s
0.01 s
1 JK^{-1}g^{-1}
Specific Heat Capacity in JK^{-1}g^{-1}
300
350
400
450
500
550
600
Time in s

(L)

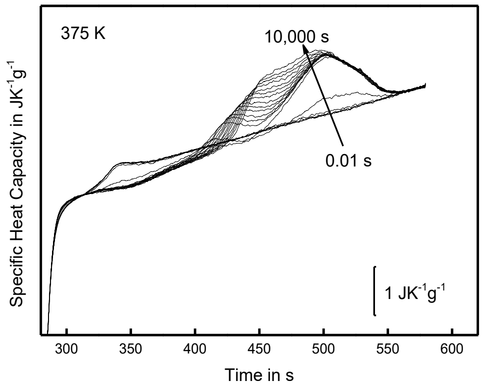
375 K
10,000 s
0.01 s
1 JK-1g-1
Specific Heat Capacity in JK-1g-1
300
350
400
450
500
550
600
Time in s

(M)

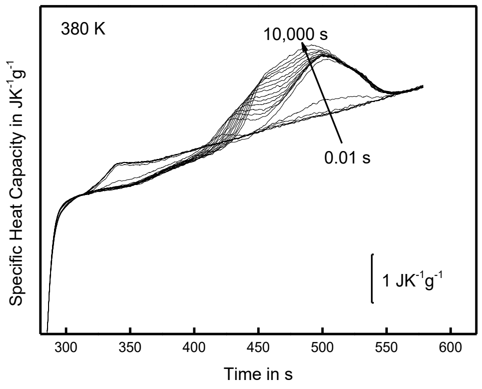
380 K
10,000 s
0.01 s
1 JK-1g-1
Specific Heat Capacity in JK-1g-1
300
350
400
450
500
550
600
Time in s

(N)

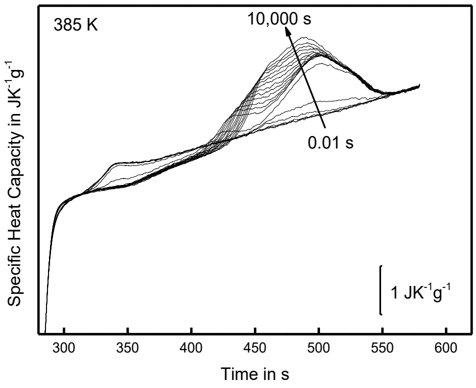
385 K
10,000 s
0.01 s
1 JK-1g-1
Specific Heat Capacity in JK-1g-1
300
350
400
450
500
550
600
Time in s

(O)

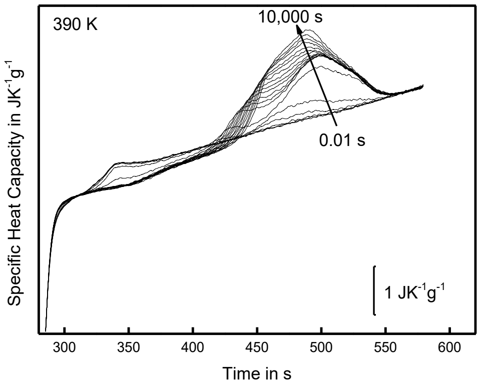
390 K
10,000 s
0.01 s
1 JK-1g-1
Specific Heat Capacity in JK-1g-1
300
350
400
450
500
550
600
Time in s

(P)

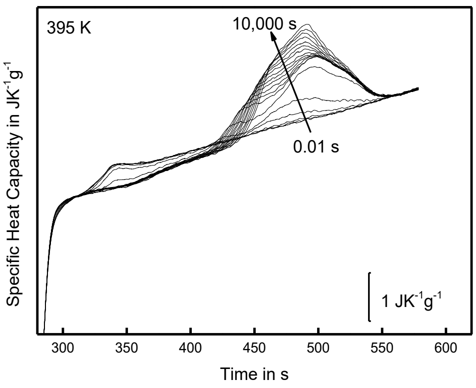
395 K
10,000 s
0.01 s
1 JK-1g-1
Specific Heat Capacity in JK-1g-1
300
350
400
450
500
550
600
Time in s

(Q)

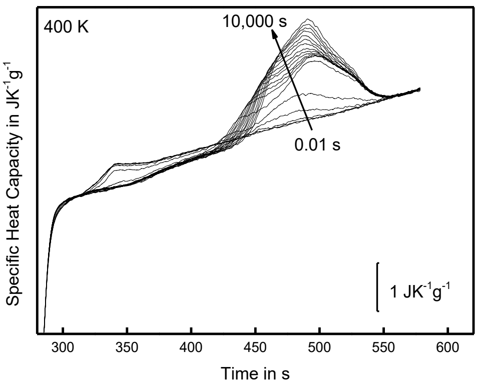
400 K
10,000 s
0.01 s
1 JK-1g-1
Specific Heat Capacity in JK-1g-1
300
350
400
450
500
550
600
Time in s

(R)

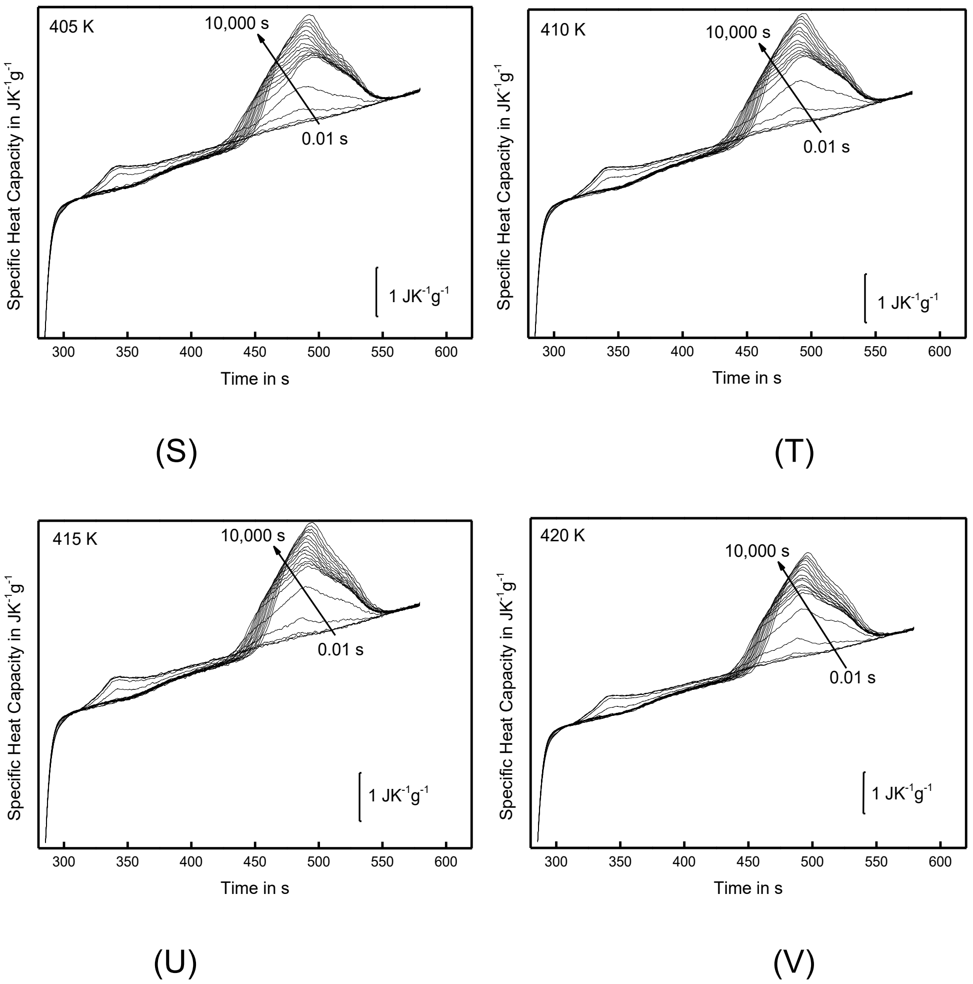

Figure A3. FSC heat scans of PA 66 after isothermal annealing at different temperatures; (A) 315 K, (B) 320 K, (C) 325 K, (D) 330 K, (E) 335 K, (F) 340 K, (G) 345 K, (H) 350 K, (I) 355 K, (J) 360 K, (K) 365 K, (L) 370 K, (M) 375 K, (N) 380 K, (O) 385 K, (P) 390 K, (Q) 395 K, (R) 400 K, (S) 405 K, (T) 410 K, (U) 415 K, (V) 420 K.

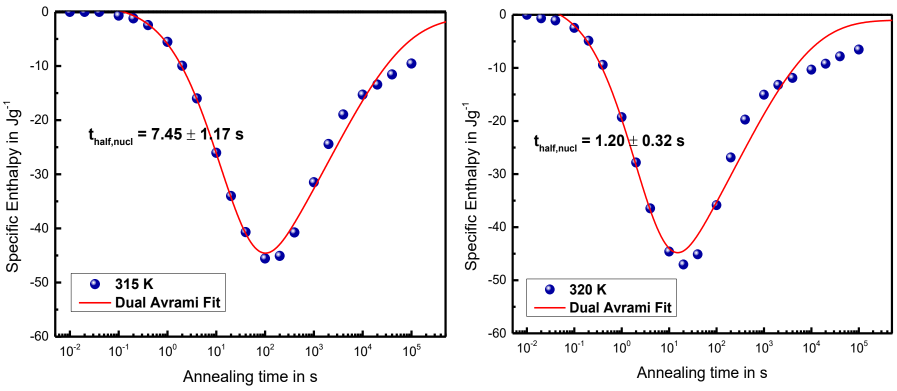

(A) (B)

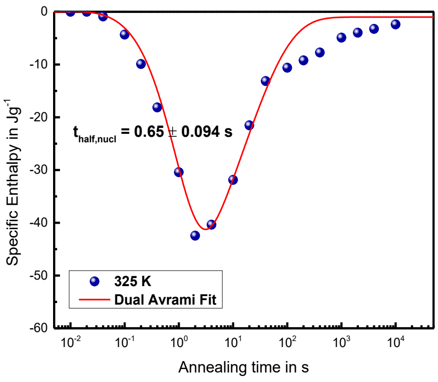
0
-10
-20
-30
-40
-50
-60
Specific Enthalpy in Jg-1
t half,nucl = 0.65 ± 0.094 s
325 K
Dual Avrami Fit
10-2
10-1
100
101
102
103
104
Annealing time in s

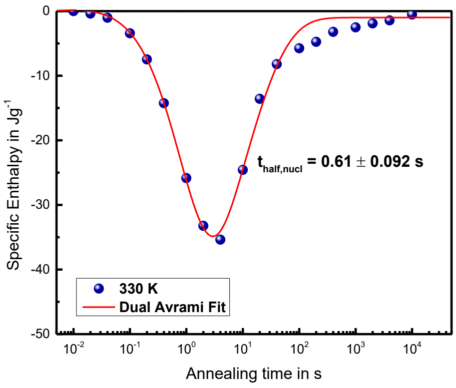
0
-10
-20
-30
-40
-50
Specific Enthalpy in Jg-1
t half,nucl = 0.61 ± 0.092 s
330 K
Dual Avrami Fit
10-2
10-1
100
101
102
103
104
Annealing time in s

(C) (D)

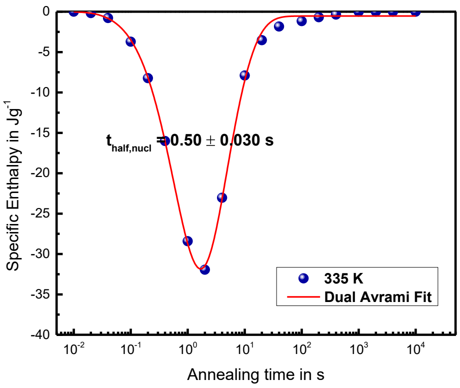
0
-5
-10
-15
-20
-25
-30
-35
-40
Specific Enthalpy in Jg-1
t half,nucl = 0.50 ± 0.030 s
335 K
Dual Avrami Fit
10-2
10-1
100
101
102
103
104
Annealing time in s

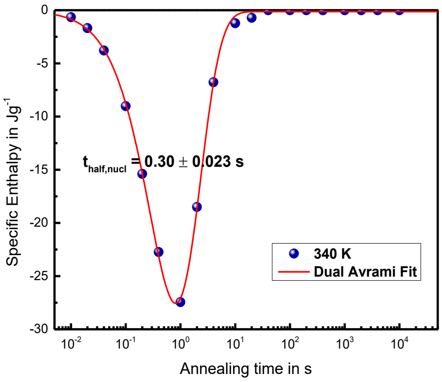
0
-5
-10
-15
-20
-25
-30
Specific Enthalpy in Jg-1
t half,nucl = 0.30 ± 0.023 s
340 K
Dual Avrami Fit
10-2
10-1
100
101
102
103
104
Annealing time in s

(E) (F)

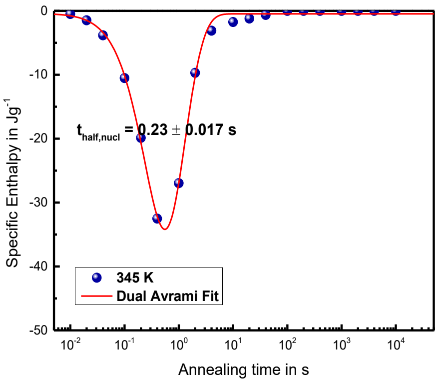
0
-10
-20
-30
-40
-50
Specific Enthalpy in Jg-1
t half,nucl = 0.23 ± 0.017 s
345 K
Dual Avrami Fit
10-2
10-1
100
101
102
103
104
Annealing time in s

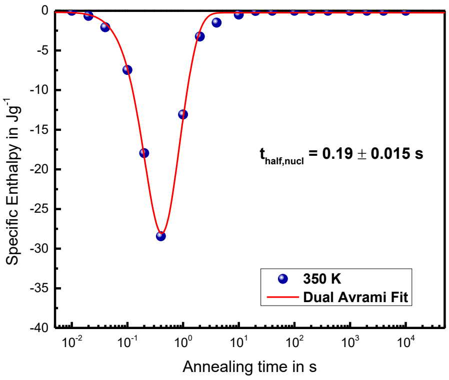
0
-5
-10
-15
-20
-25
-30
-35
-40
Specific Enthalpy in Jg-1
t half,nucl = 0.19 ± 0.015 s
350 K
Dual Avrami Fit
10-2
10-1
100
101
102
103
104
Annealing time in s

(G) (H)

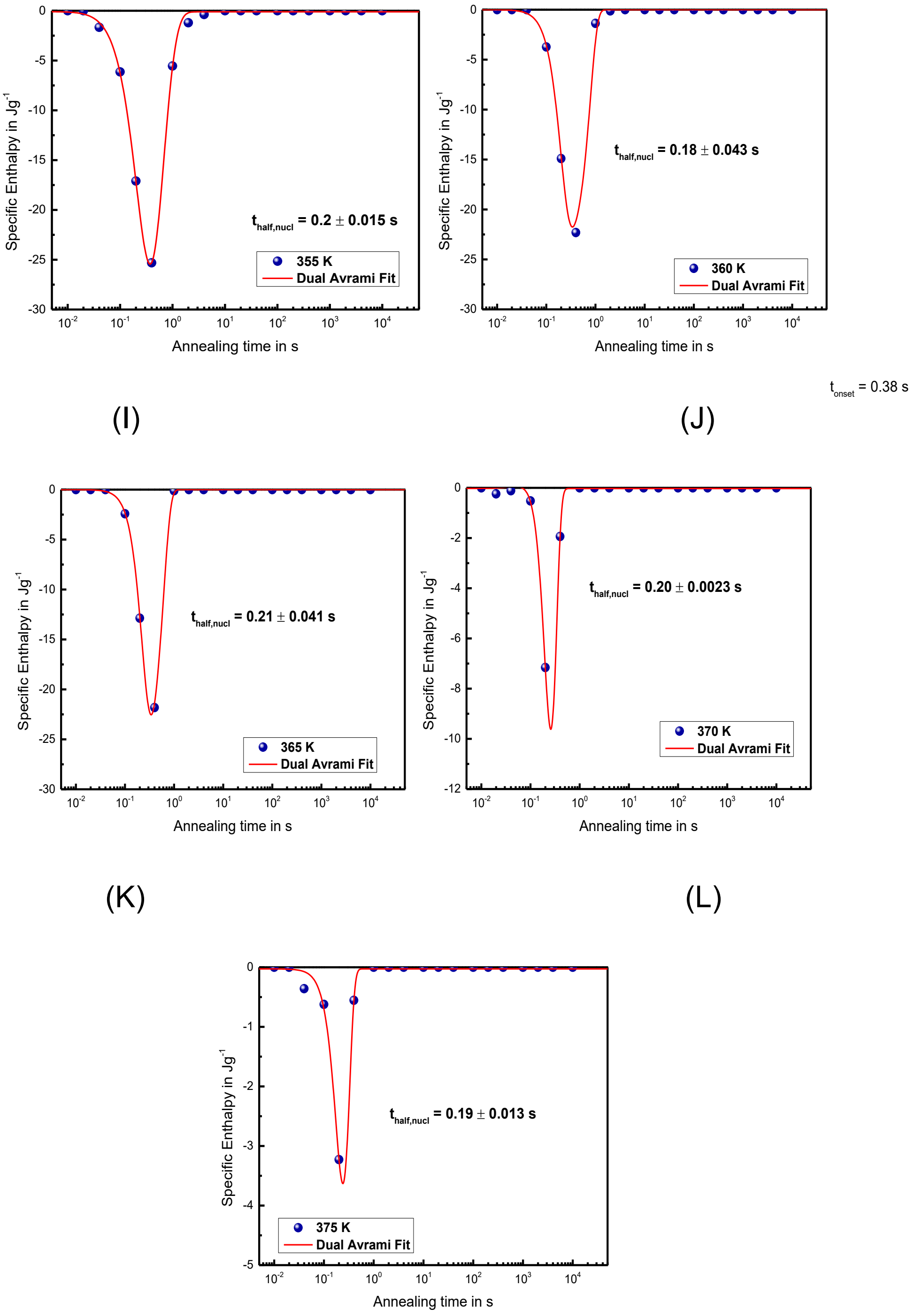

(I)

(J)

(K)

(L)

(M)

Figure A4. Δh_{cc} against annealing time at different temperatures; (A) 315 K, (B) 320 K, (C) 325 K, (D) 330 K, (E) 335 K, (F) 340 K, (G) 345 K, (H) 350 K, (I) 355 K, (J) 360 K, (K) 365 K, (L) 370 K, (M) 375 K. The data are fitted by double Avrami equation (see Eq.(1) in main text).

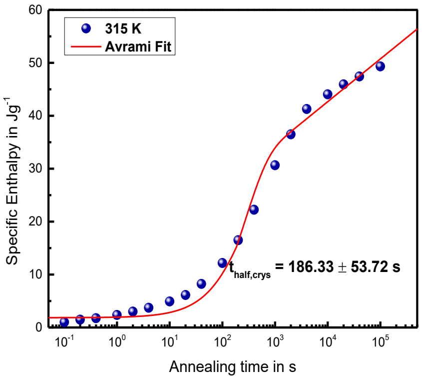
315 K
Avrami Fit
$t_{half,crys}$ = 186.33 ± 53.72 s
Specific Enthalpy in Jg^{-1}
Annealing time in s
0
10
20
30
40
50
60
10^{-1}
10^{0}
10^{1}
10^{2}
10^{3}
10^{4}
10^{5}

(A)

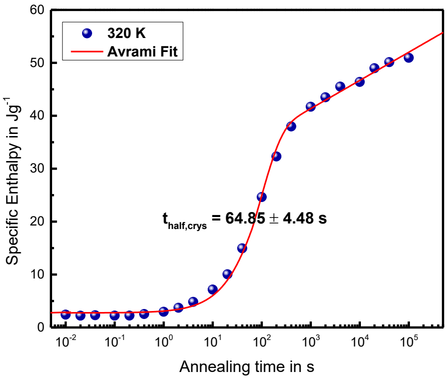
320 K
Avrami Fit
$t_{half,crys}$ = 64.85 ± 4.48 s
Specific Enthalpy in Jg^{-1}
Annealing time in s
0
10
20
30
40
50
60
10^{-2}
10^{-1}
10^{0}
10^{1}
10^{2}
10^{3}
10^{4}
10^{5}

(B)

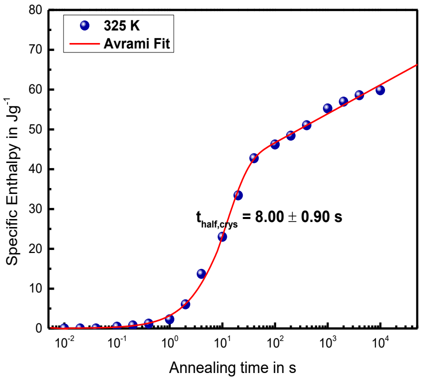
325 K
Avrami Fit
$t_{half,crys}$ = 8.00 ± 0.90 s
Specific Enthalpy in Jg^{-1}
Annealing time in s
0
10
20
30
40
50
60
70
80
10^{-2}
10^{-1}
10^{0}
10^{1}
10^{2}
10^{3}
10^{4}

(C)

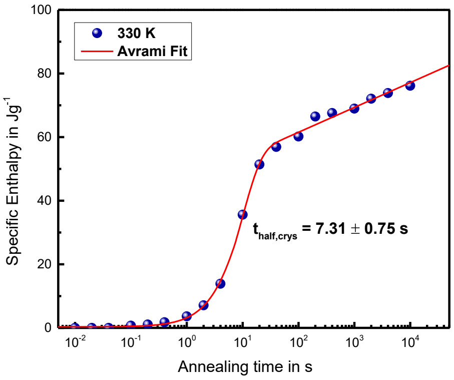
330 K
Avrami Fit
$t_{half,crys}$ = 7.31 ± 0.75 s
Specific Enthalpy in Jg^{-1}
Annealing time in s
0
20
40
60
80
100
10^{-2}
10^{-1}
10^{0}
10^{1}
10^{2}
10^{3}
10^{4}

(D)

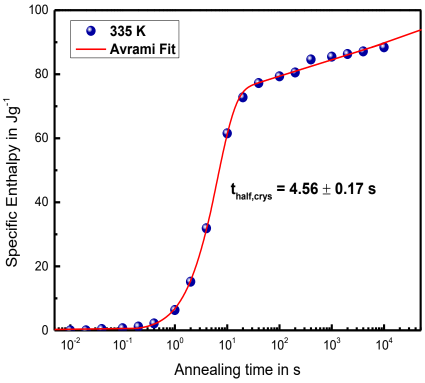
335 K
Avrami Fit
$t_{half,crys}$ = 4.56 ± 0.17 s
Specific Enthalpy in Jg^{-1}
Annealing time in s
0
20
40
60
80
100
10^{-2}
10^{-1}
10^{0}
10^{1}
10^{2}
10^{3}
10^{4}

(E)

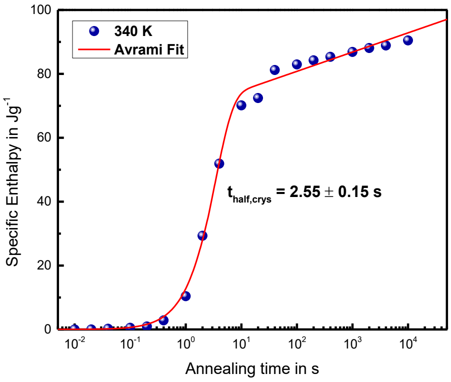
340 K
Avrami Fit
$t_{half,crys}$ = 2.55 ± 0.15 s
Specific Enthalpy in Jg^{-1}
Annealing time in s
0
20
40
60
80
100
10^{-2}
10^{-1}
10^{0}
10^{1}
10^{2}
10^{3}
10^{4}

(F)

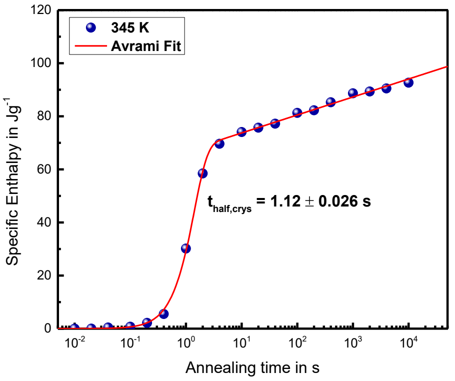
345 K
Avrami Fit
$t_{half,crys}$ = 1.12 ± 0.026 s
Specific Enthalpy in Jg^{-1}
Annealing time in s
0
20
40
60
80
100
120
10^{-2}
10^{-1}
10^{0}
10^{1}
10^{2}
10^{3}
10^{4}

(G)

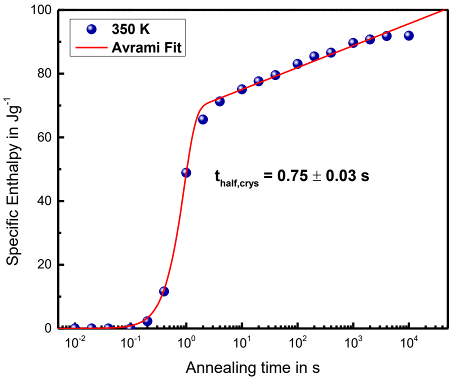
350 K
Avrami Fit
$t_{half,crys}$ = 0.75 ± 0.03 s
Specific Enthalpy in Jg^{-1}
Annealing time in s
0
20
40
60
80
100
10^{-2}
10^{-1}
10^{0}
10^{1}
10^{2}
10^{3}
10^{4}

(H)

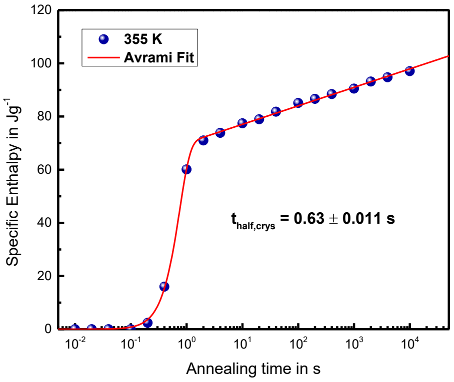
355 K
Avrami Fit
$t_{half,crys}$ = 0.63 ± 0.011 s
Specific Enthalpy in Jg^{-1}
Annealing time in s
0
20
40
60
80
100
120
10^{-2}
10^{-1}
10^{0}
10^{1}
10^{2}
10^{3}
10^{4}

(I)

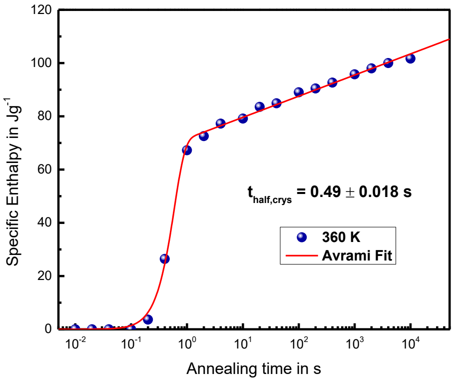
$t_{half,crys}$ = 0.49 ± 0.018 s
360 K
Avrami Fit
Specific Enthalpy in Jg^{-1}
Annealing time in s
0
20
40
60
80
100
120
10^{-2}
10^{-1}
10^{0}
10^{1}
10^{2}
10^{3}
10^{4}

(J)

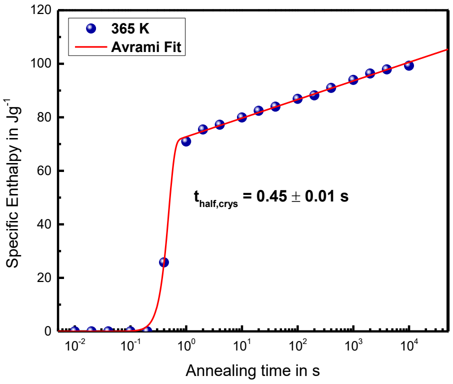
365 K
Avrami Fit
$t_{half,crys}$ = 0.45 ± 0.01 s
Specific Enthalpy in Jg^{-1}
Annealing time in s
0
20
40
60
80
100
120
10^{-2}
10^{-1}
10^{0}
10^{1}
10^{2}
10^{3}
10^{4}

(K)

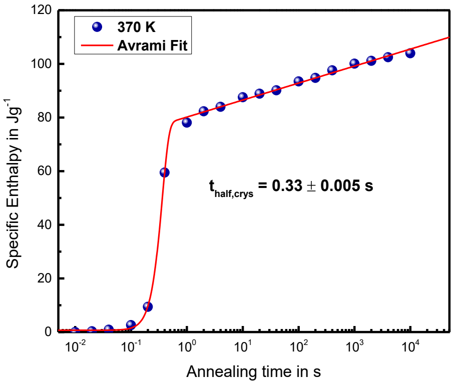
370 K
Avrami Fit
$t_{half,crys}$ = 0.33 ± 0.005 s
Specific Enthalpy in Jg^{-1}
Annealing time in s
0
20
40
60
80
100
120
10^{-2}
10^{-1}
10^{0}
10^{1}
10^{2}
10^{3}
10^{4}

(L)

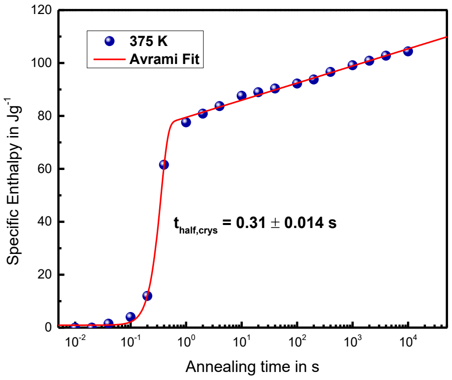
375 K
Avrami Fit
$t_{half,crys}$ = 0.31 ± 0.014 s
Specific Enthalpy in Jg^{-1}
Annealing time in s
0
20
40
60
80
100
120
10^{-2}
10^{-1}
10^{0}
10^{1}
10^{2}
10^{3}
10^{4}

(M)

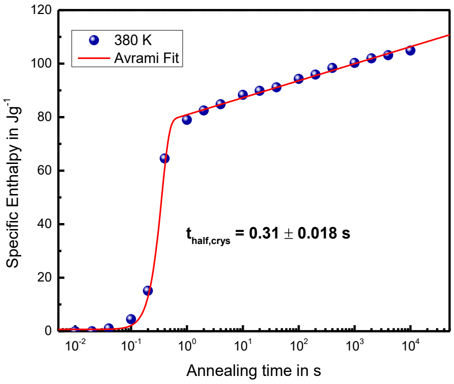
380 K
Avrami Fit
$t_{half,crys}$ = 0.31 ± 0.018 s
Specific Enthalpy in Jg^{-1}
Annealing time in s
0
20
40
60
80
100
120
10^{-2}
10^{-1}
10^{0}
10^{1}
10^{2}
10^{3}
10^{4}

(N)

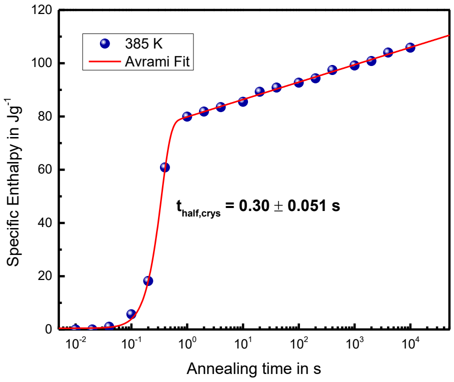
385 K
Avrami Fit
$t_{half,crys}$ = 0.30 ± 0.051 s
Specific Enthalpy in Jg^{-1}
Annealing time in s
0
20
40
60
80
100
120
10^{-2}
10^{-1}
10^{0}
10^{1}
10^{2}
10^{3}
10^{4}

(O)

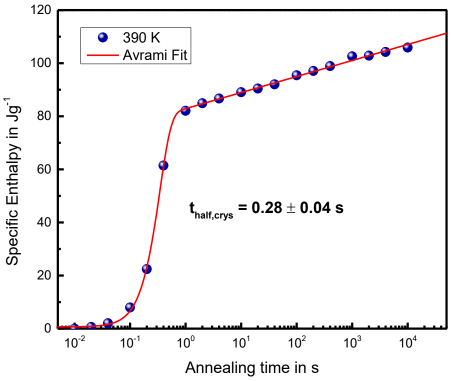
390 K
Avrami Fit
$t_{half,crys}$ = 0.28 ± 0.04 s
Specific Enthalpy in Jg^{-1}
Annealing time in s
0
20
40
60
80
100
120
10^{-2}
10^{-1}
10^{0}
10^{1}
10^{2}
10^{3}
10^{4}

(P)

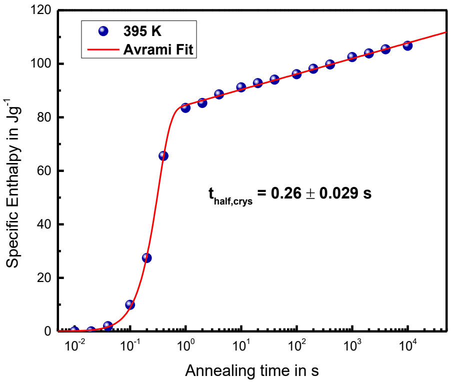
395 K
Avrami Fit
$t_{half,crys}$ = 0.26 ± 0.029 s
Specific Enthalpy in Jg^{-1}
Annealing time in s
0
20
40
60
80
100
120
10^{-2}
10^{-1}
10^{0}
10^{1}
10^{2}
10^{3}
10^{4}

(Q)

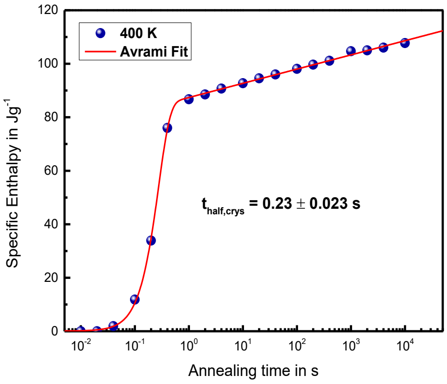
400 K
Avrami Fit
$t_{half,crys}$ = 0.23 ± 0.023 s
Specific Enthalpy in Jg^{-1}
Annealing time in s
0
20
40
60
80
100
120
10^{-2}
10^{-1}
10^{0}
10^{1}
10^{2}
10^{3}
10^{4}

(R)

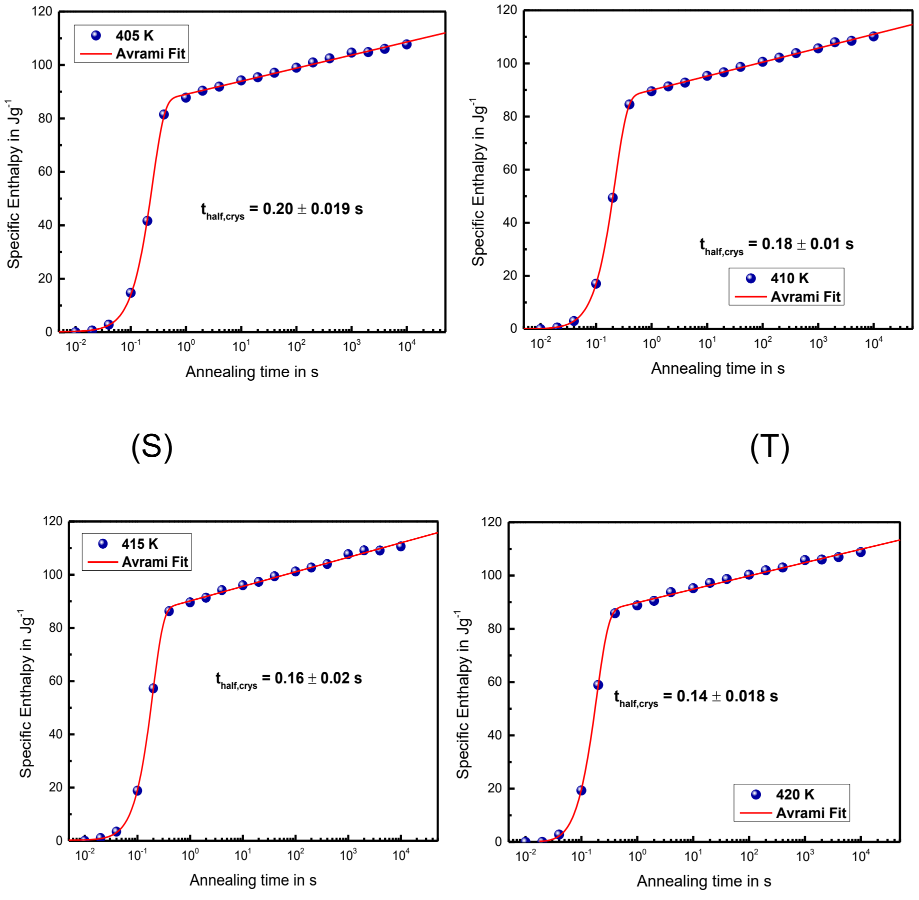

(S) (T)

(U) (V)

Figure A5. Δh_{total} against annealing time at different temperatures; (A) 315 K, (B) 320 K, (C) 325 K, (D) 330 K, (E) 335 K, (F) 340 K, (G) 345 K, (H) 350 K, (I) 355 K, (J) 360 K, (K) 365 K, (L) 370 K, (M) 375 K, (N) 380 K, (O) 385 K, (P) 390 K, (Q) 395 K, (R) 400 K, (S) 405 K, (T) 410 K, (U) 415 K, (V) 420 K. The data are fitted by Avrami equation (see Eq.(2) in main text).

A4: Estimating I_{st} through Isothermal FSC Experiments

As the same way to Figure 13 in the main text, the $N_v(t)$ at different temperatures are estimated from FSC data by using Eq.(11) of the main text. Besides, I_{st} at different temperatures are fitted by Eq.(6) in the main text, as shown in Figure S6.

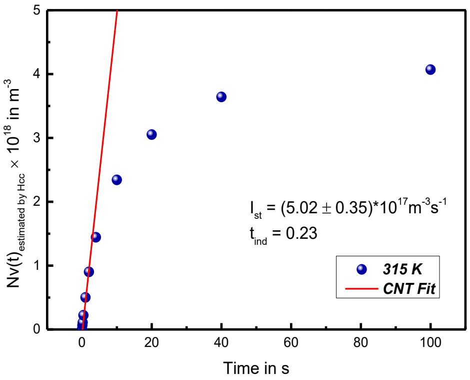
$Nv(t)_{estimated\ by\ Hcc} \times 10^{18}$ in m^{-3}
Time in s
0
1
2
3
4
5
0
20
40
60
80
100
I_{st} = (5.02 ± 0.35)*$10^{17}m^{-3}s^{-1}$
t_{ind} = 0.23
315 K
CNT Fit

(A)

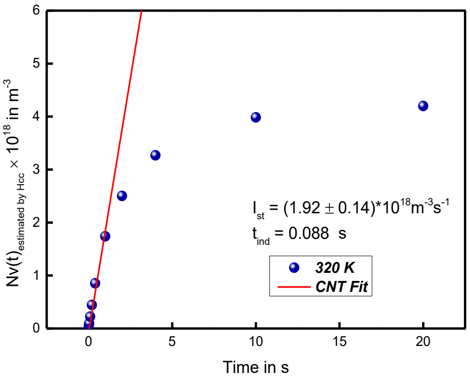
$Nv(t)_{estimated\ by\ Hcc} \times 10^{18}$ in m^{-3}
Time in s
0
1
2
3
4
5
6
0
5
10
15
20
I_{st} = (1.92 ± 0.14)*$10^{18}m^{-3}s^{-1}$
t_{ind} = 0.088 s
320 K
CNT Fit

(B)

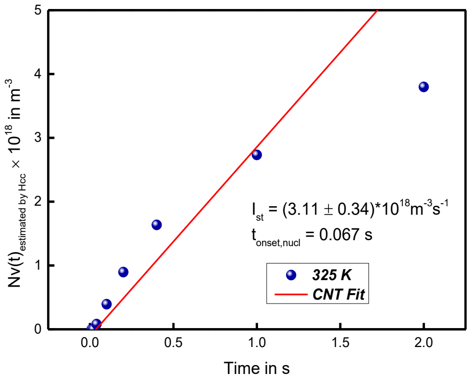
$Nv(t)_{estimated\ by\ Hcc} \times 10^{18}$ in m^{-3}
Time in s
0
1
2
3
4
5
0.0
0.5
1.0
1.5
2.0
I_{st} = (3.11 ± 0.34)*$10^{18}m^{-3}s^{-1}$
$t_{onset,nucl}$ = 0.067 s
325 K
CNT Fit

(C)

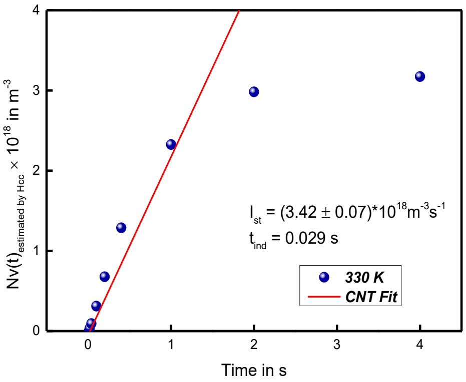
$Nv(t)_{estimated\ by\ Hcc} \times 10^{18}$ in m^{-3}
Time in s
0
1
2
3
4
0
1
2
3
4
I_{st} = (3.42 ± 0.07)*$10^{18}m^{-3}s^{-1}$
t_{ind} = 0.029 s
330 K
CNT Fit

(D)

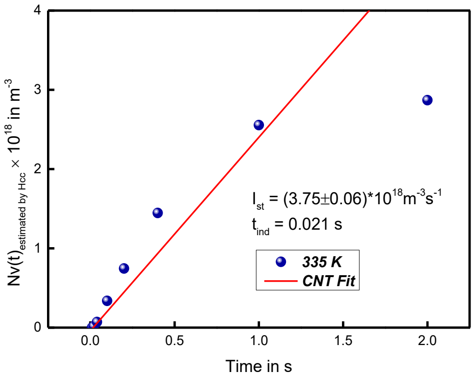
$Nv(t)_{estimated\ by\ Hcc} \times 10^{18}$ in m^{-3}
Time in s
0
1
2
3
4
0.0
0.5
1.0
1.5
2.0
I_{st} = (3.75±0.06)*$10^{18}m^{-3}s^{-1}$
t_{ind} = 0.021 s
335 K
CNT Fit

(E)

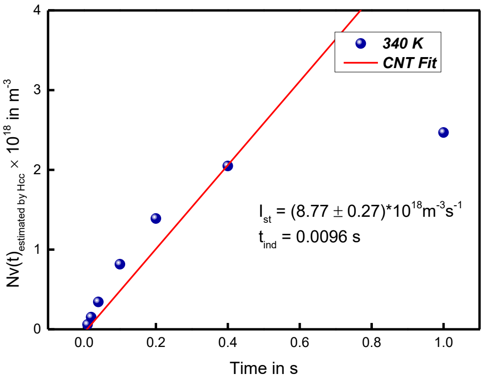
$Nv(t)_{estimated\ by\ Hcc} \times 10^{18}$ in m^{-3}
Time in s
0
1
2
3
4
0.0
0.2
0.4
0.6
0.8
1.0
340 K
CNT Fit
I_{st} = (8.77 ± 0.27)*$10^{18}m^{-3}s^{-1}$
t_{ind} = 0.0096 s

(F)

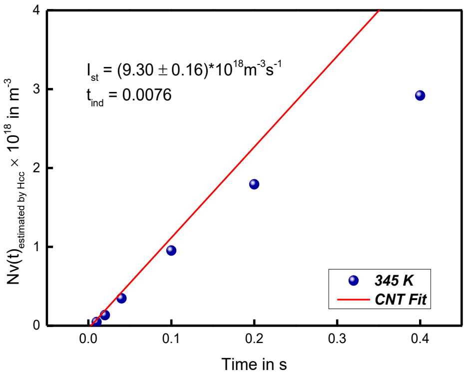
I_{st} = (9.30 ± 0.16)*10^{18}m^{-3}s^{-1}
t_{ind} = 0.0076
345 K
CNT Fit
Nv(t)$_{estimated by Hcc}$ × 10^{18} in m^{-3}
0
1
2
3
4
0.0
0.1
0.2
0.3
0.4
Time in s

(G)

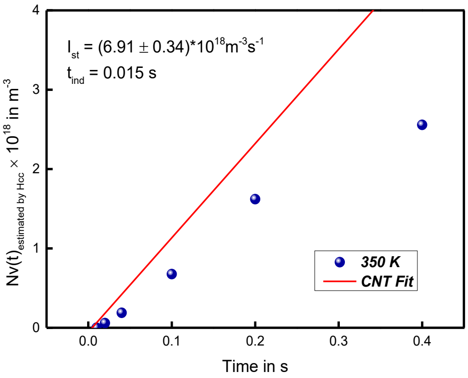
I_{st} = (6.91 ± 0.34)*10^{18}m^{-3}s^{-1}
t_{ind} = 0.015 s
350 K
CNT Fit
Nv(t)$_{estimated by Hcc}$ × 10^{18} in m^{-3}
0
1
2
3
4
0.0
0.1
0.2
0.3
0.4
Time in s

(H)

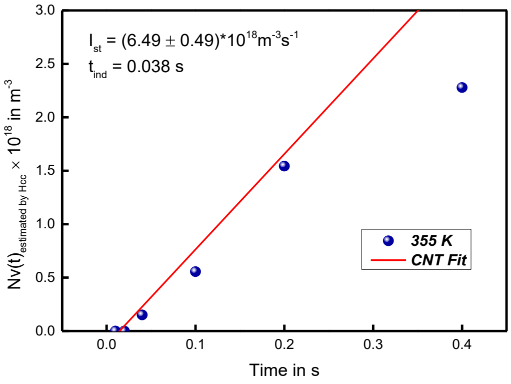
I_{st} = (6.49 ± 0.49)*10^{18}m^{-3}s^{-1}
t_{ind} = 0.038 s
355 K
CNT Fit
Nv(t)$_{estimated by Hcc}$ × 10^{18} in m^{-3}
0.0
0.5
1.0
1.5
2.0
2.5
3.0
0.0
0.1
0.2
0.3
0.4
Time in s

(I)

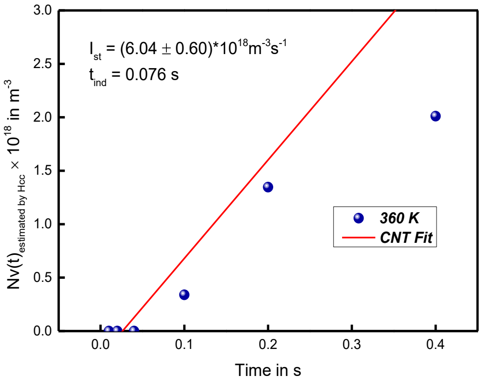
I_{st} = (6.04 ± 0.60)*10^{18}m^{-3}s^{-1}
t_{ind} = 0.076 s
360 K
CNT Fit
Nv(t)$_{estimated by Hcc}$ × 10^{18} in m^{-3}
0.0
0.5
1.0
1.5
2.0
2.5
3.0
0.0
0.1
0.2
0.3
0.4
Time in s

(J)

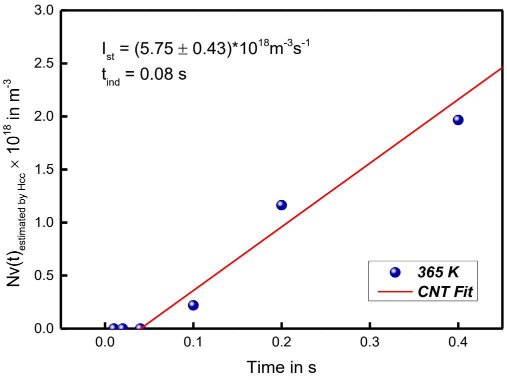
I_{st} = (5.75 ± 0.43)*10^{18}m^{-3}s^{-1}
t_{ind} = 0.08 s
365 K
CNT Fit
Nv(t)$_{estimated by Hcc}$ × 10^{18} in m^{-3}
0.0
0.5
1.0
1.5
2.0
2.5
3.0
0.0
0.1
0.2
0.3
0.4
Time in s

(K)

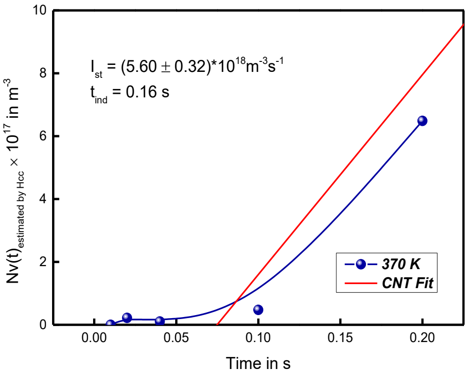
I_{st} = (5.60 ± 0.32)*10^{18}m^{-3}s^{-1}
t_{ind} = 0.16 s
370 K
CNT Fit
Nv(t)$_{estimated by Hcc}$ × 10^{17} in m^{-3}
0
2
4
6
8
10
0.00
0.05
0.10
0.15
0.20
Time in s

(L)

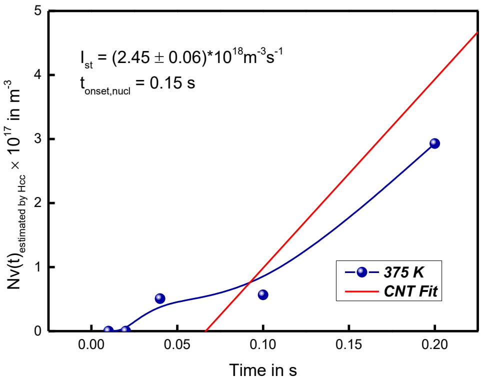

(M)

Figure A6. Nucleation density estimated through FSC data against annealing time at different temperatures; (A) 315 K, (B) 320 K, (C) 325 K, (D) 330 K, (E) 335 K, (F) 340 K, (G) 345 K, (H) 350 K, (I) 355 K, (J) 360 K, (K) 365 K, (L) 370 K, (M) 375 K. The data are fitted by the expression of steady nucleation rate from CNT (see Eq.(6) in main text).

List of Contributions

Publications

[1] **R. Zhang**, E. Zhuravlev, R Androsch, C Schick; Visualization of Polymer Crystallization by in situ Combination of Atomic Force Microscopy and Fast Scanning Calorimetry. Polymers 2019, 11, 890; doi.org/10.3390/polym11050890

[2] **R. Zhang**, E. Zhuravlev, J.W.P. Schmelzer, R Androsch, C Schick; Steady-state crystal nucleation rate of polyamide 66 determined by correlating atomic force microscopy and fast scanning chip calorimetry. Submitted.

[3] R. Androsch, **R. Zhang**, C. Schick, Melt-recrystallization of poly (L-lactic acid) initially containing α-crystals, Polymer, 2019, 176,227-235; doi.org/10.1016/j.polymer.2019.05.052

[4] R. A. Andrianov, R. Androsch, **R. Zhang**, T. A. Mukhametzyanov, A. S. Abyzov, J.W.P. Schmelzer, C. Schick; Growth and dissolution of crystal nuclei in poly(l-lactic acid) (PLLA) in Tammann's development method. Polymer 2020, accepted.

[5] J.W.P. Schmelzer, T.V. Tropin, V.M. Fokin, **R. Zhang**, A. Abdelaziz, Y.Z. Chua, V. Madhavi, T.D. Shaffer, C. Schick; Correlation between glass transition temperature and the width of the glass transition interval. International Journal of Applied Glass Science. 2019, 10, 502-513; doi.org/10.1111/ijag.13240

Conferences

[1] **Rui Zhang**, Evgeny Zhuravlev, Christoph Schick, Crystallization of polymers studied by combining AFM and fast scanning calorimetry. Conference: DPG Dresden 2017At: Dresden, (Poster)

[2] **Rui Zhang**, Evgeny Zhuravlev, Christoph Schick, Crystallization of

PEEK studied by combining AFM and fast scanning calorimetry. 8th IDMRCS 2018 At: Wisła Poland, (Poster)

[3] **Rui Zhang**, Xianru He, Slow Processes in Polymer Many Body System. PCM 2018. At: Kitakyushu, Japan. (Oral Presentation)

[4] **Rui Zhang**, Evgeny Zhuravlev, Christoph Schick, Visualization of Polymer Crystallization by a Combination of Atomic Force Microscopy with Fast Scanning Calorimetry. SPMonSPM 2018. At: Leuven Belgium, (Poster)

[5] **Rui Zhang**, Evgeny Zhuravlev, Christoph Schick, Visualization of Polymer Crystallization by a Combination of Atomic Force Microscopy with Fast Scanning Calorimetry. Crystallization Workshop 2018. At: Genova, Italy. (Poster)

[6] **Rui Zhang**, Evgeny Zhuravlev, Christoph Schick, Visualization of Polymer Crystallization by a Combination of Atomic Force Microscopy with Fast Scanning Calorimetry. ISAC-2018. At Kazan Russia, (Invited Speaker)

[7] **Rui Zhang**, Evgeny Zhuravlev, Christoph Schick, Visualization of Polymer Crystallization by a Combination of Atomic Force Microscopy with Fast Scanning Calorimetry. APS March-2019. At Boston USA.

Curriculum Vitae

1. **Full name** Zhang, Rui
2. **Date and place of birth** August 23th 1989, Yaan, Sichuan, China
3. **Present address** 18059 Rostock, Justus-v.-Liebig-Weg 6a
4. **Affiliation, title and degree** University of Rostock, Institute of Physics, Ph.D. student, M.Eng. in Material Science
5. **Short Scientific Biograph**

2016 Ph.D. student, Polymer Physics Group, Institute of Physics, University of Rostock.

2012 M.Eng. in Materials Science, Southwest Petroleum University (Technischehochschule), Chengdu, Sichuan, China

Thesis: Study on the slow processes of polymers in many body systems

2008 B.Eng. in Materials Science

Southwest Petroleum University (Technischehochschule),

Chengdu, Sichuan, China

6. **Feld of Specialization** Polymer Crystallization, Fast Scanning Calorimetry, Atomic force Microscopy.
7. **Main Publications**

[1] **R. Zhang**, E. Zhuravlev, R Androsch, C Schick; Visualization of Polymer Crystallization by in situ Combination of Atomic Force Microscopy and Fast Scanning Calorimetry. Polymers 2019, 11, 890.

[2] R. Androsch, **R. Zhang**, C. Schick, Melt-recrystallization of poly (L-lactic acid) initially containing α-crystals, Polymer, 2019, 176,227-235.

[3] R. A. Andrianov, R. Androsch, **R. Zhang**, T. A. Mukhametzyanov, A. S. Abyzov, J.W.P. Schmelzer, C. Schick; Growth and dissolution of crystal nuclei in poly(l-lactic acid) (PLLA) in Tammann's development method. Polymer 2020, accepted.

Acknowledgements

I want to thank my supervisor Prof. Dr. Christoph Schick, University of Rostock, very much for giving me the opportunity to carry out this work. The very essential and fruitful discussions helped me to get a deeper insight into many problems of calorimetry and polymer solidification.

I would like to thank Dr. Evgeny Zhuravlev, University of Rostock, for valuable discussions and ideas.

I am very grateful to all my colleges (former and present) for their support and friendship.

Prof. Dr. Androsch René, Martin Luther University Halle-Wittenberg and Dr. Jürn Schmelzer, University of Rostock, I acknowledge for the important contribution to phenomenological and theoretical interpretation of my data.

Many helpful suggestions about AFM device from Dr. Anna Müller, Anfatec Instruments AG, are very appreciated.

I am very thankful for financial support from Carbonene Technology Co. Ltd, Sichuan, China, and Functional Materials Rostock e.V., Germany, what allowed me to carry out this work.

This work would not be possible without the serious support and help form my family.